Optoelectronic properties of LaVO$_3$ perovskite for photovoltaic applications investigated by surface potential measurements

Relatore:

Prof.ssa Daniela Cavalcoli

Correlatore:

Dott.ssa M. Antonietta Fazio

Presentata da:

Margherita Sola

Optoelectronic properties of LaVO$_3$ perovskite for photovoltaic applications investigated by surface potential measurements

Margherita Sola

Abstract

La ricerca su materiali innovativi per applicazioni fotovoltaiche si è orientata negli ultimi anni verso lo studio delle perovskiti, utilizzate per lo sviluppo di nuove tipologie di celle solari ad alta efficienza e basso costo. Negli ultimi anni, si è assistito ad un incredibile sviluppo delle celle solari basate sulle perovskiti, che, all'inizio del 2016, hanno raggiunto un'efficienza certificata del 22.1% [1], un valore impressionante considerata la loro scoperta molto recente. Tuttavia, la commercializzazione di tali celle solari è ancora lontana, a causa della loro grande instabilità. L'ossido di lantanio-vanadio ($LaVO_3$) è un ossido composto da due metalli di transizione che presenta la struttura cristallina della perovskite. Questo materiale è molto promettente per applicazioni fotovoltaiche, in quanto potrebbe risolvere il problema della stabilità.

Lo scopo di questa tesi è quello di studiare sperimentalmente questo materiale, e di valutarne la possibile applicazione nello sviluppo di dispositivi solari a basso costo e alte prestazioni.

In questo contesto, gli obiettivi della tesi sono stati: lo studio delle proprietà ottiche ed elettriche del $LaVO_3$, condotto con metodi di *surface photovoltage* (SPV); l'implementazione e l'ottimizzazione di un apparato sperimentale di *surface photovoltage spectroscopy* (SPS), insieme con lo sviluppo del relativo software di acquisizione dati.

L'apparato per SPS è stato implementato con successo, il set-up sperimentale è stato ottimizzato al fine di migliorare il segnale misurato ed è stato sviluppato un software per il controllo del sistema e l'acquisizione dati.

Lo studio delle proprietà morfologiche del $LaVO_3$ alla nanoscala, condotto mediante microscopia a forza atomica, ha permesso l'identificazione delle condizioni di deposizione ottimali dei film sottili. Lo studio delle proprietà elettriche alla nanoscala, condotto mediante *scanning Kelvin probe microscopy*, ha permesso la determinazione del valore dell'altezza barriera all'interfaccia $LaVO_3$/ZnO e delle *work function* di ZnO e $LaVO_3$.

Si noti che il valore di *work function* del LaVO$_3$ non era mai stato riportato prima in letteratura. Le misure SPV sul LaVO$_3$ hanno generato un segnale minore del limite di rilevazione dell'apparato: ciò significa che le coppie elettrone-lacuna fotogenerate non vengono separate e raccolte in modo efficiente.

In conclusione, il LaVO$_3$ è noto per avere proprietà ottiche ottimali ed elevata stabilità, che sono vantaggi considerevoli per eventuali dispositivi fotovoltaici. Tuttavia, le misure di SPV, che sono sensibili alle proprietà di trasporto oltre a quelle ottiche, hanno chiaramente dimostrato che questo materiale non è ottimale come mezzo per il trasporto di carica. Perciò, i campioni di LaVO$_3$ analizzati non sono adatti per applicazioni fotovoltaiche. Per risolvere il problema, la soluzione potrebbe essere quella di incorporare nella struttura materiali per il trasporto dei portatori, creando così una struttura "mista" [2]. In una simile struttura, le numerose interfacce presenti consentirebbero la separazione e la raccolta delle coppie elettrone-lacuna fotogenerate. Queste considerazioni potrebbero aprire la strada a sviluppi futuri relativi allo studio e all'ottimizzazione del LaVO$_3$ come materiale per applicazioni fotovoltaiche.

The research on innovative materials for photovoltaic application has recently focused on perovskites for the development of new types of high efficiency and low cost solar cells. Perovskite based solar cells faced indeed an unbelievable increase in the last years, reaching a certified efficiency of 22.1% in early 2016 [1], an impressive value considering their recent discovery. However, perovskite based solar cells are still far from commercialization because of their high instability. Lanthanum-vanadium oxide (LaVO$_3$) is a transition metal oxide perovskite promising for photovoltaic applications, which could overcome the stability issue.

Aim of the present thesis is the experimental study of this material and the evaluation of its possible application in the development of low cost and high performance solar devices.

Within this framework, the objectives of the thesis were: the investigation of LaVO$_3$ optical and electrical properties by surface photovoltage (SPV) studies; the implementation and optimization of a surface photovoltage spectroscopy (SPS) experimental set-up, along with the development of the related data acquisition software.

The SPS set-up has been successfully implemented, the experimental set-up has been optimized in order to enhance the measured signal and a software for data acquisition

and system control has been developed. The study of $LaVO_3$ morphological properties at the nanoscale, by atomic force microscopy, allowed for the identification of the optimal deposition conditions of the layers. The study of the electrical properties at the nanoscale by scanning Kelvin probe microscopy allowed for the determination of the barrier height value at the $LaVO_3/ZnO$ interface and the work functions of ZnO and $LaVO_3$. It is noteworthy that the measured value of the work function of $LaVO_3$ has never been reported in literature up to now. Surface photovoltage spectroscopy on $LaVO_3$ gave a signal below the detection limit of the apparatus, showing that photogenerated electron-hole pairs are inefficiently separated and thus collected.

In conclusion, $LaVO_3$ is known to have optimal optical properties and high stability, which are considerable benefits for possible photovoltaic devices. However, SPV measurements, which are sensitive to transport properties besides the optical ones, have clearly shown that this material is a poor charge-transport medium. As a consequence, it can be concluded that $LaVO_3$ investigated layers are not suitable for photovoltaic applications. To overcome this limitation, a solution could be the incorporation of additional carrier-transport materials into a mixed structure [2]. In such a structure, a huge number of internal interfaces between the individual solar absorber and nanostructured charge transport media would enable the separation and collection of photogenerated electron-hole pairs. These considerations could pave the way for future developments on the study and optimization of $LaVO_3$ perovskite as a material for photovoltaic applications.

Contents

Introduction

The last decade witnessed an astonishing development in the renewable energies field, considered to be the best alternative to fossil fuels for energy production. Among all the available renewable energy sources, photovoltaics is the most promising one, as solar energy is free and widely distributed over the Earth and it drives to a low release of pollutants. Moreover, in the last years, a rapid decrease in the production costs of Si based solar cells paved the way to a fast diffusion of photovoltaics technology.

In particular, the research is focused on the development of new types of photovoltaic devices, the so called third generation solar cells, whose main features are high efficiency and low cost production. Within this framework, the research of new photovoltaics materials plays a crucial role.

Perovskites have been considered as promising photovoltaic materials for the first time around the year 2000; the first solar cell was obtained in 2012, around 50 papers were published on this subject in 2012, and more than 1000 in 2015 [3]. The tremendous increase in the interest on these materials is due to their optimal properties: strong light absorption, high carrier mobility, compatibility with several materials used in other photovoltaics approaches, and simple approach and low cost of the technology. Perovskite based solar cells faced indeed an unbelievable increase in the last years, reaching a certified efficiency of 22.1% in early 2016 [1], an impressive value considering that seven years ago these devices did not exist at all. However, perovskite PV are still far from commercialization because of their high instability.

In this thesis a peculiar perovskite, lanthanum-vanadium oxide ($LaVO_3$), is investigated. It is a transition metal oxide (TMO) perovskite, intrinsically much more stable, thus resulting in a considerable benefit for possible photovoltaic devices based on $LaVO_3$. The present thesis aims to study the optical and electrical properties of this material in

view of the potential photovoltaic applications.

The main objectives of the present thesis are the following:

1. the implementation and optimization of a surface photovoltage spectroscopy experimental set-up, and the development of the related data acquisition software;

2. the investigation of optoelectronic properties of $LaVO_3$ by surface potential measurements. In particular, surface photovoltage spectroscopy, atomic force microscopy, electrical force and scanning Kelvin probe microscopies have been used to detect the light induced variation of the surface potential and to map surface properties at the nanoscale.

The outline of the thesis is the following. Chapter 1 provides an introduction to current energy trends, namely renewable energy sources among which photovoltaics is on the front line. Then, the working principles of the photovoltaic cell and the state of the art of photovoltaics are described, leading to the perovskite solar cells.

In Chapter 2, the physics of surface photovoltage is described, and the experimental set-ups for surface photovoltage measurements reported in literature are presented.

In Chapter 3, after an introduction on $LaVO_3$ material properties, the spectroscopic set-up implemented in the present thesis is presented in detail. In particular, attention is paid on both its hardware components and its software developed for data acquisition and system control. In the last section, atomic force microscopy and electrical force microscopy techniques employed for morphological and electrical analysis are described.

In Chapter 4, the results of all the measurements on different samples are described.

A final discussion and some conclusions on the obtained results are presented.

Chapter 1

Photovoltaics: for a sustainable energy future

1.1 Current energy trends

The world energy system is an enormous and complex machine, and energy transition from fossil fuels to renewable sources is a long and difficult process.

The global primary energy consumption has grown at an average rate of 2.1% per year in the last decade. In 2014 it raised only by 0.9%, reaching an average rate of consumption of 17.2 TW [4]. This increase was the weakest one since 2009, indicating a possible trend towards moderation in the years to come. As shown in Fig. 1.1, fossil fuels yield 87% of the total primary supply, whereas renewable sources are going to reach the 10%. Nuclear has experienced a little increase in the last years, but this is not expected to affect the general trend, that its a progressive reduction, due to the ongoing decommissioning of many reactors in the US and Europe [5]. The demand for fossil energy amounts to 1066 barrels of oil, 108 000 m^3 of natural gas and 250 tonnes of coal per second worldwide [4]. Oil still continues to be the first energy source, the largest majority of which (ca. 80%) is used for the transportation system, while the rest is employed for heat and electricity, petrochemicals, asphalt, and lubricants [6].

The predominance of oil products in transportation has lately been weakened by natural gas and electricity, that currently represent 8.5% of the transportation fuels in the US, the largest nonpetroleum share since 1954. After decades of a fairly static scenario, the
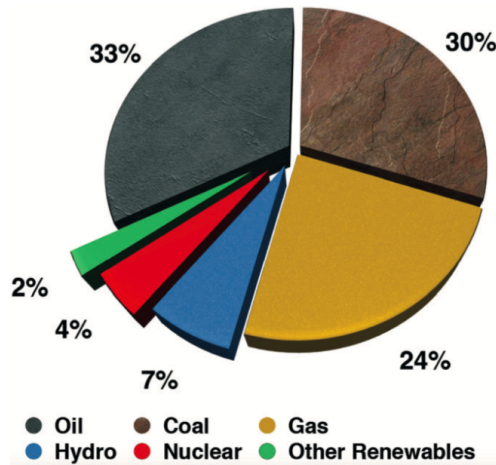
Figure 1.1: Global supply of commercialy traded primary energy [4, 6].

world oil system is now undergoing considerable changes, mainly pulled by the depletion of conventional reserves [7].

Natural gas is the most geographically concentrated energy resource; while the largest conventional gas field in the world is between Iran and Qatar, Siberia and the Russian Arctic host three of the top five world deposits. These three countries host nearly 50% of the world's estimated reserves [4]. In the last decade, the implementation and diffusion of horizontal drilling and hydraulic fracturing in the US has untapped many unconventional gas deposits stuck in shale formations across the country [8]. The US natural gas production has increased by over 40% in the last ten years, bringing the country again as the world's largest producer, well ahead of Russia [4]. However, these activities have lead to a large environmental and public health discussion, including groundwater contamination, methane release in the atmosphere and induced seismicity. Nevertheless, there is no doubt that natural gas will be increasingly exploited during the first half of this century as a bridge towards renewable energies [9]. The estimated reserves of coal are still the largest among fossil fuels. They could cover the current world demand for over 110 years, compared to 52.5 and 54.1 years for oil and natural gas, respectively [4].

The most relevant change in the world energy landscape in the last years comes from the continuous rise of renewable energies, especially in the electricity field. In 2014, for the first time, global carbon emissions associated with energy production remained

stable despite economic growth. This effect was primarily due to the increasing use of renewables and enhanced energy efficiency [10]. The leading actor in this scenario is China, which now produces as much electricity from sunlight, water and wind as all the power plants in Germany and France combined, covering 20% of its internal demand. In the period 2008-2012, its investments in non-fossil energy plants increased by 40%, whilst those in fossil-fueled facilities were significantly reduced [11].

The exceptional 7-fold drop of the photovoltaics (PV) price in the last decade (mainly caused by a huge increase of the Chinese production) has made PV a truly game changer in the global energy market. The locations where PV electricity is competitive with traditional technologies is continuously increasing and its share of electricity production in many industrialized countries has become remarkable [11]. In 2014, Italy produced about 8% of its energy needs by PV, so far the largest share in the world [6].
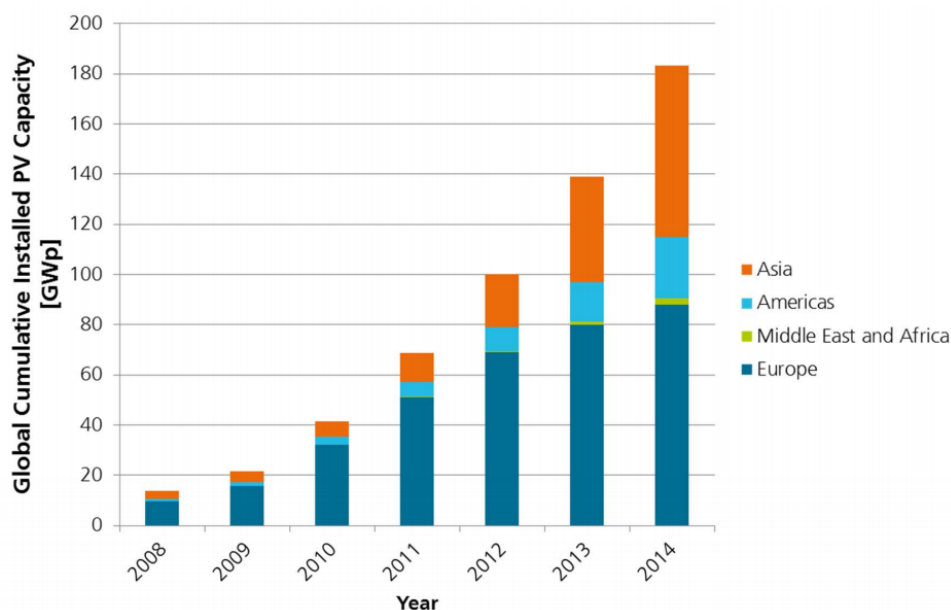
Figure 1.2: Global cumulative PV installation over years [12].

All the renewable energy sources are constantly growing. In 2014, hydroelectric global capacity exceeded 1 TW, wind reached 370 GW, and PV almost 180 GW. They respectively covered 16.6%, 3.1% and 0.9% of the world electricity demand; although the two last shares seem to be small, they are considerable values, since hydroelectricity has been an established technology for over 120 years, whereas wind and PV were virtually

non-existing just twenty years ago. Furthermore, estimated direct and indirect jobs in renewable energies worldwide are almost 8 million (1.2 million in European Union) and continue to rise [10].

The previous data show that the energy transition from fossil fuels to renewable sources is already ongoing and indicate that PV is at the forefront among renewable energies, as shown by data of last years PV installations presented in Fig. 1.2 [6].

1.2 The physics of solar cells

Sunlight is the most important energy source for humanity: it is homogeneously distributed over the Earth, abundant (90 PW = 90·10^{15} W received on the planet's surface) and unlimited, since it will last for more than 4 billion years. The current energy consumption rate of our civilization (17.2 TW in 2014) is 5000 times smaller than the solar energy irradiating the surface of the Earth [9]. However, mankind cannot use solar energy unless it is converted into a final usable energy form: heat, electricity, fuels. While conversion of solar energy into heat is direct, its conversion into electricity creates several problems, as explained in the followings.

A solar cell is a device that converts sunlight into electricity through the photovoltaic effect. Photovoltaic energy conversion results from *charge generation*, *charge separation* and *charge transport*.

A photovoltaic solar energy converter absorbs photons to excite electrons to a higher energy level, where they have increased electrochemical potential energy. To make the extraction of the excited electrons possible, an energy gap has to occur in the material band structure: a semiconductor is a very good example of such a system. The separation of the energy bands is needed to maintain the excited electrons at the higher energy for a long time compared to the thermal relaxation time, so that they may be collected. The excited electrons must be extracted and collected: these steps require a mechanism for charge separation. Some intrinsic asymmetry is needed to drive the excited electrons away from their point of creation (Fig. 1.3). In order to complete the photovoltaic conversion process, charges have to be lead to the external circuit; for this reason, the material should be a good electrical conductor. Perfect conduction means that carriers must not recombine with defects or impurities, and should not transfer energy to the

6

medium. There should be no resistive loss (series resistance) or current leakage (parallel resistance). The material around the junction should be highly conductive and ensure good Ohmic contacts to the external circuit [13].
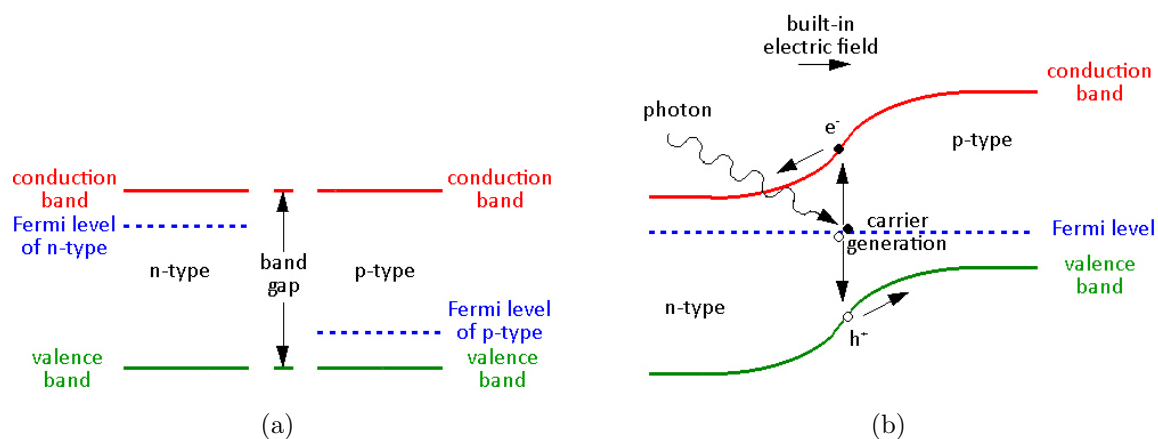
Figure 1.3: (a) Band structure of differently-doped semiconductors. (b) Band structure of a p-n junction; principle of photovoltaic device: photon absorption, carrier generation and separation [14].

Charge separation and transport are provided by the semiconductor p-n junction (which is the classical model of a solar cell) as shown in Fig. 1.3 or by another interface with the same electronic features, such as the Schottky barrier or the heterojunction [13].

1.3 Photovoltaics: basic principles

Edmund Bequerel firstly reported the photovoltaic effect in 1839, when he observed the production of an electric current from the action of light on a silver coated platinum electrode immersed in an electrolyte [13].
It was only around the 1950s, with the development of good quality silicon wafers (thanks to the new solid state electronics), that crystalline silicon photovoltaic devices produced potentially useful quantities of power. Chapin, Fuller and Pearson firstly reported in 1954 a silicon solar cell able to convert sunlight with an efficiency of 6% [13].
However, due to their high production cost, estimated about $200 per Watt, these cells were not considered for industrial power generation for several decades.
Interest in photovoltaics expanded during the 1990s, along with the growing awareness

of secure sources of electricity alternative to fossil fuels.

Although many other materials have been studied, silicon still remains the foremost photovoltaic material, thanks to the advances of silicon technology achieved by the microelectronics industry.

During the late 1990s, the photovoltaic production grew at a yearly rate of 15-25%, driving a relevant reduction in cost and opening up new markets [13].

1.3.1 The solar resource

The Sun emits light with a range of wavelengths, spanning the ultraviolet, visible and infrared sections of the electromagnetic spectrum. Its extra-terrestrial spectrum is similar to that of a black body at 5760 K, although it is considerably attenuated and changed in shape because of the Earth's atmosphere [13]. This is due to scattering and absorption events by atmosphere particles (oxygen, ozone, and nitrogen, water and CO_2), which are responsible for the dips in the absorption spectrum shown in Fig. 1.4.
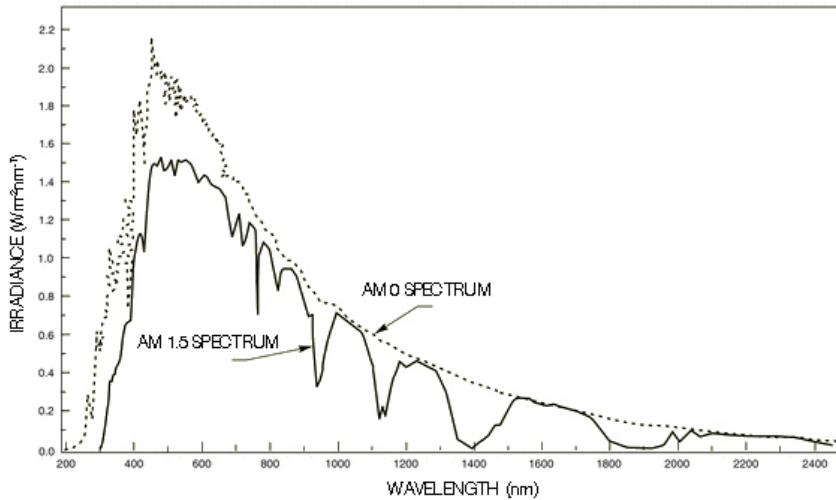
Figure 1.4: Extra-terrestrial (AM 0) solar spectrum compared with the standard terrestrial (AM 1.5) solar spectrum. Plot adapted from [15].

Attenuation by the atmosphere is quantified by the Air Mass factor, n_{AirMass} defined as:

$$n_{\text{AirMass}} = \frac{\text{optical path length to Sun}}{\text{optical path length if Sun directly overhead}}. \tag{1.1}$$

8

This definition is necessary because, depending on the position of the Sun, rays have to pass through a different width of atmosphere. Because of its great variability, Air Mass 1.5, or AM 1.5, is considered as the standard spectrum, for a total power density content of 1 kW/m^2. The AM 1.5 spectrum is an extraterrestrial solar spectrum attenuated by 1.5 thickness of an Earth atmosphere of standard composition [13].

1.3.2 Characteristics of the photovoltaic cell

Open circuit voltage and short circuit current

Charge separation due to incident light establishes a photovoltage when the terminals are isolated (infinite load resistance); this physical quantity is called the *open circuit voltage* V_{oc}.

The photocurrent drawn when the terminals are connected together is called the *short circuit current* I_{sc}. For any intermediate load resistance R_L, a voltage V between 0 and V_{oc} is established and the cell delivers a current I such that $V = IR_L$, where $I(V)$ is determined by the current-voltage characteristic of the cell under that illumination. Thus, when a load is connected to the external circuit, the cell produces both current and voltage and it can do electrical work [13].

Photocurrent and quantum efficiency

The size of the current generated by the cell in short circuit depends upon the intensity and the energy spectrum of the incident light. Photocurrent is related to incident spectrum by the *quantum efficiency QE* of the cell, which is the probability of generating an electron per incident photon as a function of photon energy. Then the *short circuit current density* J_{sc} is:

$$J_{sc} = q \int b_s(E) QE(E) dE \tag{1.2}$$

where $b_s(E)$ is the incident spectral photon flux density (the number of photons of energy in the range E to $E + dE$ which are incident on unit area in unit time) and q is the electronic charge [13]. QE depends on the absorption coefficient of the solar cell material and on the effectiveness of charge separation and charge collection in the device, whereas

it does not depend on the incident spectrum. For this reason, QE is therefore a key quantity to evaluate solar cell performance under different conditions [13].

Dark current

When a load is present, a potential difference is established between the terminals of the cell, which drives a current in the opposite direction to the photocurrent. This reverse current is usually called the *dark current* in analogy with the current $I_\mathrm{dark}(V)$ which flows across the device under an applied bias V in the dark. For the p-n junction solar cell, the behaviour is that of a diode in the dark, and for an ideal diode the *dark current density* J_dark under an applied bias V follows the law:

$$J_\mathrm{dark}(V) = J_0(e^{\mathrm{qV}/\mathrm{k_B T}} - 1) \tag{1.3}$$

where J_0 is a constant, k_B is Boltzmann's constant and T is the temperature [13]. The total current of the cell can be approximated as the sum of the short circuit photocurrent and the dark current. This approximation is reasonable for many photovoltaic materials although the reverse current flowing in response to voltage in an illuminated cell is not formally equal to the current which flows in the dark. The net *current density* $J(V)$ in the cell is

$$J(V) = J_\mathrm{sc}(V) - J_\mathrm{dark}(V) \quad \text{[13]}. \tag{1.4}$$

As the load resistance is increased, the potential difference increases as a consequence, while the net current decreases, until the photocurrent and dark current exactly cancel out: this is equivalent to the case when the contacts are isolated and the bias has its maximum value, that is the open circuit voltage V_oc [13].

Efficiency and fill factor

The working condition of the solar cell is the bias range, from 0 to V_oc, in which the cell delivers power (at $V < 0$, the illuminated device acts as a photodetector, consuming power to generate a photocurrent; at $V > V_\mathrm{oc}$, the device once again consumes power, operating as a light emitting diode).
The cell *power density* P is:

$$P = J(V)\, V \tag{1.5}$$

with $J(V)$ given by Eq. 1.4. P reaches a maximum at the cell's maximum power point, called "operating point" [13]. This occurs at some voltage V_m, close to V_oc, with a corresponding current density J_m, shown in Fig. 1.5. The optimum load resistance corresponds to this point.

The *fill factor FF* is defined as the ratio:

$$FF = \frac{J_\mathrm{m} V_\mathrm{m}}{J_\mathrm{sc} V_\mathrm{oc}} \tag{1.6}$$

and describes the "squareness" of the $J - V$ curve, as shown in Fig. 1.5 [13].
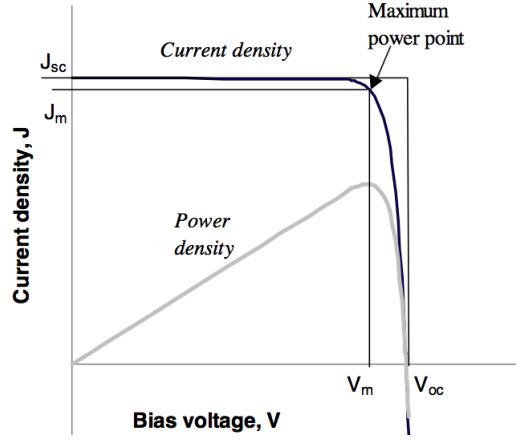
Figure 1.5: The current-voltage (black) and power-voltage (grey) characteristics of an ideal cell. The maximum power density $J_\mathrm{m} V_\mathrm{m}$ is given by the area of the inner rectangle. The outer rectangle has area $J_\mathrm{sc} V_\mathrm{oc}$. If the fill factor were equal to 1, the current-voltage curve would follow the outer rectangle [13].

The *efficiency η* of the cell is the ratio between the power density delivered at operating point and the incident light power density P_s:

$$\eta = \frac{J_\mathrm{m} V_\mathrm{m}}{P_\mathrm{s}}. \tag{1.7}$$

These four quantities J_sc, V_oc, FF and η are the key performance characteristics of a solar cell. The performance characteristics values for the most common solar cell materials are listed in Table 1.1. It can be noticed that solar cell materials with higher J_sc tend to have lower V_oc; this effect will be explained in section 1.3.4.

Cell Type	Area (cm^2)	V_{oc} (V)	J_{sc} (mA/cm^2)	FF	Efficiency (%)
crystalline Si	4.0	0.706	42.2	82.8	24.7
crystalline GaAs	3.9	1.022	28.2	87.1	25.1
poly-Si	1.1	0.654	38.1	79.5	19.8
a-Si	1.0	0.887	19.4	74.1	12.7
CuInGaSe$_2$	1.0	0.669	35.7	77.0	18.4
CdTe	1.1	0.848	25.9	74.5	16.4

Table 1.1: Performance of some PV cells [13].

Parasitic resistances

The solar cell can be modelled as a current generator in parallel with an ideal diode. In real cells, power is dissipated through the resistance of the contacts and through leakage currents around the sides of the device. These effects are electrically equivalent to two parasitic resistances, one in series (R_s) and one in parallel (R_{sh}) with the cell, as shown in Fig. 1.6. For an efficient cell, R_s has to be as small and R_{sh} has to be as large as possible [13].
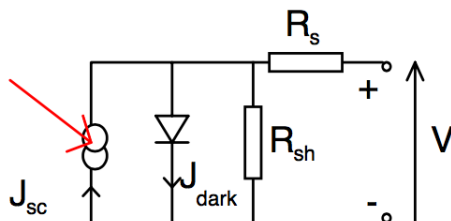
Figure 1.6: Equivalent circuit of a real solar cell, with series and shunt resistances [13].

1.3.3 Detailed Balance

The principle of detailed balance gives rise to one of the fundamental physical limitations on the performance of a photovoltaic cell. This relies on the fact that the solar cell exchanges thermal radiation with its surroundings environment: any body which absorbs light must also emit light, because of its finite temperature. The rate of photon emission by the cell must be equal to the rate of photon absorption, so that in the steady-state the concentration of electrons in the material remains constant [13].

In equilibrium

If the cell is in the dark, in thermal equilibrium with the ambient, the current density absorbed from the ambient $j_{\mathrm{abs}}(E)$ is:

$$j_{\mathrm{abs}}(E) = q(1 - R(E))a(E)b_{\mathrm{a}}(E) \tag{1.8}$$

where $a(E)$ is the absorbance of the material, i.e. the probability of absorption of a photon of energy E, $R(E)$ is the reflectance, i.e. the probability of photon reflection, and b_{a} is the incident flux of thermal photons from the ambient (it is assumed that each absorbed photon of energy E generates one electron) [13].

On the other hand, the current density for photon emission $j_{\mathrm{rad}}(E)$ is:

$$j_{\mathrm{rad}}(E) = q(1 - R(E))\varepsilon(E)b_{\mathrm{a}}(E) \tag{1.9}$$

where $\varepsilon(E)$ is the emissivity, i.e. the probability of emission of a photon of energy E.

The cell emits these photons by spontaneous emission (or radiative recombination), that is the emission of a photon of the energy released by an excited electron relaxing to its ground state [13].

For preserving a steady state, the current densities j_{abs} (Eq. 1.8) and j_{rad} (Eq. 1.9) must balance, hence [13]:

$$\varepsilon(E) = a(E). \tag{1.10}$$

Under illumination

If the cell is under illumination, some electrons are excited, inducing the production of a voltage and a photocurrent; however, in these conditions, spontaneous emission is also increased. This radiative recombination is an unavoidable loss, which means that absorbed solar radiant energy can never be fully utilised by the solar cell.

The delivered current is due to the difference between the flux of photons absorbed from the Sun and the flux of photons emitted by the excited device.

The cell absorbs solar photons of energy E at a rate $(1-R(E))a(E)b_{\mathrm{s}}(E)$, where b_{s} is the incident flux of thermal photons from the Sun. The equivalent current density for

photon absorption includes a term from thermal photons and therefore:

$$j_{\text{abs}}(E) = q(1 - R(E))a(E)\left(b_{\text{s}}(E) + Cb_{\text{a}}(E)\right) \tag{1.11}$$

where the coefficient of b_{a} is introduced to consider the fraction of the incident ambient flux which has been replaced by solar radiation [13].

1.3.4   Limiting efficiency: the Shockley-Queisser limit

The power conversion efficiency is the ratio between the incident and the extracted power from the photon fluxes (Eq. 1.7). The incident power density P_{s} is the integral of the incident irradiance $L(E)$ (the emitted energy flux density) over photon energy [13]:

$$P_{\text{s}} = \int L(E)dE = \int Eb_{\text{s}}(E)dE. \tag{1.12}$$

For cell power density, Eq. 1.5 is recalled [13]:

$$P = J(V)\ V. \tag{1.13}$$

The power conversion efficiency η is then:

$$\eta = \frac{J(V)\ V}{P_{\text{s}}} \tag{1.14}$$

and maximum efficiency is achieved when:

$$\frac{d}{dV}\eta = \frac{d}{dV}J(V)\ V = 0. \tag{1.15}$$

Effect of bandgap

As it has already been said, photocurrent is due to the difference between the flux of photons absorbed from the Sun and the flux of photons emitted by the excited device; then, the photocurrent density at short circuit J_{sc} can be obtained by integrating over photon energy [13]:

$$J_{\text{sc}} = q\ \int_0^\infty b_{\text{s}}(E)QE(E)dE. \tag{1.16}$$

However, since bands are separated by a bandgap E_{g}, photons with $E < E_{\mathrm{g}}$ are not absorbed, because an electron in the lower band needs at least an energy equal to E_{g} to be promoted to the upper band. It is assumed that the material is perfectly absorbing and non-reflecting, and that each absorbed photon of energy $E \geq E_{\mathrm{g}}$ is absorbed to promote one electron to the upper band. Within these assumptions, the maximum photocurrent is obtained for this specific bandgap. Then:

$$QE(E) = a(E) = \begin{cases} 1 & E \geq E_{\mathrm{g}} \\ 0 & E \leq E_{\mathrm{g}} \end{cases} \tag{1.17}$$

and

$$J_{\mathrm{sc}} = q \int_{E_{\mathrm{g}}}^{\infty} b_{\mathrm{s}}(E) dE \quad [13]. \tag{1.18}$$

Photocurrent is then only a function of the bandgap and of the incident spectrum. It is clear that the lower is E_{g}, the greater will be J_{sc} [13].

On the other hand, voltage is due to the electrochemical potential energy of the excited electron, thus V_{oc} must always be equal to or less than $\frac{E_{\mathrm{g}}}{q}$ [13].

It is evident that very small or large bandgap values will lead to poor photoconverters: in the first case due to a small working value of V, while in the second due to a small working value of the photocurrent. Hence, considering Eq. 1.15, it is possible to calculate
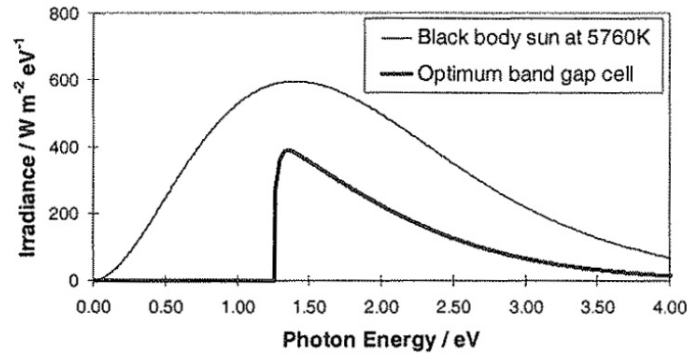
Figure 1.7: Power spectrum of the Sun modelled as a black body at 5760 K, and power available to the optimum bandgap cell. Clearly, no photons with energy less than E_{g} contribute to the available power [13].

15

the maximum efficiency. For each spectrum, there is an optimum bandgap at which η has a maximum, and, for a standard solar spectrum, this limit was reported by Shockley and Queisser in 1961: it is around 33% at a bandgap of 1.4 eV, for the standard AM 1.5 solar spectrum [13].

Optimising the performance of the ideal single bandgap photoconverter is therefore a matter of choosing the appropriate material [13].

1.3.5 The ideal photoconverter and some problematic issues

In order to achieve the limiting efficiency, a real device should have strong light absorption, efficient charge separation and charge transport, an optimum energy gap, and an optimised load resistance.

The condition of the bandgap is satisfied by several materials, but the requirement for conductivity makes semiconductors an appropriate choice. Due to their bandgaps in the range 0.5 - 3 eV, semiconductors can absorb visible photons and excite electrons across the bandgap, where they may be collected. The III-V compound semiconductors gallium arsenide (GaAs) and indium phosphide (InP) are favoured for high efficiency cells, having bandgaps close to the optimum (1.42 eV and 1.35 eV, respectively, at 300 K). Silicon is cheap and abundant compared to these III-V materials, and it is the most used solar cell material, despite its less favourable bandgap (1.1 eV). Other compound semiconductors, namely cadmium telluride (CdTe) and copper indium gallium diselenide ($CuInGaSe_2$) have been developed for thin film photovoltaics. According to recent developments in semiconducting molecular materials, organic semiconductors are promising materials for photovoltaic energy conversion in the future [13].

Besides the intrinsic limit due to the bandgap and the fact that the process is threshold-based, other reasons that limit real solar cells performances are the following.

- Incomplete absorption of the incident light. Photocurrent is reduced since photons are not absorbed when passing through the cell, or being reflected from the front surface or from the contacts.

- Non-radiative recombination of photogenerated carriers. Defect sites trap excited charges, that subsequently recombine before being collected, reducing thus the

photocurrent. This happens where the surface defect density is higher, or near interfaces with another material, or near the junction.

- Voltage drop due to series resistance between the point of photogeneration and the external circuit, that reduces therefore the available power [13].

Other features of materials used for solar energy conversion should be: abundance on the planet, low environmental impact throughout the life cycle, stability for many years under light irradiation, and they should be not too much expensive.
Intermittence and intensity fluctuations due to diurnal cycles and atmospheric conditions are other problems concerning solar energy conversion. For this reason, storage components are often required as an integral part of the systems [6].

1.4 Strategies for high efficiencies: emerging photo-voltaics

Solar cells are classified into three generations, which indicate the order of which each became important.

The first cells are made of crystalline silicon (c-Si), the commercially predominant PV technology. The second generation cells are thin film solar cells, including amorphous silicon, CdTe and CuInGaSe$_2$ (CIGS) cells, and they are quite commercially significant. The third generation of solar cells includes several thin film technologies, often described as emerging photovoltaics, which are still at research or development stage [13].

Concurrent research progresses into all the three generations, while the first generation technologies are most highly represented in commercial production. c-Si solar cells currently represent about 90% of the market, because of Si is stable, non toxic, abundant and its physical properties are well known. Furthermore, the technology is mature, thanks to the massive use of Si in the microelectronic industry [13].

Fig. 1.8 presents the features, in terms of costs and efficiency, of the three generations of cells. The potential benefits of the current research in the third generation solar cells are evident: reaching high efficiency at low cost per power.
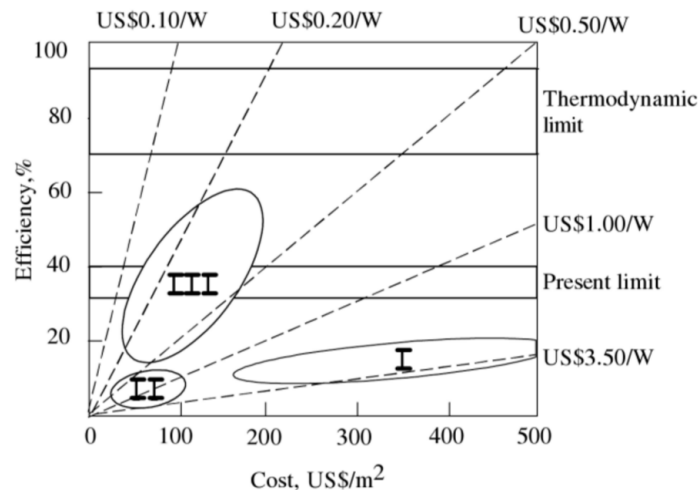
Figure 1.8: Efficiency vs. trade-cost for the three generations of solar cells [16].

Figure 1.9: Evolution of solar cell efficiencies from the 1970s to present days [1].

Fig. 1.9 shows the state of the art of the highest confirmed efficiencies for different photovoltaic technologies, as reported by National Renewable Energy Laboratory (NREL) [1]. The highest achievements have been obtained so far for multi-junction technologies used in combination with solar concentrators.

In the following paragraphs some of the most promising photovoltaic technologies will be briefly reviewed.

1.4.1 CIGS thin film solar cells

$CuIn_{1-x}Ga_xSe_2$ (copper indium gallium diselenide, or CIGS) is a direct gap semiconductor, where the value of x can vary from 0 ($CuInSe_2$, pure copper indium diselenide) to 1 ($CuGaSe_2$, pure copper gallium diselenide). The bandgap varies continuously with x from about 1.0 eV (for $CuInSe_2$) to about 1.7 eV (for $CuGaSe_2$). CIGS has a chalcopyrite crystal structure (Fig. 1.10) [17].
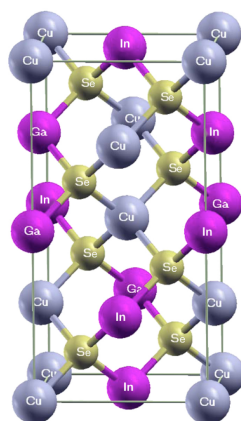
Figure 1.10: CIGS unit cell: the lattice elements are tetrahedrally coordinated. Se atoms have two bonds to InGa and two bonds to Cu atoms [17].

CIGS main feature is that it has an optical absorption which is among the highest known for all semiconductors; therefore, a much thinner film is required with respect to other semiconductor materials. Its strong absorption, as well as its availability in both p- and n-types, make it attractive for thin film photovoltaics. The conductivity of p-type CIGS is due to native defects, mostly indium vacancies and copper atoms on indium sites, and can be adjusted by varying the Cu/In ratio during growth. Electron diffusion length is similar to the grain size, determining an internal quantum efficiency up to 90% [13].

1.4.2 Multi-junction solar cells

Single junction solar cells are limited by the material bandgap to a portion of the solar spectrum: photons with energy higher than the bandgap lose their excess energy by thermalization, while photons with energy below the bandgap are not successfully converted. A possible strategy to increase the efficiency of a solar cell is to stack multiple solar cells using materials with different bandgaps that could exploit a broader range of the solar spectrum, resulting in a multi-junction solar cell, as shown in Fig. 1.11 [18].
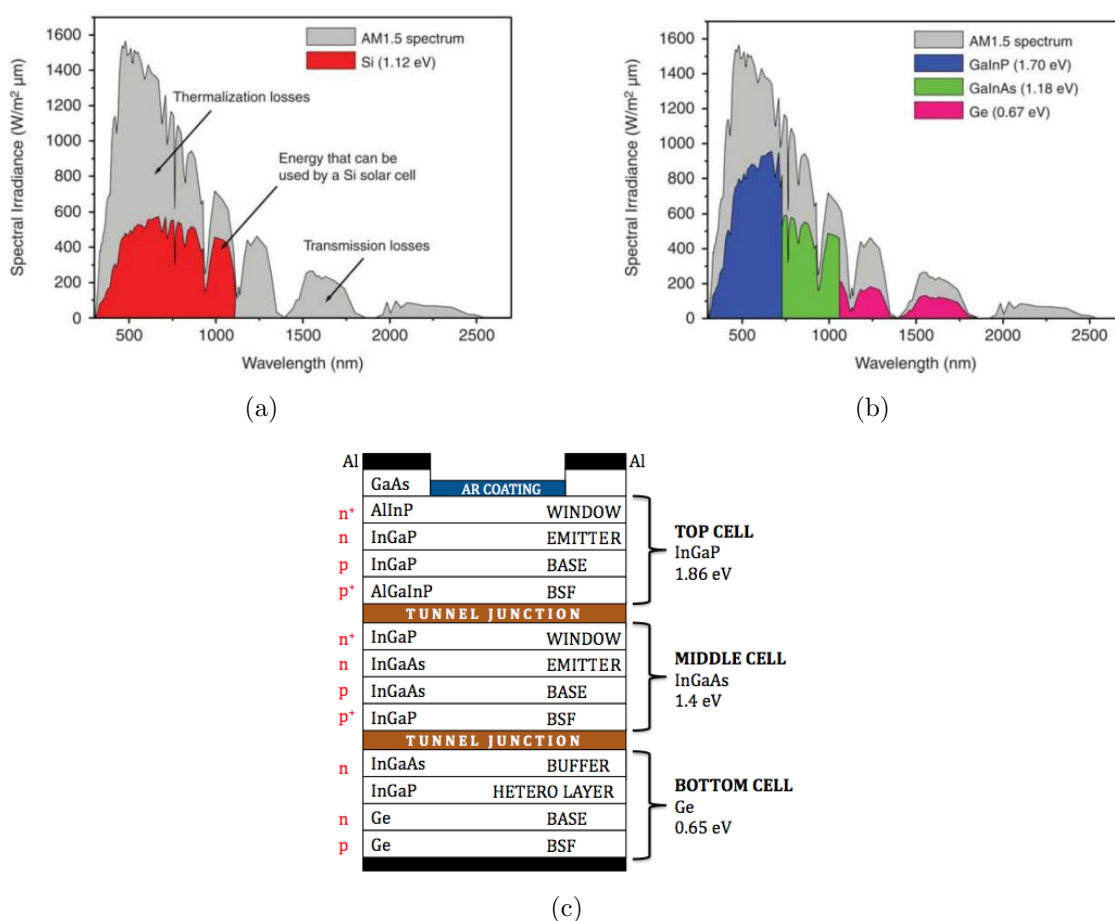
Figure 1.11: Spectral irradiance vs. wavelength over the AM 1.5 solar spectrum; plots show the parts of the spectrum that can be used, in theory, by: (a) Si solar cells; (b) GaInP/GaInAs/Ge solar cells [18]. (c) Structure of a multi-junction solar cell [19].

Each layer going from the top to the bottom has a smaller bandgap than the previous

one. In this way it absorbs and converts the photons with energies greater than its bandgap and smaller than the bandgap of the higher layer [20].

These solar cells have a maximum theoretical efficiency limit of 86.8% and their main limitation is related to the availability of materials with optimal bandgaps that allow high efficiency due to low defect densities [18].

The best materials for fabricating such multi-junction cells are III-V compound semi-conductors. In fact, they have bandgaps which span a wide spectral range -mostly with direct bandgaps with a high absorption coefficient- and they can also be grown with excellent material quality because of similar lattice constants [18, 21]. This is a key feature for the reason why all layers must have similar crystal structure, since a mismatch between different layers creates dislocations and significantly deteriorates the efficiency of the solar cell.

The success of this technology has been achieved thanks to these factors, leading to reach the highest solar-to-electric conversion efficiency of any photovoltaic device so far. Clearly, the key problem with multi-junction cells is the high production cost of this technology [18, 21].

1.4.3 Dye-sensitized solar cells and organic photovoltaics

Dye-sensitized solar cells (DSSC) and organic photovoltaics (OPV) will be probably the next PV technology to become commercially significant.
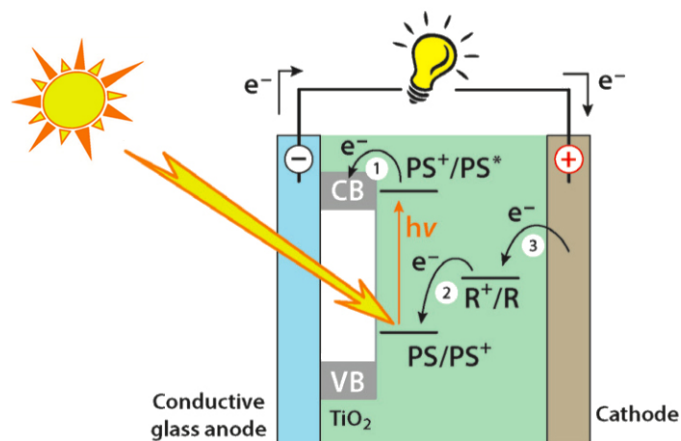
Figure 1.12: Working principle of a dye-sensitized solar cell [6].

Fig. 1.12 schematically depicts the DSSC working principle. A photosensitizer (PS) is

22

linked to a semiconductor electrode and the process is mediated by a redox molecule (R). Therefore, compared to conventional photovoltaics, the DSSC main difference is that light absorption, and electron-hole transport are carried out by different components (dye, semiconductor, electrodes, redox mediator). For this reason, the degrees of freedom to optimize the device are, in principle, many more [6].

Organic photovoltaic (OPV) systems, instead, are based on photoactive p-conjugated polymers and small molecules, as shown in Fig 1.13. The chemical nature of these materials and the simple device architecture often result in lightweight, solution processable and flexible devices. OPV systems are mostly based on abundant elements and low cost materials, can be produced at high manufacturing throughput, and allow easy recycling of constituent materials. These are excellent features for application perspectives and market diffusion [6].
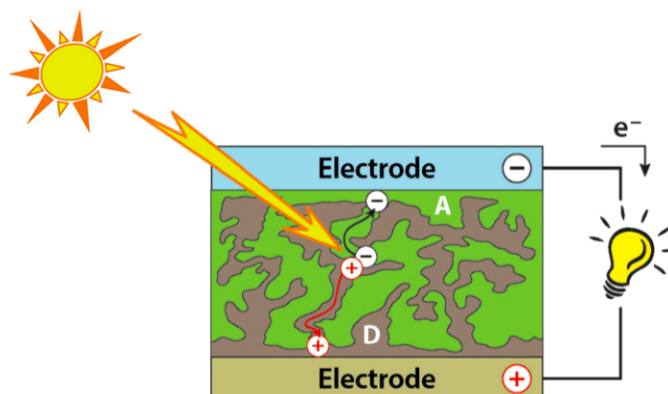
Figure 1.13: Schematic representation of an organic photovoltaic cell with bulk heterojunction [6].

For several years, expectations for their market debut have been high, but they have materialized only to a very small extent so far. In fact, although DSSC and OPV can be manufactured at smaller economic and energetic cost, they are still not competitive on efficiency and lifetime, which is a strong barrier for a wide market diffusion [6].

1.4.4 The rise of perovskite

Perovskite is a calcium titanium oxide mineral composed of calcium titanate ($CaTiO_3$). The mineral was discovered in the Ural Mountains of Russia by Gustav Rose in 1839

and it is named after Russian mineralogist Lev Perovski [22].

The term perovskite indicates by extension a wide class of compounds that exhibit the same particular crystal structure as $CaTiO_3$ and have the general formula ABX_3 (A and B are two cations of different size and X is an anion that binds to both). A is usually an alkaline earth or rare earth element and B could be a 3d, 4d, and 5d transition metal [6]. Several metallic elements are stable in the perovskite crystal structure, as shown in Fig. 1.14.
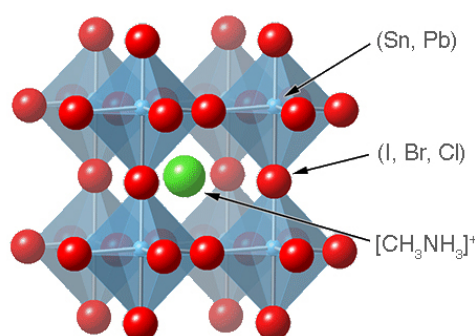
Figure 1.14: Perovskite crystal structure [23].

Apart from the structure, perovskites used in PV devices have nothing in common with the rock-solid oxides that naturally occur in minerals. They are synthetic hybrid organic–inorganic methylammonium lead halide materials of the general formula $CH_3NH_3PbX_3$ (in which X = I, Br, Cl).

They were firstly used for solar applications by Miyasaka and co-workers in 2009 and by Park and co-workers in 2011. In these works, the hybrid perovskite $CH_3NH_3PbI_3$ was used in a DSSC, reporting a cell efficiency of 3.5% in 2009 [24] and 6.5% in 2011 [25].

The sudden rise of perovskite PV begun in 2012, when the two above-mentioned groups published, independently, perovskite-based devices with efficiencies between 9.7 and 10.9%, jointly with the groups of Snaith [26] and Grätzel [27]. In all these works, a solid-state device structure was used, avoiding decomposition of the perovskite absorber in the electrolyte.

Since 2012, several hundreds of papers have been published on this subject, also thanks to the simplicity and low cost of this technology, which can be easily performed with very standard lab equipment. The purpose of these works was to rationalize the working mechanism and to enhance the device efficiency through materials and device optimiza-

tion.

Although the first efficient solid-state perovskite cells were reported only in mid-2012, extremely rapid progress was made during 2013 with energy conversion efficiencies, reaching a confirmed 16.2% at the end of the year. This increased to a confirmed efficiency of 17.9% in early 2014 [28], and achieved a certified efficiency of 22.1% in early 2016 [1], an impressive value considering that seven years ago these devices did not exist at all. During these years, the structure of the cell has further evolved, as shown in Fig. 1.15.

(a)   (b)
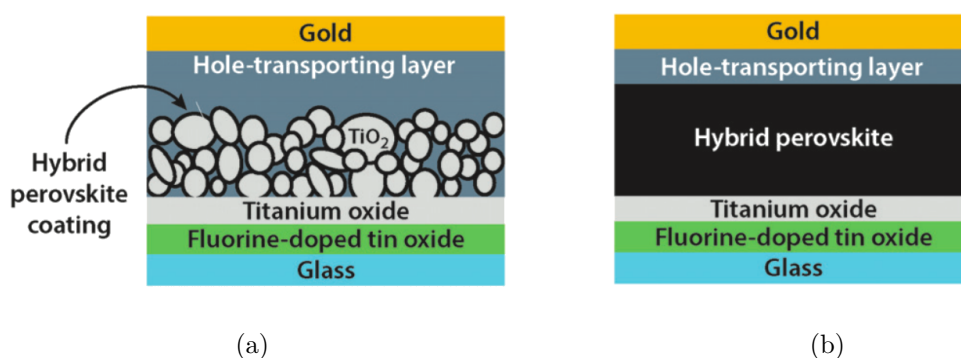
Figure 1.15: Evolution of the architectures of solar cells based on hybrid perovskites. In (a) the perovskite is deposited on mesoporous TiO_2 and serves as light absorber and hole conductor. In (b) the perovskite is deposited as a thin film and serves as light absorber and ambipolar semiconductor, which transports both electrons and holes [6].

The current dominant material in the PV perovskite field remains $CH_3NH_3PbI_3$, the best performance described in the seminal paper of Miyasaka and co-workers [24]. This material is cheap, can be easily deposited with wet methods and matches all the following features that, in principle, make it ideal for PV.

- Strong absorption over the entire visible spectral window with the spectral onset at 800 nm (bandgap 1.55 eV), enabling fabrication of very thin films.

- Low "loss-in-potential" within the cell, allowing open circuit voltages (V_{oc}) of over 1.0 V, much higher than DSSC and OPV (0.7–0.8 V).

- A very weak exciton binding energy (0.03 eV), allowing prompt dissociation into free carriers at room temperature.

- High carrier mobility and carrier diffusion lengths as long as 1 μm (i.e. 100 times longer than traditional thin film technologies).

- Ambipolar semiconductor character, enabling an excellent and balanced electron-hole transport, with remarkable simplification of the device.

- An easy crystal-growth control, allowing nearly perfect crystalline films with very low defect densities and ideal charge transport features.

- Compatibility with many materials used in other PV approaches (e.g. DSSC and OPV), which allows testing of new and unconventional device architectures [6].

$CH_3NH_3PbI_3$ is a material with many positive characteristics, but also relevant problems. This is the reason why perovskite PV is still far from commercialization. $CH_3NH_3PbI_3$ can lose its perfect crystallinity at temperatures typically experienced inside solar panels under intensive irradiation and, upon dissolution, it generates PbI_2, a carcinogen banned in many countries.
Perovskite PV experienced a much faster rise of efficiency over time compared to OPV and DSSC. At present, perovskites are envisaged as top cells in future tandem systems to harvest a larger portion of solar spectrum. This would overtake the Shockley and Queisser efficiency limit for single junction systems, which is set at about 31% for perovskite cells [6].

In this thesis a peculiar perovskite, $LaVO_3$, will be investigated (Sec. 3.1).

Chapter 2

Analysis on materials for photovoltaic applications: surface photovoltage (SPV)

The surface photovoltage (SPV) method is a contactless technique for semiconductor characterization that relies on analysing illumination-induced changes in the surface voltage.

This section is intended to provide a brief overview of one specific variant of the SPV method: surface photovoltage spectroscopy (SPS), in which changes in band-bending (both at the free semiconductor surface and at buried interfaces) are monitored as a function of incident photon energy. This technique permits the extraction of many important surface and bulk parameters (bandgap and carriers type, carrier diffusion length and lifetime, surface/bulk state distribution and properties) and can be used for complete construction of surface and interface band diagrams, including the measurement of energy levels in quantum structures.

SPS measurements are contactless and non-destructive; moreover, they can be performed both *in situ* and *ex situ*, they are ambient insensitive and capable of any lateral resolution, in principle down to the atomic scale [29, 30].

In 1953, Bardeen and Brattain discovered that an external light illuminating the semiconductor induces a change in its surface potential [31]. Afterwards, Johnson showed that surface photovoltage measurements may yield minority carrier lifetimes (1957) [32]

and Goodman developed an algorithm for the extraction of the minority carrier diffusion length (1961) [33].

The history of SPS begins in the early 1970s, with systematic research on the effects of sub-bandgap illumination on the surface voltage, performed by Gatos, Lagowski and Balestra [34]. These researchers realized that they had invented a powerful tool for surface state characterization and also coined the term "surface photovoltage spectroscopy" (SPS).

Since then, SPS has become popular and has been used as an extensive source of surface and bulk information on semiconductors and semiconductor interfaces. From the mid-1990s, Shapira's group, and more recently Pollak's group, have systematically applied SPS for quantitative studies of various semiconductor interfaces and heterostructures, including actual device structures [29, 30].

2.1 The physics of SPV

2.1.1 Electrical properties of semiconductor surfaces

In this section a brief introduction to the electrical properties of semiconductor surfaces is presented.

A surface is defined as a boundary of media with different physical properties; the surface between a semiconductor and vacuum or gas is usually referred to as a "free surface" and the surface between a semiconductor and another solid is usually referred to as an "interface" [29].

The periodic structure of an ideal crystalline semiconductor, whose electronic wave functions are Bloch waves (periodic functions with the same periodicity as the crystal), results in the appearance of allowed energy bands separated by forbidden energy gaps.

The termination of the periodic structure of a semiconductor at its free surface gives rise to surface-localized electronic states within the semiconductor bandgap and/or a double layer of charge, known as a surface dipole. Of course, similar considerations can be applied to a semiconductor interface too [29].

The presence of surface-localized states induces charge transfer between bulk and surface in order to establish thermal equilibrium between the two; hence, the free carrier density

near the surface deviates from its equilibrium value in the bulk and the charge transfer results in a surface space-charge region (SCR). According to the charge conservation rule:

$$Q_{ss} + Q_{sc} = 0 \qquad (2.1)$$

where Q_{ss} is the net surface charge and Q_{sc} is the net charge in the SCR (both per unit area) [29].

The surface may be found in three different regimes: (a) accumulation, where the majority carrier concentration at the surface is larger than its bulk value; (b) depletion, where the majority carrier concentration at the surface is smaller than its bulk value, but larger than the minority carrier concentration at the surface; (c) inversion, where the minority carrier concentration at the surface is larger than the majority one.

Thus, this region is electrically non-neutral, implying a non-zero electric field in it and thus a potential drop across it. Therefore, the surface potential, denoted as V_S, is different from the electric potential far away in the bulk, even under equilibrium conditions. These characteristics translate into a semiconductor band-bending in the vicinity of the surface. By definition, the higher the electrical potential, the lower the energy band, so that a positive V_S corresponds to downward-bent bands.

As an example, consider an n-type semiconductor with a depleted surface: electrons have been trapped in surface states such that they are repelled from the surface space-charge region and holes are attracted to it (electron concentration in SCR is smaller than its equilibrium value, but larger than that of the minority carriers). The potential drop across the SCR is manifested by the bending of the semiconductor bands, as shown in Fig. 2.1 (a) [29, 30].

The formation of surface and interface localized states typically involves additional phenomena besides the symmetry-breaking lattice termination, such as: "dangling bonds", i.e. the formation of surface atoms with no upper atom to bind to; surface reconstruction or relaxation, i.e. a change in the position or chemical bonding configuration of surface atoms to minimize the surface energy; impurity atoms adsorbed on the surface, etc [30]. In fact, in addition to surface states, another important phenomenon associated with a semiconductor surface is the surface dipole $\Delta\phi_S$.

The surface barrier is usually characterized by the electron affinity χ, that is the energy needed to release an electron from the conduction band into vacuum. At a real
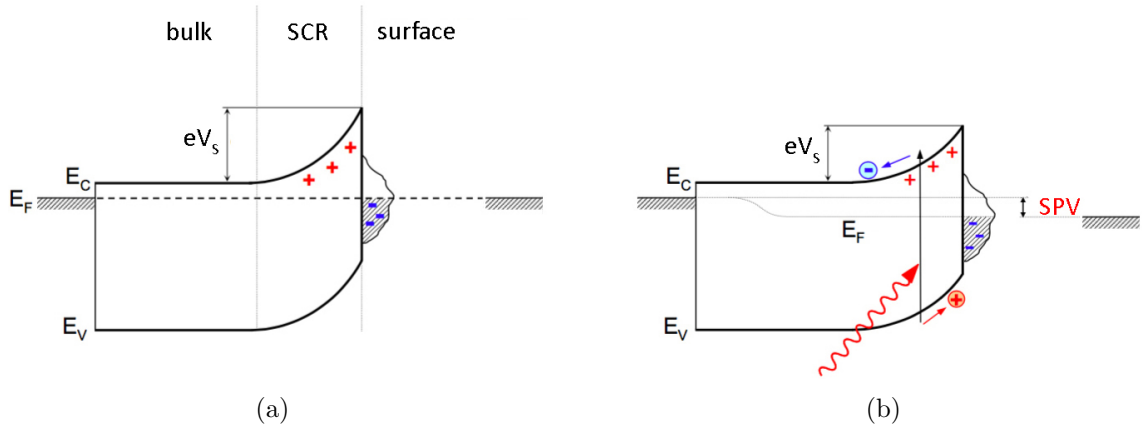
Figure 2.1: Band diagrams of a depleted n-type semiconductor surface: (a) in the dark, at thermal equilibrium; (b) under super-bandgap illumination with carrier separation under an electric field. The SPV is the change in the surface potential due to illumination.

semiconductor surface or interface, it is possible that microscopic dipole contributions (for example due to adsorption) lead to a band-bending such that the effective surface barrier, and therefore the effective electron affinity χ^*, may differ from the bulk ones due, indeed, to surface dipole effects (Fig. 2.2) [30].
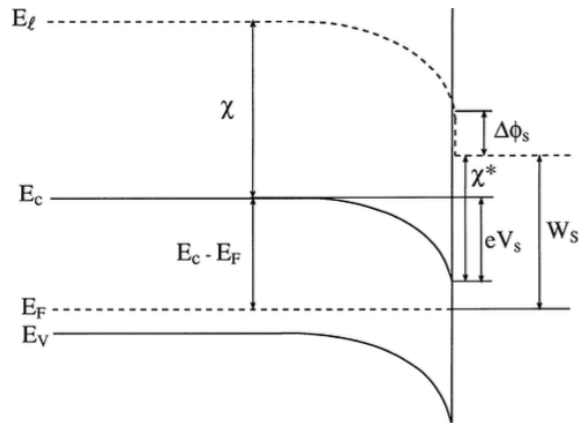
Figure 2.2: Band diagram at a semiconductor surface (depleted p-type). This figure also shows the semiconductor surface work function W_S, defined as the energy separation between the Fermi level E_F and the local vacuum level E_ℓ at the surface [29].

2.1.2   The surface photovoltaic effect

The photovoltaic effect at metal-semiconductor and semiconductor-semiconductor junctions is at the heart of semiconductor devices which convert light to electricity, as described above in Sec. 1.2. A specific variant of the photovoltaic effect is the less familiar surface photovoltaic effect, which is the focus of this section.

Let us consider SPV induced at the free surface of a semiconductor sample with a grounded ohmic back contact.

In the absence of an external field, the charge neutrality rule (Eq. 2.1), must remain valid regardless of illumination. However, both Q_{ss} and Q_{sc} may change upon illumination.

The absorbed photons induce the formation of free carriers by creating electron-hole pairs via band-to-band transitions, as shown in Fig. 2.1 (b) (typically dominant for super-bandgap photons) or release captured carriers via trap-to-band transitions (typically dominant for sub-bandgap photons). Thus, a significant amount of charge may be redistributed between the surface and the bulk, hence, the potential drop across the surface SCR changes, together with the surface potential. It is important to note that the establishment of a SPV occurs only if carrier generation per se is followed by a net charge redistribution.

It is important to underline that the magnitude of the SPV effect increases with decreasing temperature, because the carriers transitions induced by SPV take place against a background of thermal transitions [29, 30].

2.2   Experimental set-up

The SPV measurements are non-trivial because the surface potential is a built-in potential, not an external potential. Therefore, application of any contact to measure the built-in voltage will alter the surface properties and hence the quantity under measurement. Consequently, many elaborate techniques for measuring the surface potential (or at least changes of it) without applying a direct electrical contact have been developed [29, 30].

2.2.1 The Kelvin probe

Re-examining the electronic band structure at a semiconductor surface (Fig. 2.2), it is evident that any change in the surface band-bending eV_S causes a variation of equal magnitude in the surface work function W_S. Therefore, a measurement of work function changes is completely equivalent to a direct SPV measurement (in absolute value).

The oldest techniques for measuring the work function difference between two materials (first employed in 1951 [35]) is by forming a parallel plate capacitor. This is presented in Fig. 2.3 for the simple case of two metals. Prior to connection, the two metals are electrically neutral and share the same local vacuum level - Fig 2.3 (a). Upon short-circuiting the metals, charge must flow from the metal with smaller work function to the metal with larger work function until the two Fermi levels match - Fig 2.3 (b).

As in any parallel plate capacitor, this charge transfer results in an electric field in the gap between the two plates and a drop in the local vacuum level across this gap. The voltage drop is equal to the difference in the work functions W of the two metals and is referred to as the contact potential difference (CPD):

$$eV_{CPD} = W_1 - W_2 = \Delta W_S. \tag{2.2}$$

Theoretically, CPD may be easily calculated if both the stored charge Q, and the capacitance C are known, because for a capacitor Q is equal to $C\,V_{CPD}$ [29, 30].

However, the extraction of these quantities is non-trivial and therefore another method to measure CPD had to be found. This obstacle was overcome by Lord Kelvin [36], who suggested that the CPD may be measured directly by a null method: when an external DC bias, equal and opposite to the CPD, is applied to the capacitor, the Fermi levels on both metals differ by eV_{CPD}, just as in the isolated case, as shown in Fig. 2.3 (c). No charge transfer between the metals do take place and the capacitor is discharged. Hence, in order to determine the CPD, it is sufficient to determine the applied bias that discharges the capacitor, even if neither the capacitor charge nor the capacitance is known. This technique is known as the Kelvin probe, after its inventor [29, 30].

The Kelvin probe arrangement has been broadly applied to the measurement of illumination-induced changes in work function starting from the earliest experiments of Bardeen and Brattain [31]. This has been achieved by ohmically contacting the back side of the semiconductor sample to a metallic reference electrode. The work function of the metallic

electrode does not change under illumination, so the following equation is assumed:

$$-e\Delta\mathrm{SPV} = e\Delta V_{\mathrm{CPD}} = \Delta W. \qquad (2.3)$$
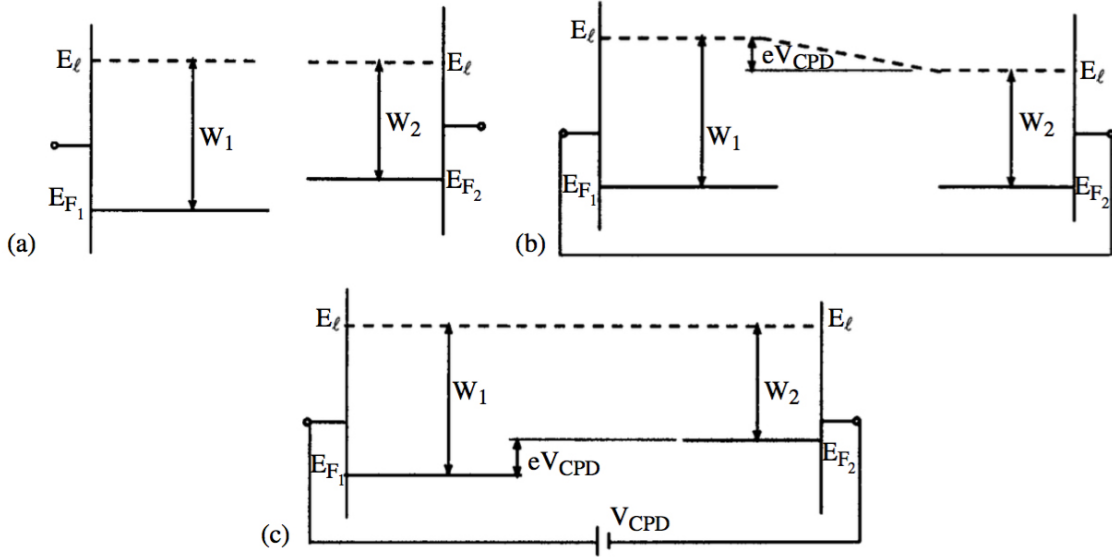
Figure 2.3: Band structrure of a parallel plate capacitor formed by two different metals, with the two plates: (a) isolated, (b) short-circuited, (c) connected through a DC bias equal and opposite to the CPD [29].

Most modern Kelvin probes rely on a periodically vibrated plate which oscillates near the sample surface, such that a steady-state AC current develops in the effective AC capacitor [37]. This current is equal to zero if, and only if, the capacitor is discharged. Therefore, the CPD is measured by determining the DC bias for which the external AC current is cancelled out.

2.2.2 The metal–insulator–semiconductor approach

Another method to directly measure the SPV is performed by using a metal–insulator–semiconductor (MIS) structure.

Let us consider a MIS capacitor, brought into open-circuit mode by disconnecting its two terminals. If illumination is now applied to the capacitor, V_{S} may change due to the photovoltaic effect, producing an equal change in the measurable voltage between the two

capacitor terminals. Therefore, the SPV at a free semiconductor surface can be attained by measuring the photo-induced voltage changes between the MIS capacitor terminals. The first scientist who has applied the above explained method was Morrison in 1953, achieving the MIS structure by placing a static metallic grid in front of the sample [38]. Thus, a MIS structure where the insulator was simply air or vacuum was produced, and contactless, non-destructive SPV measurements were taken (using chopped illumination in conjunction with lock-in detection to enhance the SPV signal).

Subsequently, Morrison's method has been employed by many other scientists. The air/vacuum gap could be replaced by an insulating spacer (e.g. mylar), as long as the placement of the spacer does not modify the surface properties of the semiconductor [29].

2.2.3   Scanning SPV measurements

Both Kelvin probes and MIS structures may be employed also in a scanning mode, which allows for lateral variations recording in the SPV by scanning a small probe or a well-focused light beam across the surface. Both approaches are typically limited to a lateral resolution roughly of the order of $\sim$1 µm [39].

To achieve even finer lateral resolution, SPV measurements can be performed by scanning tunnelling microscopy (STM) and atomic force microscopy (AFM). By the early 1990s, both STM [40] and AFM [41] have been used for SPV measurements, opening new horizons for SPV mapping with a resolution previously unknown.

2.3   Applications of SPS

As explained above, the SPS method permits the extraction of many parameters of materials (e.g. bandgap and carriers type, carrier diffusion length and lifetime, surface/bulk state distribution and properties) and it can be used for complete construction of surface and interface band diagrams. Moreover, SPS can be applied not only to clean surfaces but also to real ones, in practically any ambient, because it is contactless and non-destructive [30].

In the following paragraphs some basic applications of SPS measurements are presented.

2.3.1 Bandgap energy and semiconductor type

The first application of SPS is the determination of the semiconductor bandgap, based on the large increase in light absorption at the bandgap energy E_g found in most semiconductors. This increase leads to a significant change of the SPV signal, which is easily identified as a sharp change in the slope of the SPV curve and is often the most significant one in a given spectrum.

The use of SPS for extraction of E_g is nothing but an emulation of an absorption spectrum. The advantages of using SPS instead of transmission spectroscopy are that SPS does not require light collection beyond the sample, allowing its use on arbitrarily thick samples, and does not require the sample to be removed from the substrate or grown on a transparent one [30].

To determine the type (p or n) of semiconductor using SPS, the focus must be on the sign of the "knee" associated with the SPV onset: most semiconductor surfaces are depleted, which means that the bands of p-type semiconductors are bent downwards towards the surface, whereas the bands of n-type semiconductors are bent upwards (as described above in Sec. 2.1.1) [30].
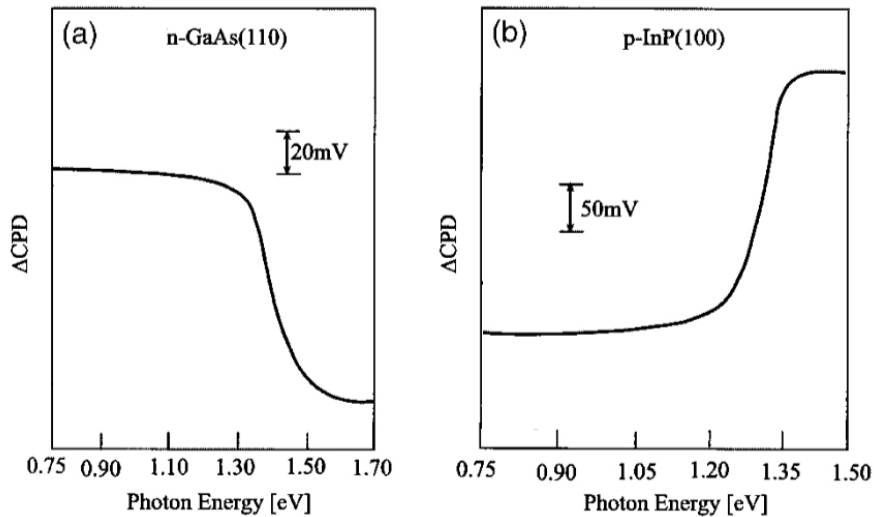
Figure 2.4: Surface photovoltage spectra of: (a) an n-type GaAs(110) surface, UHV cleaved; (b) a p-type InP(100) surface, UHV cleaved. Adapted from [42].

Super-bandgap illumination typically tends to decrease the surface band-bending, and

thus n-type semiconductors show a positive SPV (negative ΔCPD), while p-type semiconductors show a negative SPV (positive ΔCPD). This is presented, as an example, in the SPV spectra of n-type GaAs and p-type InP (shown in Fig. 2.4), which clearly feature opposite onset signs [30].

Hence, SPS could be very useful in determining the semiconductor type if it is unknown, and in making fast and non-destructive check for semiconductors whose doping is non-trivial and subject to compensation by their native doping (for example the p-doping of GaN which is natively a n-type [43]).

2.3.2 Defect state characterization

Another key aspect of SPS is the possibility to determine the energy position and type of surface states. In fact, a "knee" in the SPV spectrum appears whenever the photon energy exceeds the threshold energy of a certain transition, including those induced by sub-bandgap photons from a surface state to a band, or viceversa. If the transition involves excitation of electrons from the surface state to the conduction band, a positive change in the surface charge is induced and hence a positive SPV (negative ΔCPD) is expected. Otherwise, excitation of holes to the valence band makes the surface charge more negative, and a negative SPV (positive ΔCPD) is expected. Therefore, the combination of the SPV threshold energy and slope sign make the determination of the approximate position of the surface state within the bandgap possible [30].

2.3.3 Characterization of multilayer structures

In the above discussion only uniform bulk samples have been considered. However, actual semiconductor samples may be thin, not much larger than the diffusion or absorption length, so that excess carriers may be generated close to the back surface as well. Samples may also have a multilayer structure that has several buried interfaces due to junctions in the structure (this is the typical case for photovoltaic material samples).

At first glance, interfaces that are buried deep into the sample may seem unable to contribute to the measured SPV signal, due to screening by a thick quasi-neutral region. Conversely, optical absorption in any non-neutral region present within the sample does contribute to the measured SPV signal, since the energy bands are serially connected and therefore the potential of the free surface is linked to any other illuminated region,

no matter how deep is located within the sample.

Thus, the sensitivity of SPV measurements of a certain region in the semiconductor is limited only by the absorption length of the photons, i.e. by the possibility of introducing free excess carriers in the region of interest. Therefore, beyond the study of surface and bulk properties, the characterization of multilayer structures by SPS technique has widely spread in the literature in recent years [29, 30].

As an example, consider the SPV spectrum of a ZnO:Al/ZnO/CdS/CIGS layered structure used for the fabrication of thin-film solar cells (Fig. 2.5) [44]. Distinct spectral "knees" are observed at $\sim$1, $\sim$2.4, and $\sim$3.1 eV, corresponding to the bandgaps of CIGS, CdS and ZnO respectively, and confirming SPS sensitivity to buried interfaces.

In a similar way, SPS allows for the characterization of quantum wells and other low-dimensional heterostructures [29, 30].
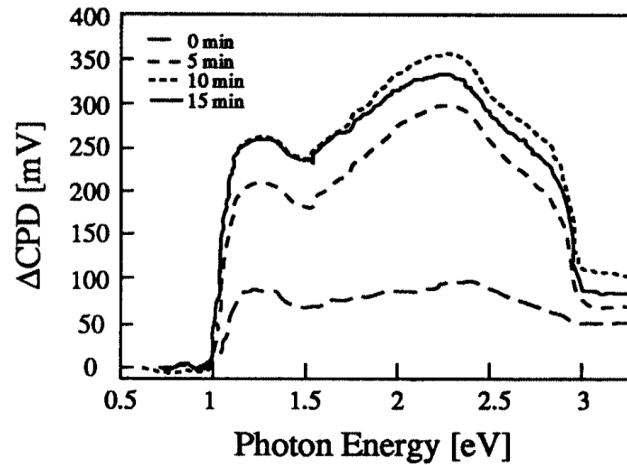
Figure 2.5: Surface photovoltage spectra of ZnO:Al/ZnO/CdS/CIGS structures for several annealing times. The three bandgaps of CIGS, CdS and ZnO can be clearly observed respectively at $\sim$1, $\sim$2.4, and $\sim$3.1 eV (the "feature" at $\sim$1.5 eV is an artefact due to a change of filter at that energy) [44].

Since SPS is contactless and non-destructive, characterization of multilayer structures can be successfully performed on actual device structures, for process monitoring and quality control, resulting in significant savings in time and money [30].

Chapter 3

Materials and Methods

In the following sections the material under investigation and several experimental methods are described. After an introduction on LaVO$_3$ material properties, the spectroscopic set-up implemented in the present thesis is presented in detail. In particular, attention is paid on both its hardware components and its software developed for data acquisition and system control. In the last section, atomic force microscopy and electrical force microscopy techniques employed for morphological and electrical analysis are described.

3.1 LaVO$_3$

Lanthanum-vanadium oxide (LaVO$_3$) is not a typical hybrid organic-inorganic perovskite as those described in Sec. 1.4.4. It is a transition metal oxide (TMO) perovskite; its structure is shown in Fig. 3.1.
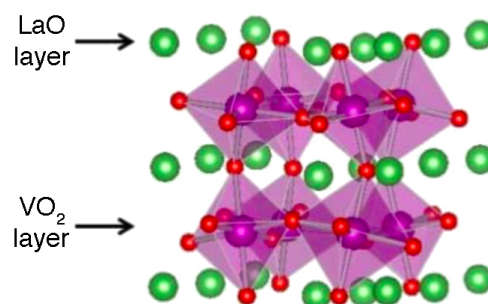
Figure 3.1: LaVO$_3$ perovskite structrure. The La, V and O atoms are shown as green, purple, and red spheres, respectively [45].

TMOs derived from the perovskite structure form a unique class of materials that exhibit several functional properties such as metal–insulator transition (i.e. they are Mott insulators), ferroelectricity, superconductivity, and huge magnetoresistance. The perovskite structure induces high electronic polarizability and strong Coulomb correlations, and these materials exhibit higher conductivity and lower work functions than non-perovskite oxides, making TMO perovskites promising candidates in the PV field [45, 46].

TMO perovskites contain only Earth-abundant elements and have intrinsically long-term chemical stability, making them suitable for durable, cheap and environmentally-friendly solar cells.

Moreover, the perovskite structure is extremely tolerant with respect to charge and size of the constituting cations: the different constituents make TMO perovskites bandgaps ranging from near infrared to ultraviolet, as shown in Fig. 3.2. Their structure compatibility and wide-range of different bandgaps could potentially bring to multi-junction solar cells based on TMO perovskites [2].

Among TMO perovskites, ferroelectric (FE) oxides are particularly interesting: their intrinsic polarization should separate photogenerated carriers, enhancing the PV effect (this is the so called "anomalous PV effect"); therefore, the maximum reachable output voltage is not limited by the absorber's bandgap, allowing in principle higher efficiency [47].
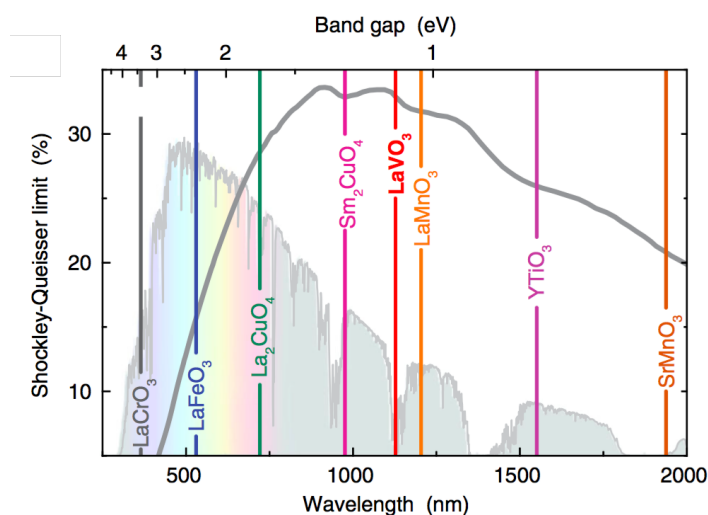
Figure 3.2: Shockley-Queisser limit as a function of the bandgap, over the solar spectrum. The bandgaps of many TMOs are marked [2].

In the last few years, several papers have been published on this subject, in order to study TMO perovskites and, especially, LaVO$_3$ properties and its possible applications. As regards the charge transport properties of LaVO$_3$, the temperature dependences of electrical resistivity showed a semiconducting behaviour. Magnetic susceptibilities revealed antiferromagnetic ordering at 137 K [48].

LaVO$_3$ physical properties are summarised in Tab. 3.1 [49].

In particular, the work of Wang et al. (2015) systematically investigated the optical absorption and transport properties of LaVO$_3$ films, and tested LaVO$_3$ as a light absorber in solar cells [2].

The optical bandgap obtained from the photoconductivity measurement is approximately 1.1 eV. According to the Shockely-Queisser limit curve the bandgap of LaVO$_3$ is close to the optimal value for solar energy conversion (Fig. 3.2): therefore, LaVO$_3$ can be a promising candidate as a light absorber in solar cells.

Absorption spectra of the LaVO$_3$ films were also systematically measured and analysed; they showed, besides the 1.1 eV bandgap, a set of direct bandgaps at 1.80, 2.99, and 4.30 eV in the higher-energy range, revealing a hierarchical bandgap behaviour [2].

Between the two tested technologies, the DSSC-type heterojunctions led to better photovoltaic performances than the thin film device structure.

In fact, in the conventional thin-film solar cells, semiconductors are assembled into planar p-n junctions, serving for both light harvesting and photocarrier transport; but LaVO$_3$ charge transport properties at room temperature are far inferior compared to those of crystalline semiconductors like Si or GaAs. Therefore, to obtain devices which work properly, the thicknesses of LaVO$_3$ layer should be comparable to the depletion layer thickness, which is often only several tens of nanometers. If the LaVO$_3$ layer is too thick, there will be no driving force to separate the photocarriers, and no photocurrent will be able to reach the electrodes [2].

These recent results pave the way for developing a class of PV devices based on LaVO$_3$ and TMO perovkites in general, indicating that the synthesis and transport properties of this material must be substantially improved in order to increase the power-conversion efficiency.

substance: $LaVO_3$

| crystal structure | tetragonal (perovskite, at 300 K) |
| | orthorhombic (D_{2h}^{16}-Pbnm) at RT, but tetragonal for $T < 139$ K |

lattice parameters

$a = b$	5.535 Å		tetragonal description
c	7.830 Å		
$a = b$	5.542 Å		orthorhombic description
c	7.838 Å		
a	7.868 Å	$T = 77$ K	tetragonal
c	7.738 Å		

energy gap

E_g	1.1 eV	direct absorption edge

electrical conductivity

σ	2.3 Ω^{-1} cm^{-1}	p-type semiconductor
	10^{-7} Ω^{-1} cm^{-1}	

hole concentration

p	$3 \cdot 10^{19}$	$T = 800$ K

hole mobility

μ_p	0.15 cm^2 V^{-1} s^{-1}	$T = 800$ K

Néel temperature

T_N	137 K

melting point

T_m	2353 K

Debye temperature

Θ_D	235 K

Table 3.1: $LaVO_3$ physical properties. Adapted from [49].

3.2   Experimental methods

3.2.1   Transmittance and SPS measurements set-up

This section describes the complete generic set-up both for transmittance and SPS measurements, a schematic view of which is given in Fig. 3.3 (a) and (b), respectively. For spectroscopic purposes it is necessary to generate the signal using a broadly tunable light source. The default choice, therefore, would be the use of a "white light" source in conjunction with a monochromator. The light also must be periodically chopped to allow for lock-in detection of the signal.

For transmittance measurements, the sample is simply placed in front of the output diffracted light beam, before the pyroelectric sensor, as shown in Fig 3.3 (a).
For SPS, the MIS structure (cf. Sec. 2.2.2) set-up was realised by using an ITO (Indium Tin Oxide) coated glass slide as the transparent electrode and placing it in front of the sample to achieve the plate capacitor configuration, where the insulating spacer is simply air. The output light beam passes through the slit and illuminates the sample through the coated slide. Both the ITO coated glass slide and the sample are contacted to the system with silver conductive paste. Then, the voltage signal is sent to a preamplifier before being read by the lock-in, as shown in Fig 3.3 (b).

The instrumental set-up is coordinated by a real-time computer program, described in Sec. 3.2.2. This program controls the monochromator motor and, thus, the wavelength changes, it reads the measurement results by interfacing with the lock-in, and finally stores the obtained spectrum for subsequent display and analysis.

Light sources

A QTH (Quartz Halogen Tungsten) lamp and a Xe (Xenon) lamp have been used as light sources. These lamps have high emission spectra at low (around 1 eV) and high (2-3 eV) energy, for the QTH and the Xe, respectively. Thus, using both lamps, it was possible to investigate a wide part of the light spectrum, from 300 to 2500 nm.

The emission spectrum of a QTH lamp is a black body emission spectrum, centred on a certain value depending on the filament temperature. A typical QTH emission spectrum
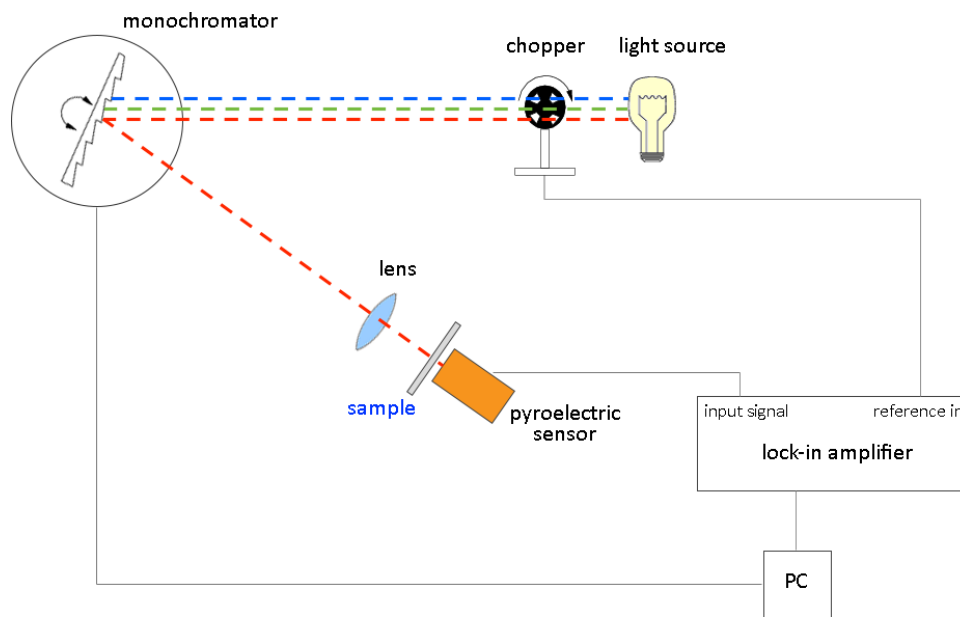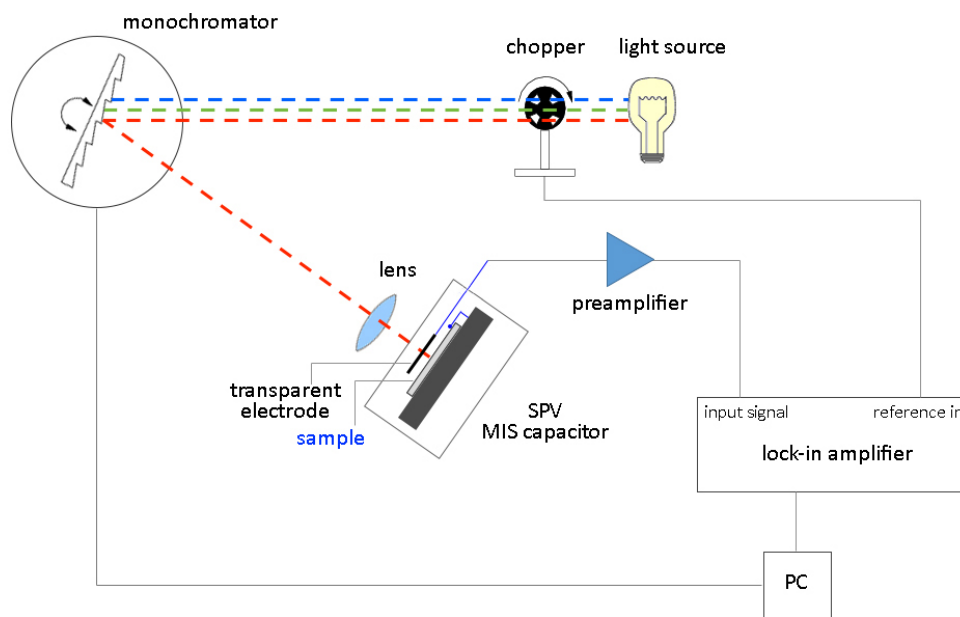
Figure 3.3: Transmittance (a) and SPS (b) measurements experimental set-up.

is shown in Fig. 3.4. The filament temperature depends on the applied voltage - in the present case equal to 23 V.
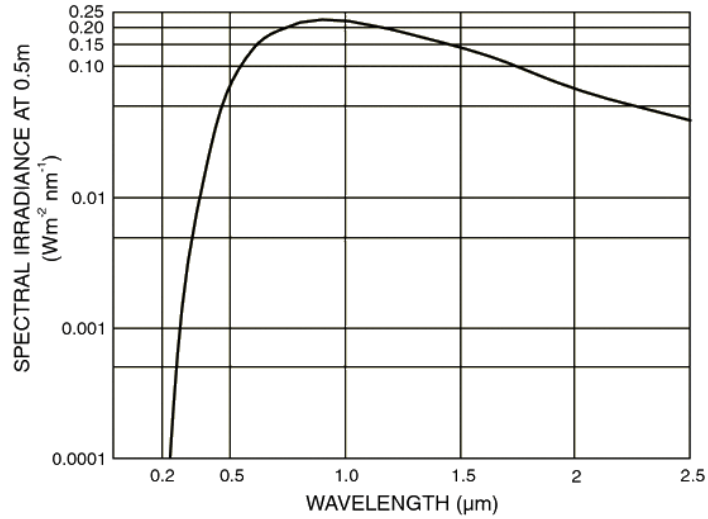
Figure 3.4: Spectral irradiance at 0.5 m from a 1000W QTH [50].

The Xe emission spectrum is slightly different; it is centred on a different wavelength value and several spikes occur, as shown in Fig. 3.5.
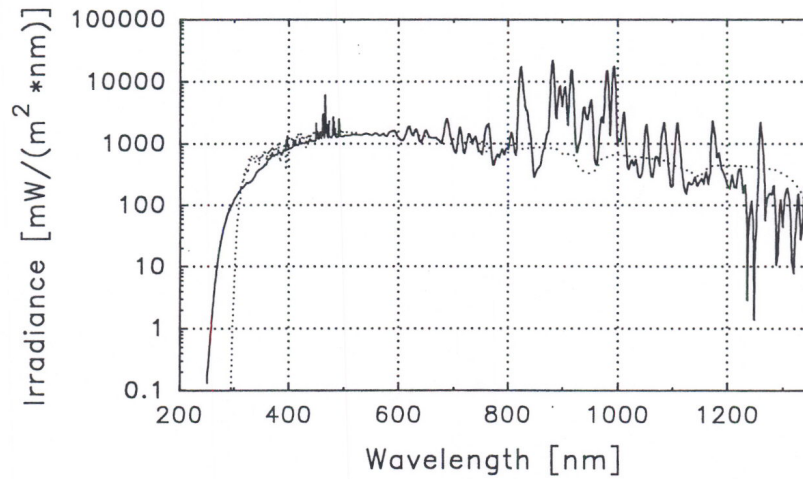
Figure 3.5: Spectral irradiance of a long arc Xenon lamp [51].

Monochromator

SPEX 500M was used as monochromator, whose sketch is illustrated in Fig. 3.6 [52].
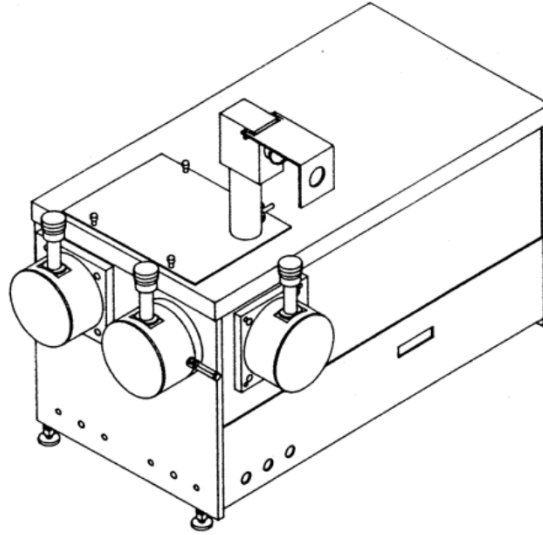
Figure 3.6: SPEX 500M monochromator [52].

A monochromator is an optical device that can produce monochromatic light from wider range of wavelengths available at the input. This is achieved thanks to a reflective diffraction grating, a dispersive optical element consisting of a surface that has a large number of parallel and closely spaced grooves (Fig 3.7) [53].
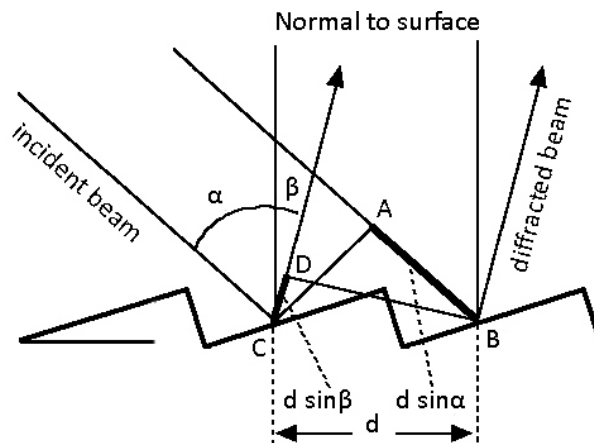
Figure 3.7: Reflective diffraction grating. Adapted from [53].

Each groove becomes a secondary source which emits light at all angles. The light rays

emitted at a certain angle by two adjacent grooves result in constructive interference if the path difference AB - CD (Fig. 3.7) is equal to any integer multiple of the wavelength. This corresponds to the condition described by the grating equation:

$$m\lambda = d \, (\sin\alpha - \sin\beta)$$

where m is the order of diffraction, λ is the diffracted wavelength, d is the distance between successive grooves, α and β are respectively the angle of incidence and the angle of diffraction measured from the grating normal [54, 55].

A grating has a spectral efficiency that depends on the wavelength, that is it is not equally efficient for all wavelengths (in fact the acquired spectrum of a lamp flux is obtained from the convolution of the emission spectrum of the lamp with the efficiency spectrum of the grating employed for the measurement). By controlling the cross-sectional profile of the grooves, it is possible to concentrate most of the diffracted energy in a particular order for a given wavelength. The incident angle and wavelength which correspond to the best diffraction efficiency are called blazing angle and blazing wavelength, respectively [54].

Two different gratings are installed in the monochromator (with blaze at 300 and 1500 nm, respectively), so that the most appropriate one for the wavelength under investigation can be employed. Efficiency spectrum of a 300 nm grating is presented in Fig. 3.8.
The gratings are installed on a rotating system connected to a motor, allowing the selection of the diffracted wavelength that will hit the sample [52].
On the lower side of our monochromator, there is a 5-digit mechanical counter, which displays wavelengths in Ångstroms. A needle-point at right, and white marks on the counter wheel allow the reading up to 0.1 Å. This counter reads the correct value of the wavelength only for 1200 grooves/mm gratings [52]. The two gratings employed have a groove density of 600 grooves/mm, so the counter reading must be multiplied by a factor 2 to obtain the real output wavelength (cf. Sec. 3.2.2).

The entrance and exit slits on the front or at the side of the spectrometer are controlled by a micrometer-type knob above each slit. The slits can be set from 3 µm to 3 mm and are calibrated in 2 µm increments [52]. For these measurements, both the entrance and the exit slits were kept open at their maximum aperture, 3 mm.
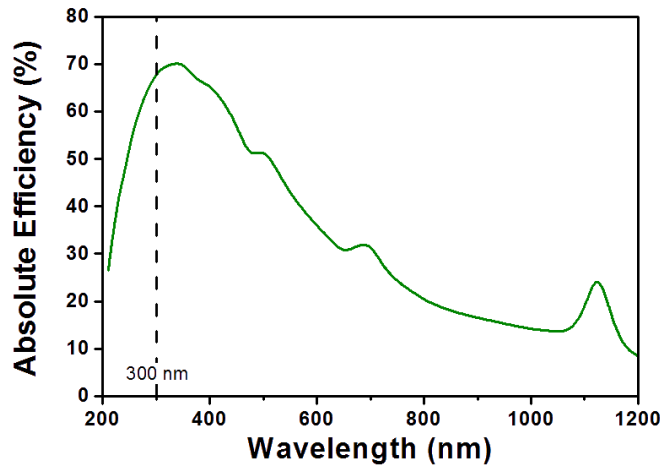
Figure 3.8: Absolute efficiency of 600 grooves/mm 300 nm blaze wavelength grating: maximum efficiency occurs at 300 nm. Adapted from [56].

Pyroelectric sensor

The intensity of transmitted light was measured with a pyroelectric sensor placed behind the sample, as shown in Fig. 3.3 (a).

This sensor is made by a thin pyroelectric material layer with two metal contacts at its ends; pyroelectricity is the property to generate a voltage with changes in temperature. Pyroelectric materials atoms have an intrinsic electric dipole moment; the change in temperature modifies the positions of the atoms within the lattice, such that the polarization of the material changes. This polarization variation gives rise to a voltage across the crystal [57].

The pyroelectric sensor detectivity increases at low frequencies, thus a low frequency was chosen to perform the measurements (cf. Sec. 4.1.2).

Lock-in amplifier

The Stanford Research Systems SR830 lock-in amplifier, shown in Fig. 3.9 [58], reads the output voltage signals.

Lock-in amplifiers are used to detect and measure very small AC signals. Depending on the dynamic reserve of the instrument, a small signal (up to a few nanovolts) can still be reliably detected even when it is obscured by noise sources up to several thousands of times larger [59].

Figure 3.9: Stanford Research Systems SR830 lock-in amplifier [58].

Lock-in amplifiers use a technique known as phase-sensitive detection to single out the component of the signal at a specific reference frequency and phase.

Phase-sensitive detection relies on the orthogonality of sinusoidal functions. Specifically, when a sinusoidal function of frequency ν_1 is multiplied by another sinusoidal function of frequency ν_2, different from ν_1, and integrated over a time much longer than the period of the two functions, the result is zero. Otherwise, when ν_1 is equal to ν_2 and the two functions are in phase, the average value is equal to half of the product of the amplitudes.

Basically, a lock-in amplifier multiplies the input signal by the reference signal, and integrates it over a specified time, usually on the order of milliseconds to a few seconds. The resulting signal is a DC signal, which has no contribution from any noise signals at frequencies different from the reference frequency; these components are rejected and do not affect the measurement [59].

Therefore, lock-in measurements require a frequency reference, in this case provided by the chopper. The experiment is excited at a fixed frequency and the lock-in detects the response from the experiment at the reference frequency.

The lock-in is interfaced to the computer program that controls all the instrumental set-up, which is described in the next section.

3

3.2.2 Data acquisition program

Surface photovoltage spectroscopy (SPS) data acquisition (DAQ) program was developed in the framework of the present thesis work. The program was created using LabVIEW (Laboratory Virtual Instrument Engineering Workbench), which is a software development environment from National Instruments that allows the computer to create an interface between data acquisition hardware.

Programs developed by LabVIEW –which are indeed called Virtual Instruments (VI) and have a *.vi file extension– allow data acquisition, display and storage, but also the development of algorithms, mathematical analyses, and communication tasks that extend beyond data acquisition.

LabVIEW is a software built on a graphical programming language and on the concept of data flow to control program execution. The graphical programming language is represented by function icons connected by virtual wires, which permit data to flow between the function icons.
The execution of the program, therefore, is controlled by the flow of the data. This is conceptually different from text-based programming languages where the execution of the program is determined primarily by the order of the program statements [60].
The LabVIEW environment includes two windows, called Front Panel –the user interface– and Block Diagram, which contains the graphical source code.

A detailed description of the program is presented in the followings lines.
The program is called "SPS_Data_Acquisition.vi", and on its Front Panel several features are present (Fig 3.10):

- a frame for the file path;

- three boxes for `NOTES`, `MONOCHROMATOR` and `LOCK-IN`;

- a display, presenting what the program is doing at the moment;

- a `START` button to start the acquisition;

- a graph which shows data acquisition point by point: once the first point has been collected, it is shown on the graph, which automatically rescales every time a measurement is acquired.
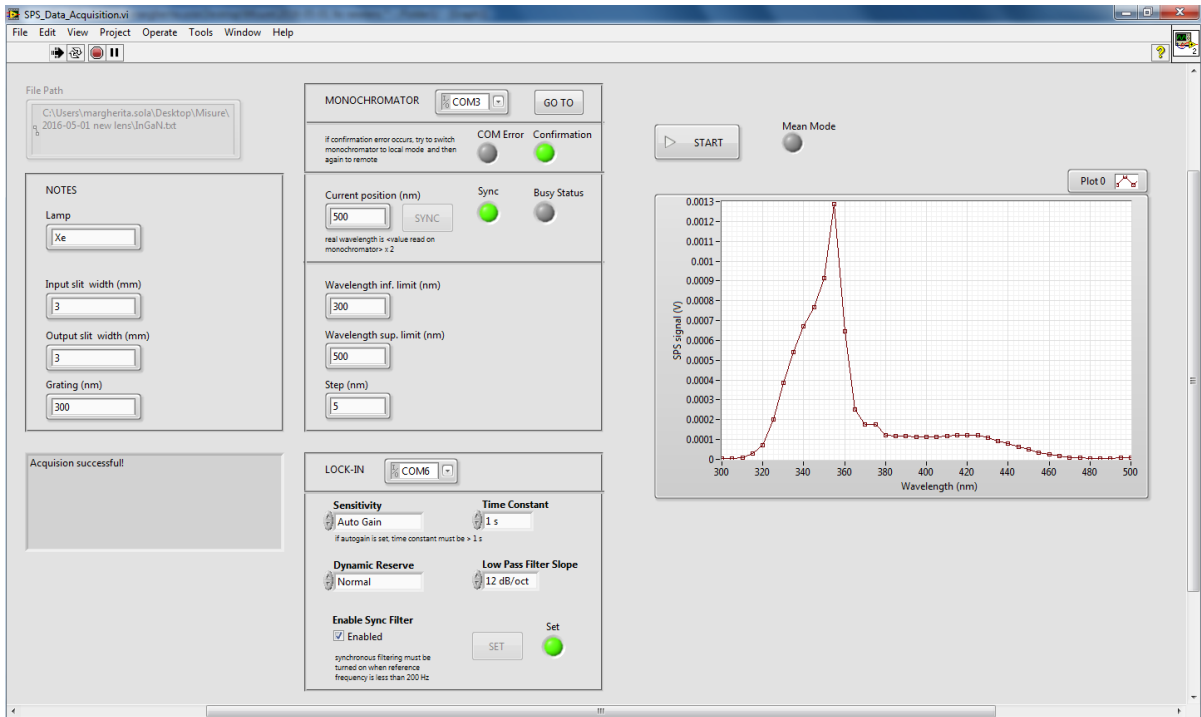
Figure 3.10: Screenshot of the Front Panel of "SPS_Data_Acquisition.vi".

In `NOTES` box, the user can write some information about the experimental set-up, which will be written in the header of the file. The information that the user can insert in the header file is the following: the lamp used as source, the input and output slit width and the grating used in the monochromator.

In `MONOCHROMATOR` box, the instrument is set up. To achieve this aim, the user has to specify which serial port the monochromator SPEX 500M is connected to. The monochromator controller must be set in remote mode, in order to be controlled by the computer. There are some LED indicators in the Front Panel: the `COM Error` LED indicates that there is a problem with the connection to COM port, and `Confirmation` LED indicates that the computer has properly set a communication with the instrument[1]. If `COM Error` or `Confirmation` error occurs, an error message is shown and the program is aborted.

Monochromator must be synchronized by the user, since it does not allow for reading

---

[1]If the monochromator is turned on *after* the computer, it could not recognize the instrument, so it may be useful to switch monochromator to local mode and then again to remote.

its current position; the real wavelength is $\lambda_{obs} \cdot 2$, where λ_{obs} is the value read on the monochromator. This correction is due to the employment of different gratings with respect to the original one[2].

Once `SYNC` button is pressed, the monochromator is synchronized; `Sync` LED indicator turns on and `SYNC` button is disabled and greyed out. The program checks if the user has not forgotten to synchronize the monochromator by not allowing the start of the acquisition if the monochromator is not synchronized. An error message is shown in this case. `Busy status` LED indicates that the monochromator motor is busy, that is the monochromator is moving toward another wavelength. The user must set the inferior and superior limit of the wavelength and the step between two subsequent acquisitions. There are some checks to verify if: (a) the wavelength superior limit set by the user is actually greater then the wavelength inferior limit; (b) the step value set by the user is different from 0 nm; (c) the wavelength inferior limit is greater than or equal to 0 nm; (d) the wavelength superior limit is less than or equal to 3000 nm[3]. The program does not allow the acquisition start if all conditions are not satisfied and in these cases one or more error messages are shown.

If the user simply needs to move the monochromator without starting an acquisition, it is possible to press `GO TO` button and the program opens a dialog window with a sub-VI (Fig. 3.11). `COM Error` and `Confirmation` LED indicators are present, the same as those explained above. If `COM Error` or `Confirmation` error occurs, an error message is shown and the program is aborted.

The user has to specify `Current position` and the wavelength to `Go to`. If `Current position` was already specified in the main program, its value is automatically updated in the sub-VI. After pressing `GO` button, the monochromator moves to the specified wavelength, then `Current position` value is updated. The user could then specify another `Go to` value and press `GO` button again. When the user does not need to move the monochromator any more, `ESC` button takes him back to the main program, and `Current position` value is updated in the main panel too.

In `LOCK-IN` box, the instrument is set up. Within this aim, the user has to specify

---

[2]The original grating has a groove density of 1200 grooves/mm, while the two gratings employed have a groove density of 600 grooves/mm.

[3]The reason of these last two checks is that the scanning drive has limit stop switches and the user should avoid scanning to the ends of the drive. The normal range operation is 0-3000 nm.
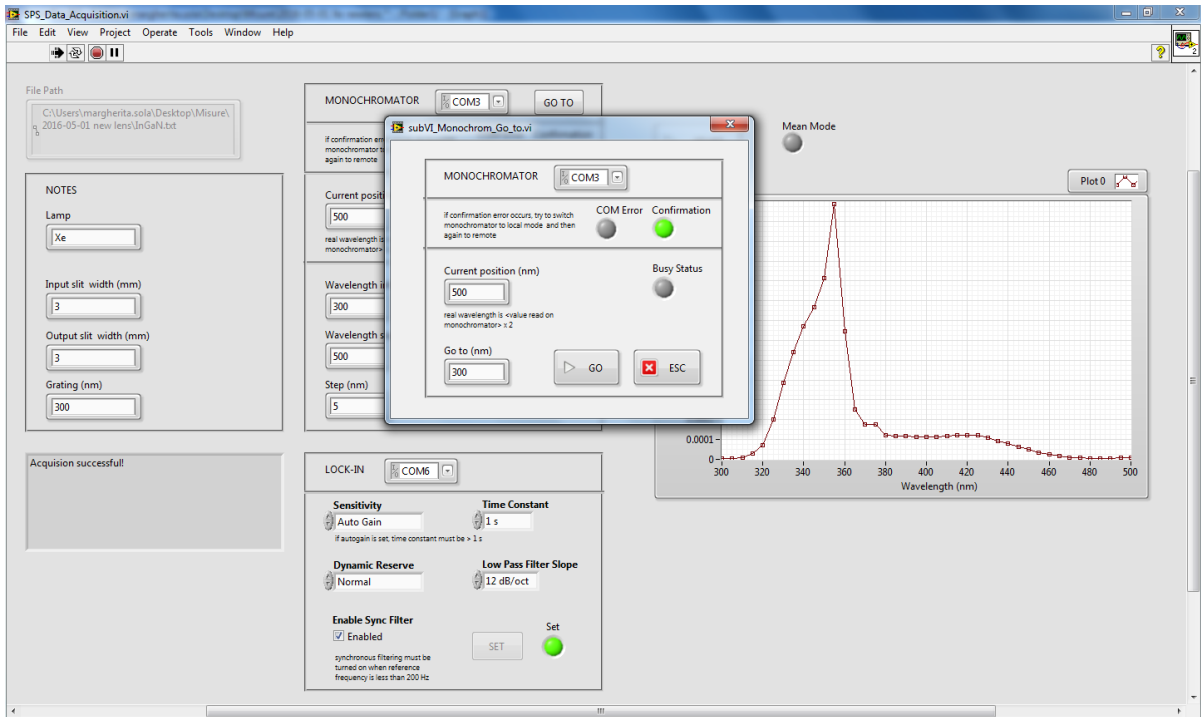
Figure 3.11: Screenshot of the Front Panel of the sub-VI to move the monochromator.

which serial port lock-in SRS830 is connected to. The user must set lock-in parameters (`Sensitivity`, `Time Constant`, `Dynamic Reserve` and `Low Pass Filter`) from drop down lists, and must select to `Enable Sync Filter` or not[4]. Once `SET` button is pressed, the lock-in is set up; `Set` LED indicator turns on and `SET` button is disabled and greyed out. The program checks if the user has not forgotten to set up the lock-in by not allowing the start of the acquisition if the lock-in is not set. An error message is shown in this case.

After all these steps are carried out, the user can start acquisition of the signal by pressing the `START` button.

The program requires the choice of the directory and the file name where data will be stored. It is recommended to add a *.txt file extension in order to help Windows and Origin to recognize the type of file. When the file name is chosen, data acquisition begins.

The display shows what is happening at that moment. If the acquisition is running

---

[4]Synchronous filtering must be turned on when reference frequency is less than 200 Hz.

smoothly, the user can read the sentences written in Tab. 3.2:

- *Monochromator setup in progress...* - *Monochromator setup completed.*	Monochromator has gone to the wavelength inferior limit, then `Current position` value is updated.
- *Lock-in setup in progress...* - *Lock-in setup completed.*	Lock-in is in the remote state (remote indicator on lock-in front panel turns on, keyboard and knob are locked out except for the [Local] key which returns the lock-in to local state). Lock-in parameters have been set.

Table 3.2: Sentences shown on the display while the program is running.

If *Auto Gain* has been selected for `Sensitivity`, the program starts an autoscale procedure described in the followings:

- if the value read by the lock-in is greater than 90% of the current full-scale, the program switches the lock-in to the upper scale;

- if the current value is less than 60% of the previous full scale, the program switches the lock-in to the lower scale.

The previous two steps are repeated until the measured value is within the range between the 60% of previous full-scale and 90% of current full-scale. In this case, the program considers the current scale appropriate for acquisition.

This range was chosen to be wide enough to avoid the risk that the program would continuously change the scale to find the appropriate one, chasing the signal when it is unstable. Moreover, if the signal is very unstable, it is better to use a slightly larger scale than the smallest possible, in order not to change the scale continuously (lock-in takes a certain time to hang up the signal and to provide a reliable measurement every time the scale is changed).

It is recommended to select *Auto Gain* for `Sensitivity` for two reasons: 1) a correct data acquisition –at the best sensitivity at every step– and 2) the preservation of the lock-in. Before running the program, it is recommended to manually set the appropriate scale, not to force the program to change a lot of scales to find the correct one.

Then, the program checks the stability of the signal: it is considered stable enough if it does not have variations greater than 8% for at least 5 consecutive acquisitions (the program reads one value per time constant). In this condition, the program writes on the file the mean value of the last 5 read values[5]. If stability does not occur for over 25 seconds, which is a reasonable value according to experience, the program switches to *mean mode* and `Mean Mode` LED indicator turns on.

If *mean mode* is active, the program reads 10 values and writes their average value on the file. In this way, data acquisition can go on even if the signal is very unstable, though much more slowly[6]. In this case, however, measurement uncertainty is much greater.

After writing the values on the file, the monochromator is moved to next wavelength and `Current position` value is updated. The program waits for a time constant to let the signal become stable, then restarts the autoscale procedure and continues the acquisition in the way described above.

Data acquired are shown in real time on a graph, which automatically rescales during the measurement.

At the end of the acquisition, the program confirms the success of the operation using a pop-up that says "Acquisition successful!" and the display shows the same sentence. The program also beeps once to notify the end of the operation if the user is not looking at the computer.

Data acquisition generates a text file having the following structure:

- a header of 5 lines, all beginning with # character, where the date and the information in `NOTES` box are written;

- a line with column titles which are: the `wavelength(nm)`; the abscissa `X(V)`, the ordinate `Y(V)`, the module `R(V)` and the phase angle `theta(deg)` of the signal; the reference (chopper) `frequency(Hz)`; a quantity called `waitForStable(unit=time constant)`, which is the number of time constants the program has waited before

---

[5]When the program acquires values from the lock-in, 5 quantities (X, Y, R, phase and reference frequency) are read simultaneously (see SNAP function from SR830 manual) and data are recorded in a vector. The arithmetic mean is performed on each element of the vector.

[6]Speed of data acquisition depends critically on the stability of the signal, so it is recommended to check periodically the frequency of the chopper.

judging the signal stable and then acquiring its value. This quantity can range from 5 (if the signal is stable) to 25, or the value 999 is stored in the case of mean mode acquisition;

- data stored in columns separated by spaces[7].

Step by step instructions

1. Turn on the lamp, the chopper, both monochromator controllers, the lock-in and the computer. Set monochromator to remote mode, in order to control it from the computer. Once lock-in is initialized, set manually the appropriate scale to fit the signal.

2. Open and run "SPS_Data_Acquisition.vi".

3. Fill in `NOTES` box with the information on the experimental set-up: the lamp used as source, the input and output slit width and the grating used in the monochromator.

4. In `MONOCHROMATOR` box, write $\lambda_{obs} \cdot 2$ as `Current position` and press `SYNC` button. Set `Wavelength inf. limit`, `Wavelength sup. limit` and `Step`.

5. In `LOCK-IN` box, set lock-in parameters (`Sensitivity`, `Time Constant`, `Dynamic Reserve` and `Low Pass Filter`) from the drop down lists, and select to `Enable Sync Filter` or not; press `SET` button.

6. Press `START` button.

7. Choose the directory and the name of the file where data will be saved. It is recommended to add a *.txt file extension in order to help Windows and Origin to recognize the type of file.

---

[7]The decimal separator used is the point.

3.2.3 Atomic Force Microscopy

Atomic force microscopy (AFM) technique has been used to perform morphological and electrical measurements on the samples.

In AFM, a sharp tip (typically with a curvature radius of a few nm) is mounted at the free end of a very small cantilever. The tip is positioned close to the sample, at a variable distance depending on the mode of operation. The forces between the tip and the sample generate a measurable deflection of the cantilever, according to the Hooke's law [61]. The interactive forces between the tip and the sample can be modelled as Van der Waals forces between two atoms at a distance r, described by the Lennard-Jones potential (whose qualitative shape is shown in Fig. 3.13):

$$V(r) = 4\varepsilon \left[\left(\frac{\sigma}{r} \right)^{12} - \left(\frac{\sigma}{r} \right)^{6} \right]$$

where ε is the depth of the potential well, and σ is the diameter of the sphere which approximates the atom in a rigid sphere model. The first term describes the attractive force at a large distance, while the second is related to the short range repulsion [62].
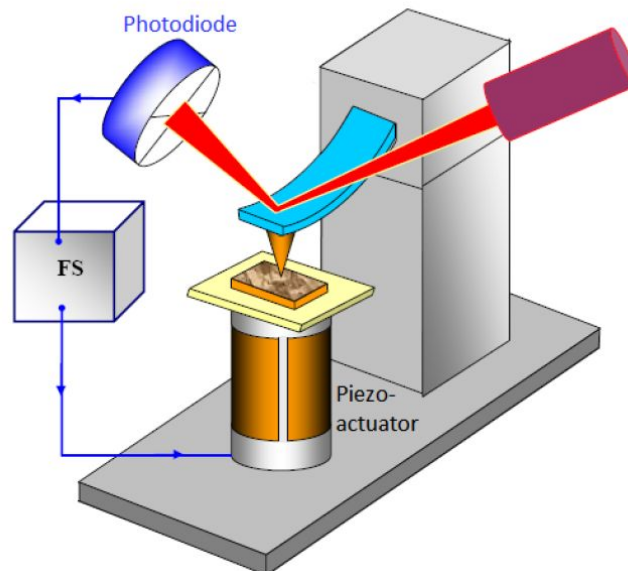
Figure 3.12: Schematic representation of AFM set-up.

Hence, AFM measures the interactive force between the tip and the sample, by the deflection of the cantilever. This deflection is calculated by monitoring the deviation of a laser beam reflected from the top part of the cantilever using a 4-sector photodetector (which can precisely distinguish and estimate both vertical and lateral deflection of the cantilever).

The ability to position the tip with extremely high precision is usually achieved using piezo-electric actuators, which means that the material generates a bias when it is subjected to a mechanical deformation, and vice versa [63]. Feedback circuits are used to control the bias applied to the piezo-electric transducer, and hence to maintain parameters with constant values (for example the cantilever deflection), depending on which AFM operation mode is used to perform the measurements.

AFM set-up is sketched in Fig. 3.12.

The AFM operation modes are:

- contact mode: the AFM tip is in constant contact with the sample and the deflection of the cantilever is kept constant during scanning;

- non-contact mode: the oscillation of the cantilever is set at a frequency close or equal to its resonance one. The interactive forces between the tip and the sample modify the cantilever resonant frequency, so that the cantilever's amplitude of vibration decreases for a fixed drive frequency;

- semi-contact mode (or tapping mode): the oscillation of the cantilever is set at a frequency close to its resonance one, in such a way that it is in contact with the sample at every period. In this way the sample surface and the tip are much less damaged than in the contact mode [64].

Fig. 3.13 shows the inter-atomic force modelled as Lennard-Jones potential vs. AFM operation modes tip-sample distance [65].

Atomic force microscopy, which has provided scientists with unprecedented access to the nanoscale structure of materials, has proved to be enormously adaptable and it is now used to measure several other properties besides topography: i.e. mechanical, electrical and magnetic characteristics [61, 66].
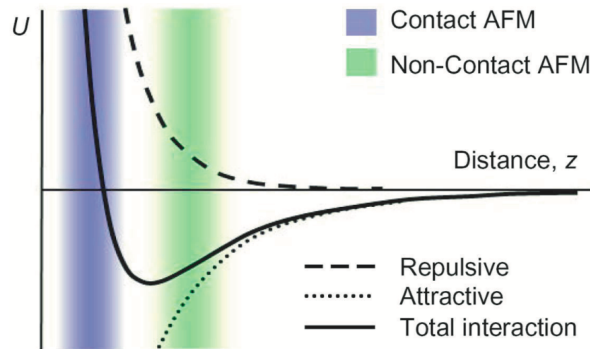
Figure 3.13: Interatomic force modelled as Lennard-Jones potential vs. AFM operation modes tip-sample distance [65].

Electrical Force Microscopy

The intuition which led to the development of electrical force microscopy (EFM) and various related techniques is the possibility of using the AFM tip to measure other local forces besides Van der Waals interaction between the tip and the sample measured in topographic imaging [61].

EFM maps electric properties on a sample surface (such as the surface potential or charge distribution) by measuring the electrostatic force between the surface and the tip, which is biased. However, in addition to the electrostatic force, Van der Waals forces between the tip and the sample surface are always present and their magnitude change according to the tip-sample distance.

The resulting signal combines information of both surface topography (Topo signal, generated by Van der Walls forces) and surface electrical property (EFM signal, generated by the electrostatic forces).

Effective EFM imaging can be obtained if the EFM signal is successfully separated from the entire signal. This can be achieved using two different modes for maps acquisition, based on the two following considerations [61, 67].

The first EFM mode is the Force Range technique, which relies on the fact that the two forces involved have different dominant regimes. Van der Waals forces are proportional to $\frac{1}{r^6}$, while electrostatic forces are proportional to $\frac{1}{r^2}$, where r is the tip-sample distance. Thus, Van der Waals forces are dominant when the tip is close to the sample, while they rapidly decrease as the tip is moved away, when electrostatic forces become dominant.

In the Force Range technique, the first scan is performed near the sample, in the region where Van der Waals forces are dominant. Then, the tip-sample distance is increased to place the tip where electrostatic forces are dominant and the EFM image is acquired, as shown in Fig. 3.14 (a) [67].

The second EFM mode is the Two Pass technique, which relies on the fact that the topography line is the line of the constant tip-sample distance, which equals the line of constant Van der Waals forces. In the Two Pass technique, the first scan is performed to obtain the topography by scanning the tip near the surface; in the second scan (known as the lift scan), the tip-sample distance is increased in order to place the tip in the region where electrostatic forces are dominant. The tip is then biased and scanned without feedback, following the height profile recorded in the previous scan, so that the tip-sample distance, and hence Van der Waals forces applied to the tip, should be kept constant, as shown if Fig. 3.14 (b). Thus, the only source of the signal variation is the change of the electrostatic force [61, 67].
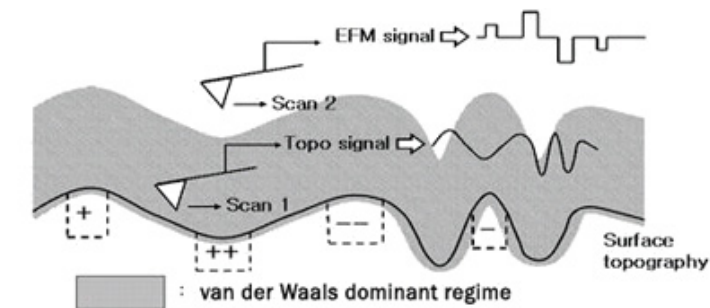
(a)
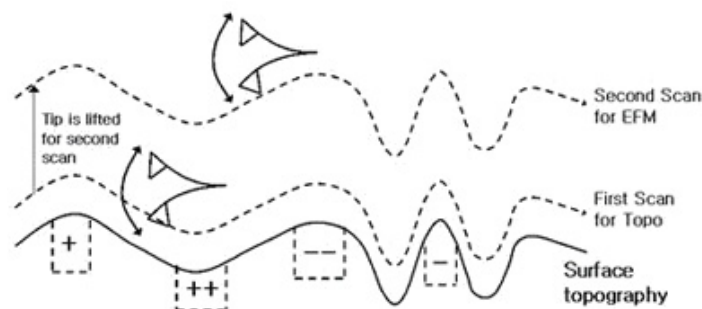
(b)

Figure 3.14: Schematics of (a) Force Range technique and (b) Two Pass technique [67].

The voltage between the tip and the sample $V(t)$ can be expressed by the following equation:

$$V(t) = V_{\text{DC}} - V_{\text{S}} + V_{\text{AC}} \, sin\omega t$$

where V_{DC} is the DC bias applied to the tip, V_{S} is the surface potential on the sample and V_{AC} is the AC bias of frequency ω applied to the tip [67].

In fact, the potential difference applied to the tip has both a DC and an AC component; a lock-in amplifier is connected to the system to apply the AC bias to the tip (in addition to the DC bias applied), and it is also used to separate the ω frequency component from the output signal [61, 67].

In order to derive an expression for the electrostatic force F acting on the tip, the tip and sample may be modelled as a parallel plate capacitor, hence:

$$F = Q \, E = Q \, \frac{V}{d} = C \, \frac{V^2}{d}$$

where Q is the charge, E is the electric field, C is the local capacitance between the tip and the sample, V is the voltage difference and d the distance between the plates of this capacitor (tip-sample) [67].

The force then becomes:

$$
\begin{aligned}
F(t) &= \frac{C}{d} \, (V(t))^2 = \\
&= \frac{C}{d} \, \left[(V_{\text{DC}} - V_{\text{S}})^2 + (V_{\text{AC}} \, sin\omega t)^2 + 2 \, (V_{\text{DC}} - V_{\text{S}}) \, V_{\text{AC}} \, sin\omega t \right] = \\
&= \frac{C}{d} \, \left[(V_{\text{DC}} - V_{\text{S}})^2 + V_{\text{AC}}^2 \, \frac{1}{2} \, (1 - cos2\omega t) + 2 \, (V_{\text{DC}} - V_{\text{S}}) \, V_{\text{AC}} \, sin\omega t \right] = \\
&= \frac{C}{d} \, \left[(V_{\text{DC}} - V_{\text{S}})^2 + \frac{1}{2} V_{\text{AC}}^2 \right] + 2 \, \frac{C}{d} \, (V_{\text{DC}} - V_{\text{S}}) \, V_{\text{AC}} \, sin\omega t - \frac{1}{2} \, \frac{C}{d} \, V^2_{\text{AC}} \, cos2\omega t.
\end{aligned}
$$

There are three terms in this final summation, that can be referred to the DC term, the ω term, and the 2ω term, respectively. Thus, the total cantilever deflection signal, which represents the force between the tip and sample, can be analysed in its separate components.

The DC part derives from Van der Waals interaction between the tip and the sample, and the AC part with a frequency of ω and 2ω reflects the electrostatic properties and the capacitive properties of the sample, respectively [67].

One common variant of EFM is scanning Kelvin probe microscopy (SKPM - sometimes referred to as surface potential microscopy), in which the DC bias is controlled by a feedback circuit, with the aim to cancel out the ω term.

The SKPM manages in a different way the ω signal obtained from the lock-in amplifier. The DC bias applied to the cantilever is controlled so that the ω signal from the lock-in amplifier is maintained to zero. As discussed above, the ω term is equal to:

$$2 \, \frac{C}{d} \, (V_{\mathrm{DC}} - V_{\mathrm{S}}) \, V_{\mathrm{AC}} \, sin\omega t.$$

Therefore, the signal goes to zero when $V_{\mathrm{DC}} = V_{\mathrm{S}}$, that is when the DC bias applied to the cantilever is equal to the surface potential. It is worth mentioning that the surface potential V_{S} corresponds to the V_{CPD}, which is defined as the difference in the work functions of the two materials, the tip one and the sample one (cf. Sec. 2.2.1).

A feedback loop varies the DC offset bias such that the output of the lock-in amplifier that measures the ω signal is zero. This value of the DC offset bias that cancels out the ω signal becomes then a measurement of the surface potential. Repeating this procedure in consecutive points of the sample, a surface potential map can be acquired [61, 67, 68]. An example of such a map compared to the corresponding topographic image is shown in Fig. 3.15 [68].
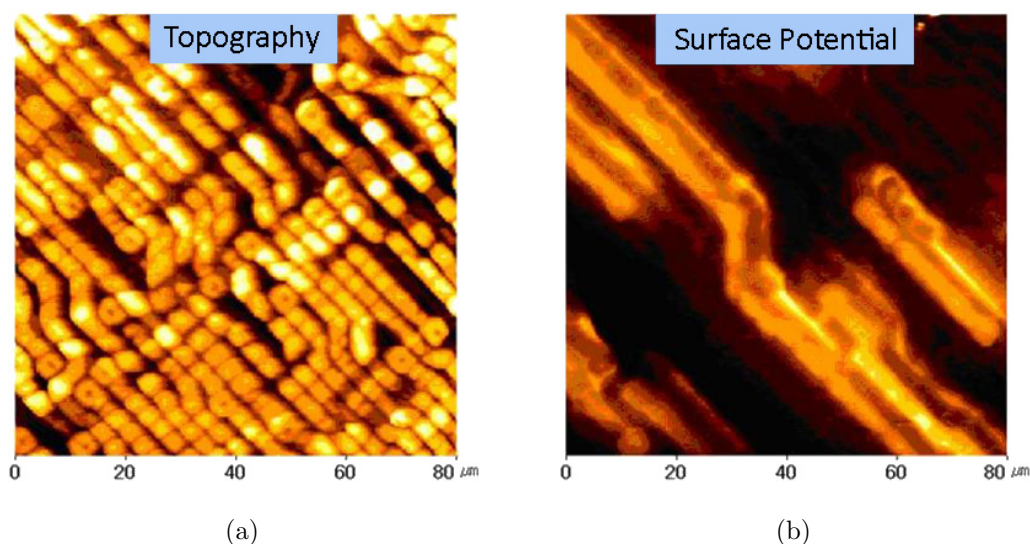
Figure 3.15: (a) Topography and (b) surface potential of an integrated circuit [68].

The system used for the purpose of this thesis is a Park NX10, in ambient atmosphere at room temperature. Non-contact mode was employed for the topographic mapping, and Force Range technique for electrical characterization.

Nanosensors SSS-NCHR tips (Super Sharp Silicon- Non-Contact mode - High resonance frequency - Reflex coating) and Nanosensor PPP-NCSTAu tips (Point Probe Plus Non-Contact / Soft Tapping mode - Au coating) were employed for morphological and electrical maps, respectively. Clearly, the tips used for electrical characterization are coated with gold since a metallic tip is required.

The super sharp tips have a guaranteed curvature radius less than 5 nm, while the Au coated tips have a typical curvature radius less than 50 nm, as shown in the SEM images in Fig. 3.16 [69, 70].

(a)   (b)
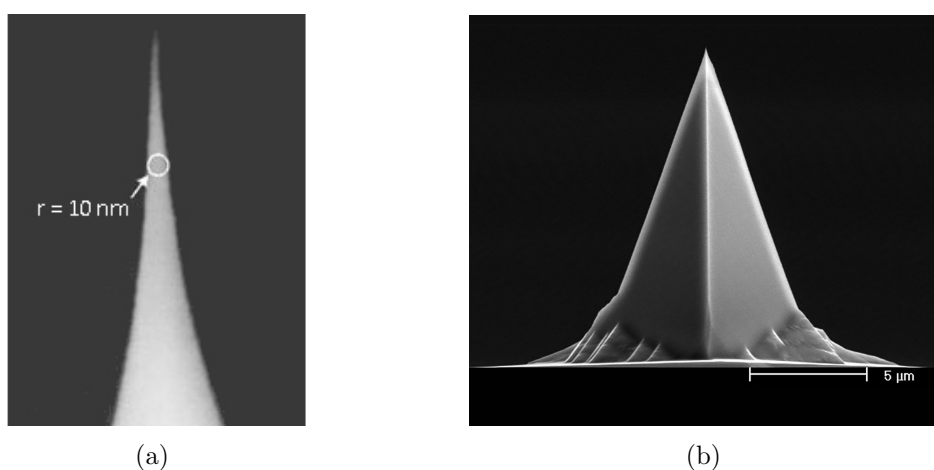
Figure 3.16: SEM images of: (a) SSS-NCHR tip [69]; (b) PPP-NCSTAu tip [70].

3.2.4   Image processing and analysis

To acquire non-distorted images of the sample, AFM software usually includes specific routines for image analyses. An open-source software called Gwyddion has been employed to obtain all analyses of the samples, for its versatility and completeness [71].

Surface images usually show a slope: it may be a result of a tilted installation of the sample onto the scanner or caused by non-flatness of the sample itself. This slope takes a large portion of z-axis when the image is inclined, causing a loss in the clearness of small image details. This is the reason why one of the first processes applied to raw

AFM data is usually plane levelling.

The continuous changes in the tip-sample distance during scanning create another distortion, due to the micro-movements in elements of the head structure or to micro-particles from the ambient captured by the tip apex. These events produce steps parallel to the scanning direction on the acquired image. These defects can be removed by a procedure of line-by-line average [71].

Fourier filtering can be also used, in order to eliminate luminous spots linked to periodic noise sources in the Fourier transform image [71].

After all image processing is done, morphological analysis has been performed on topography maps. Gwyddion does extract statistical parameters of surface roughness from AFM maps.

Considering a map as a matrix, numerical characteristics of each row or column can be extracted as functions of their position and an average value with its error (standard deviation) is directly calculated. The Root Mean Square Roughness RMS can be obtained as the square root of the arithmetic mean of the square of the vertical deviation from the average height:

$$\text{RMS} = \sqrt{\frac{1}{N} \sum_{j=1}^{N} (r_j - \bar{r})^2} \qquad (3.1)$$

where N is the number of pixels on a row/column, r_j is the value of the j-th point and $\bar{r}$ is the average height [71].

For the EFM and SKPM maps, Gwiddion simply extracts the average value of the measured bias from selected regions of the image.

Chapter 4

Results

In the present chapter the experimental results will be reported.

First of all, in Sec. 4.1 results of the experimental set-up optimization are presented. Secondly, Sec. 4.2 and 4.3 report the results of the transmittance and SPV measurements respectively. At last, morphological and electrical AFM analysis will be described in Sec. 4.4.

The sample investigated in this work were deposited by sputtering or solgel procedures at the MaCEPV (Materials for electronic and photovoltaic devices) laboratory, iCube, CNRS, Université de Strasbourg. The sample characteristics and labels are reported in Tab. 4.1.

- LVO22Q: 55 nm $LaVO_3$ on quartz (sputtering)

- LVO24S: 55 nm $LaVO_3$ on Si (sputtering)

- LVOsg2Q: 36 nm $LaVO_3$ on quartz (solgel)

- LVO7Q: ZnO (100 nm) // $LaVO_3$ (100 nm) // quartz (sputtering)

- LVO14Q: ZnO (100 nm) // $LaVO_3$ (130 nm) // quartz (sputtering)

Table 4.1: Characteristics and labels of the $LaVO_3$ samples.

The last two samples have a layered structure; ZnO does not completely cover the $LaVO_3$ layer, since it is deposited only on a part of the sample, as shown in Fig. 4.1.
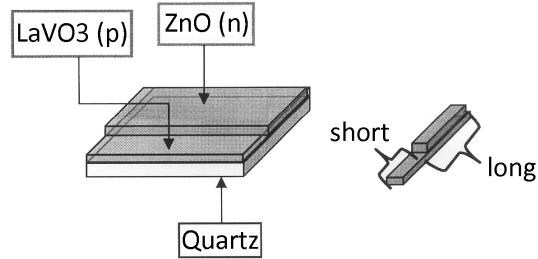
Figure 4.1: LaVO$_3$/ZnO samples structure.

4.1 Experimental set-up optimization

One of the aims of this thesis was the implementation of the experimental set-up and of the related software, since they did not exist before. Therefore, several preliminary tests were carried out for the optimization of the experimental set-up.

4.1.1 QTH and Xe stability test

First of all, the stability of the two lamps used as light sources has been tested.
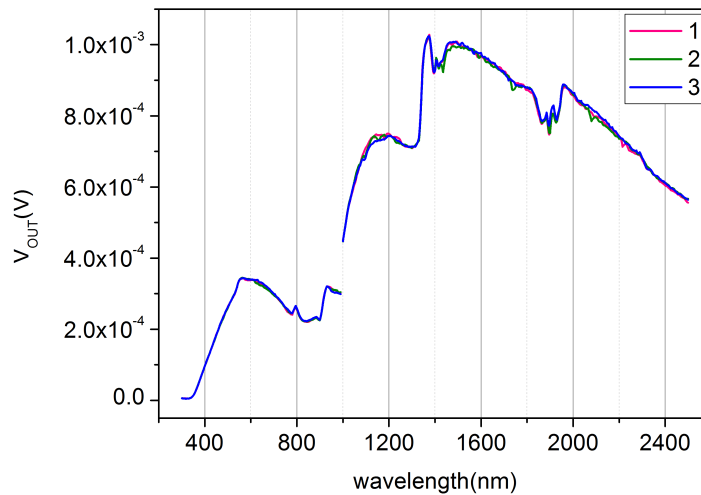
Figure 4.2: Three acquisitions (1, 2, 3) of the QTH flux. V$_{OUT}$ is the output voltage signal measured by the pyroelectric sensor.

In Fig. 4.2 three successive acquisitions of the QTH flux are shown. The spectral dependence of the output signal shows the presence of two maxima, this is due to the convolution of the QTH emission spectrum with the grating efficiency spectrum (cf. Sec. 3.2.1). The discontinuity in the spectra is due to the fact that two different gratings are used as the wavelength varies: the 300 nm grating for shorter wavelengths (range 300-1000 nm) and the 1500 nm grating for longer wavelengths (range 1000-2500 nm), as explained in Sec. 3.2.1.

The mean relative error obtained from these data is less than 1% for both ranges; the conclusion is that the QTH lamp is definitely stable. As expected, the relative error is higher for the range 300-1000 nm, where the flux intensity is smaller. In particular, the relative error reaches a maximum for wavelengths corresponding to a very low flux.

In Fig. 4.3 three successive acquisitions of the Xe flux are shown. The mean relative error obtained from these data is slightly higher than the one obtained from QTH fluxes, and, as expected, the relative error reaches a maximum for wavelengths corresponding to a very low flux, as for the previous case.
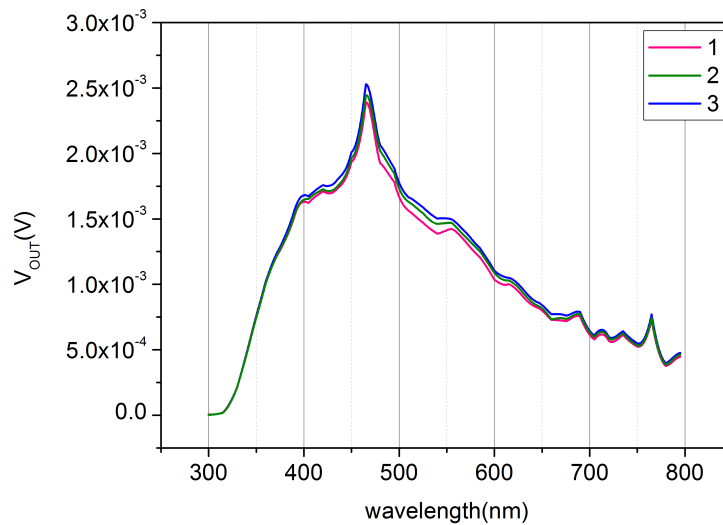
Figure 4.3: Three acquisitions (1, 2, 3) of the Xe flux. V_{OUT} is the output voltage signal measured by the pyroelectric sensor.

The obtained values are reported in Tab. 4.2.

67

lamp	range (nm)	mean relative error	maximum relative error
QTH	300-1000	0.009	0.094
QTH	1000-2500	0.006	0.024
Xe	300-800	0.026	0.088

Table 4.2: Mean and maximum relative errors of the photon flux signals.

4.1.2 Pyroelectric sensor functionality test

As already explained in Sec. 3.2.1, the pyroelectric sensor has a better detectivity at low frequencies. The output signal of the pyroelectric detector has been measured for different frequencies in the spectral range 1500-1600 nm; the results are shown in Fig. 4.4. The signal increases by lowering the frequency, as expected. The frequency for all subsequent measurements performed with the pyroelectric sensor was set at 13 Hz, a good compromise to avoid loss in the noise suppression efficiency of the lock-in.
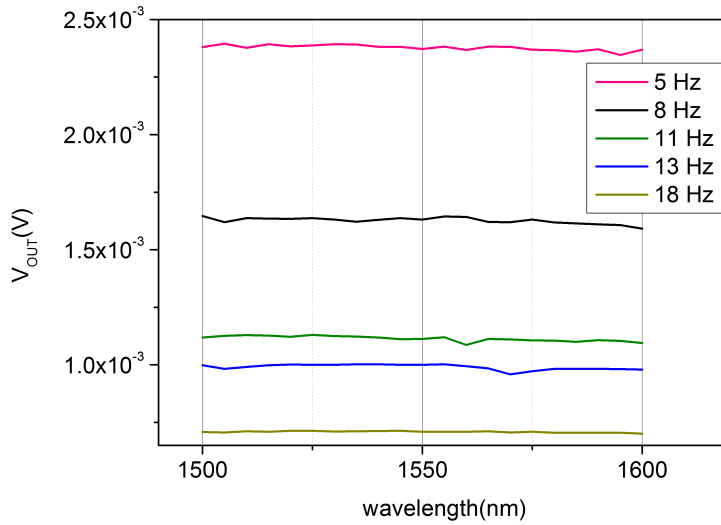
Figure 4.4: Acquisitions of the same signal for different chopper frequencies. V_{OUT} is the output voltage signal measured by the pyroelectric sensor.

4.1.3 Monochromator set-up test

As shown in Figure 4.5, the monochromator has 3 openings. Opening 1 is used for the input light beam, while the others can be used (one at a time) for the output. This
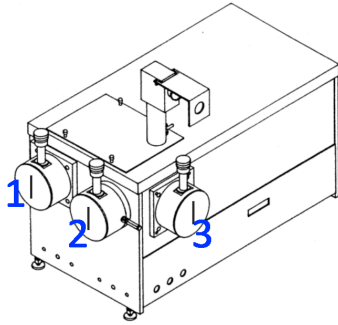
Figure 4.5: SPEX 500M monochromator [52]. The three openings are indicated.

choice is due to the fact that there could not be enough space for the detection device on the front (exit 2), because of the presence and dimensions of the lamp, while there is much more freedom for other geometries on the side (exit 3). For example, the SPV measurement device must be placed at the side exit 3, due to space limitations, while the pyroelectric sensor may be placed at both exits. The monochromator grating is placed in such a way to reflect the photon beam towards the front; a semi-reflective mirror is present in the optical system in order to deflect the light beam towards the side. It is then necessary to verify the mirror effects on the output light beam. In addition, a focussing lens can be placed at the chosen exit, before the pyroelectric detector.
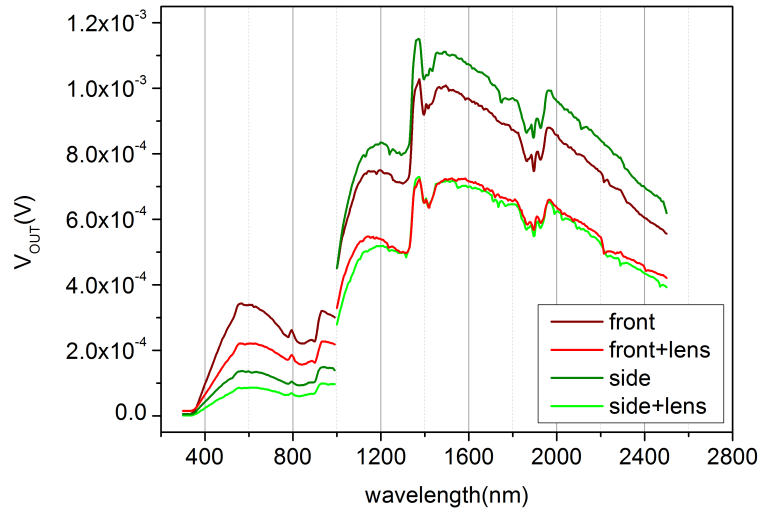
Figure 4.6: Photon flux from the QTH lamp signals for different monochromator set-ups: front (dark red), front+lens (light red), side (dark green), side+lens (light green). V_{OUT} is the output voltage signal measured by the pyroelectric sensor.

69

The QTH signal has different trends in the two ranges 300-1000 nm and 1000-2500 nm (Fig. 4.6). In the 300-1000 nm range, the signals measured with the lens are lower than those with no lens, both employing the front and the side opening (maintaining the same shape). Also, the signals collected from the side are smaller than the front ones.

For the higher wavelengths (1000-2500 nm range), the signal is greater on the side, slightly lower on the front and even lower in both conditions when the lens is added. These differences are due to the absorption by the mirror and the lens, but also to different optical path travelled by the light beam in the two different configurations.
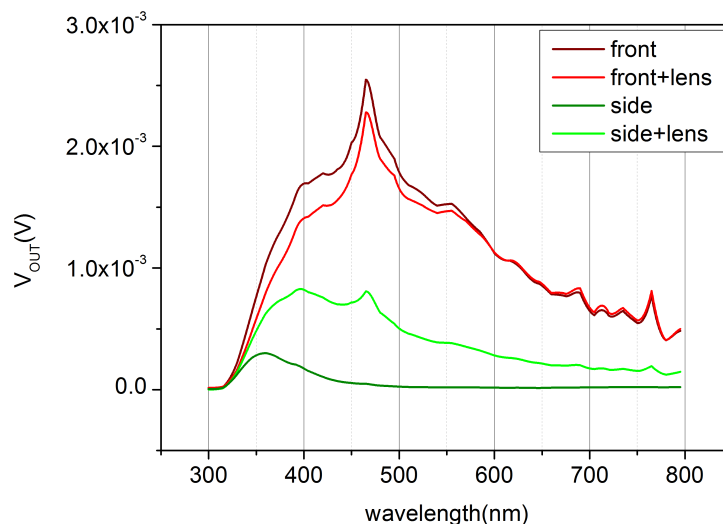
Figure 4.7: Photon flux from the Xe lamp signals for different monochromator set-ups: front (dark red), front+lens (light red), side (dark green), side+lens (light green). V_{OUT} is the output voltage signal measured by the pyroelectric sensor.

The Xe signal (300-800 nm) in different configurations is described in Fig. 4.7. It is very high on the front, and much smaller on the side where its shape also changes: the mirror does absorb in this range of wavelengths but differences are also due to different optical paths. Moreover, a difference in the lens focalization, which gives better performance on the Xe lamp, is explained since the trend of the spectral dependence of the photon flux is different for the two lamps.

Therefore, since the mirror has a spectral dependence, i.e. it is not a neutral optical element, it can be concluded that measurements cannot be performed with a fixed system

configuration with pyroelectric sensor on the front and SPV device on the side. All measurements must be performed on the same side.

4.2 Transmittance measurements

Before SPV analysis, optical absorption spectral measurements were performed, in order to identify the bandgap and the spectral range of interest for SPV.

4.2.1 System functionality test

Before measuring the LaVO$_3$ samples, the system was tested with a crystalline-Si sample whose optical properties are well known. Fig. 4.8 (a) depicts the Si transmission spectrum compared to the QTH flux and Fig. 4.8 (b) the normalized signal, that is the transmittance, obtained by the ratio of the transmitted photon flux with the incident photon flux.
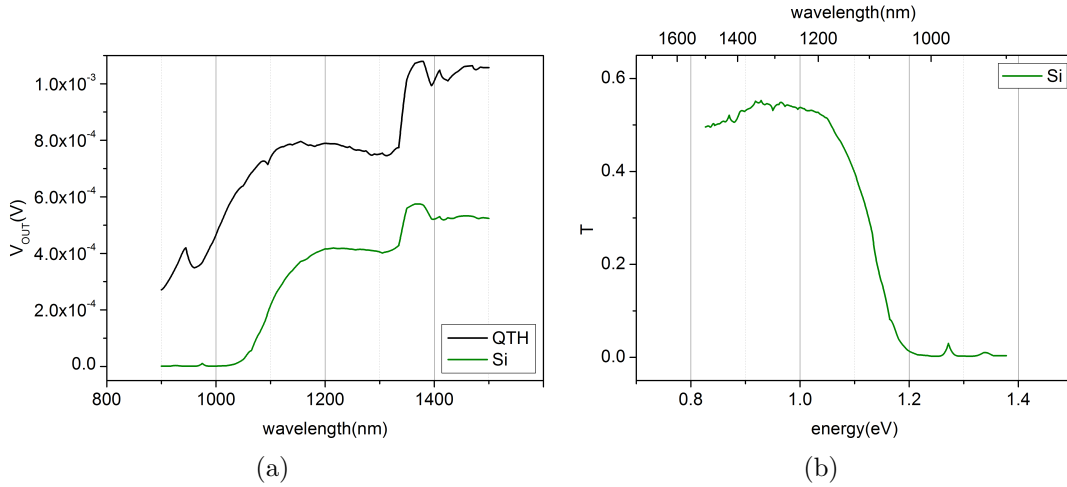
Figure 4.8: (a) Si transmission spectrum (green) over the QTH flux (black). V$_{\text{OUT}}$ is the output voltage signal measured by the pyroelectric sensor. (b) Si transmittance.

Then, the absorption coefficient α was calculated by the following equation:

$$\alpha = \frac{1}{d} \, ln \left(\frac{1}{T} \right) \tag{4.1}$$
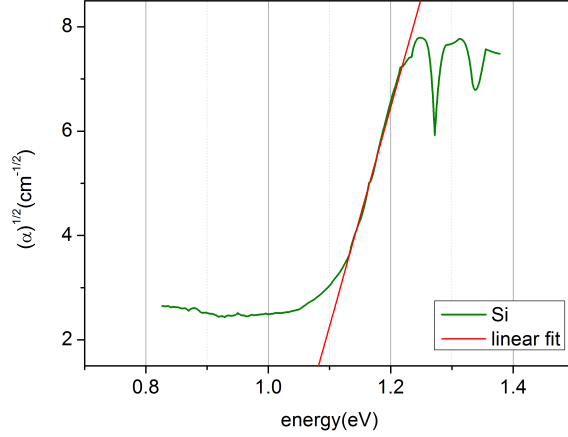
Figure 4.9: Si $\alpha^{\frac{1}{2}}$ plot as a function of energy $h\nu$ of the impinging photons. The intersection of the linear fit (red line) with the x-axis gives the value of the energy gap.

where d is the thickness of the layer and T is the transmittance [72].

As Si is an indirect gap semiconductor, a linear fit in the high absorption region of $\alpha^{\frac{1}{2}}$ as a function of energy $h\nu$ of the impinging photons has been performed (Fig. 4.9) in order to obtain the bandgap value E_g following the relation:

$$\alpha^{\frac{1}{2}} \propto (h\nu - E_\mathrm{g}). \tag{4.2}$$

Thus, the intersection of the linear fit with the x-axis gives the bandgap value. The obtained value of E_g is 1.04 ± 0.03 eV, which is consistent with expectations from the literature. Then, the conclusion is that the system test has been successful.

4.2.2 LaVO$_3$ transmittance measurements

LaVO$_3$ transmittance measurements were performed firstly on LVO22Q sample.

Fig. 4.10 (a) depicts the LVO22Q transmission spectrum compared to the QTH flux and Fig. 4.10 (b) the transmittance. The measurement does not give a clear indication of the energy gap, likely due to the sample thickness. It seems that the sample may be too thin to absorb enough photons to produce a measurable signal.

Therefore, in order to get a higher signal, Xe lamp was used because of its higher flux, and transmittance measurements were performed on a different sample, LVO7Q, which is about twice thicker than LVO22Q (see Tab. 4.1). Since a different spectral range can
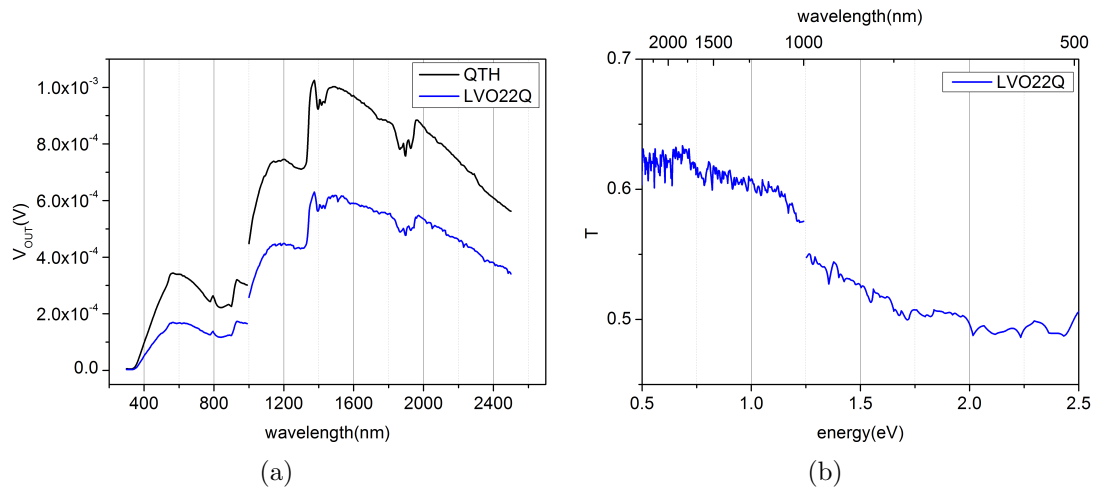
Figure 4.10: (a) LVO22Q transmission spectrum (blue) compared to the QTH flux (black). V_{OUT} is the output voltage signal measured by the pyroelectric sensor. (b) LVO22Q transmittance.

be investigated with this lamp, other $LaVO_3$ bandgaps could be found in this range (1.80 and 2.99 eV) with respect to the one at lower energies which could be identified using the QTH lamp (1.1 eV); cf. Sec. 3.1 [2].
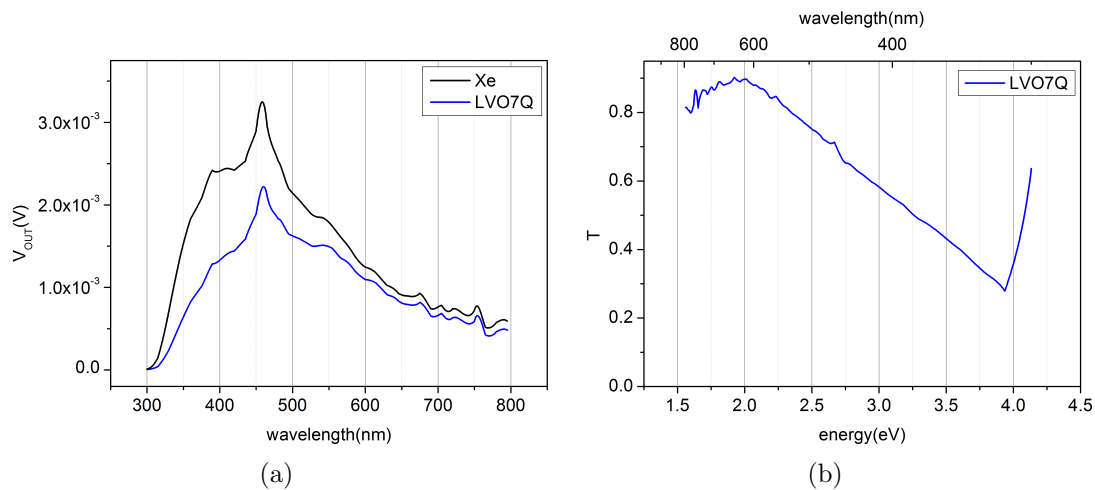
Figure 4.11: (a) LVO7Q transmission spectrum (blue) compared to the Xe flux (black). V_{OUT} is the output voltage signal measured by the pyroelectric sensor. (b) LVO7Q transmittance.

Fig. 4.11 (a) depicts the LVO7Q transmission spectrum compared to the Xe flux and Fig. 4.11 (b) the corresponding transmittance.

In order to understand the characteristics of the performed measurements, the absorption coefficient α was calculated using Eq. 4.1 from the optical transmission data.

<div align="center">(a)   (b)</div>
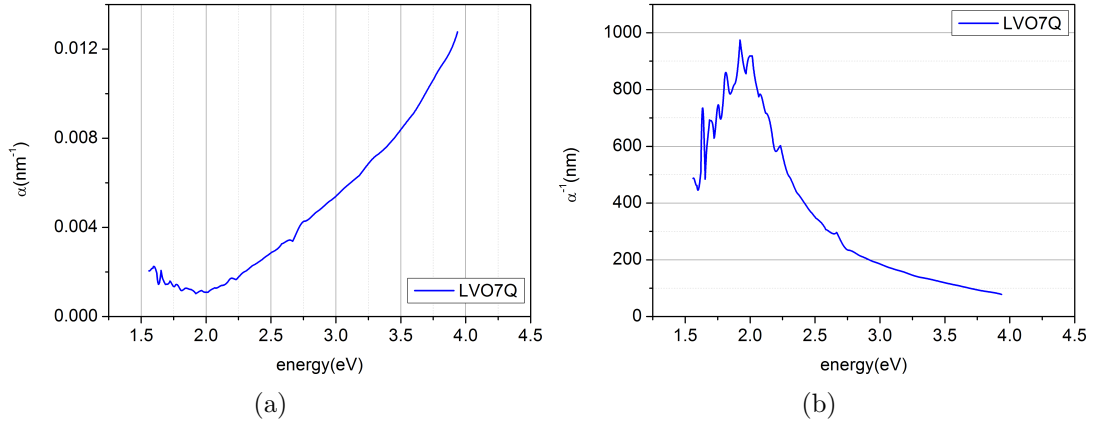
Figure 4.12: Plots of (a) α and (b) α^{-1} as functions of the energy of the impinging photons.

Fig. 4.12 (a) and (b), respectively, present the plots of α and α^{-1} (an estimate of the photon penetration depth) as functions of the energy of the impinging photons.
Since optical properties of $LaVO_3$ are still debated in literature (the optical gaps are cited as direct and/or indirect in the literature [2, 49] and $LaVO_3$ can contain also amorphous phases), a clear model to extract the bandgap value from absorption data is not available. Therefore, the bandgap value has been estimated by the energy onset of the absorption edge of α plot (Fig. 4.12 (a)), and its value is around 1.8 eV, which corresponds to one of the $LaVO_3$ bandgaps [2].
The α^{-1} plot shows that, in the spectral range of interest, photons penetrate in the sample at a depth ranging from 400 to 900 nm, while the investigated $LaVO_3$ samples are thinner, with the thickest sample among all (LVO14Q) only 130 nm thick.

Therefore, since SPV signal comes from electron-hole generation and collection by the surface band-bending, in order to have measurable SPV signal, photoinduced electron-hole pairs need to be generated as much as possible within the sample. Thus the ideal

condition is when α^{-1} is less than or almost equal to d (that is the sample thickness). As this condition is not satisfied, SPV measurements will be concentrated on thicker samples (LVO7Q and LVO14Q).

4.3 SPV measurements

4.3.1 System functionality and working frequency tests

As done in the transmittance measurements, the system was tested with a known sample of GaN. Moreover, a test on frequency was conducted to determine which was the most appropriate one to detect the SPV signal.

The SPV signal of GaN was acquired for different chopper frequencies, as illustrated in Fig. 4.13. First of all, a peak can be clearly observed in the plot, in correspondence of GaN bandgap, which means that the system is working properly. As far as it concerns frequency, the signal increases for lower frequencies, but 77 Hz was chosen as the best value for subsequent measurements, since the acquisition proceeds permanently stable (while for other frequencies several points were acquired in mean mode, cf. Sec. 3.2.2).
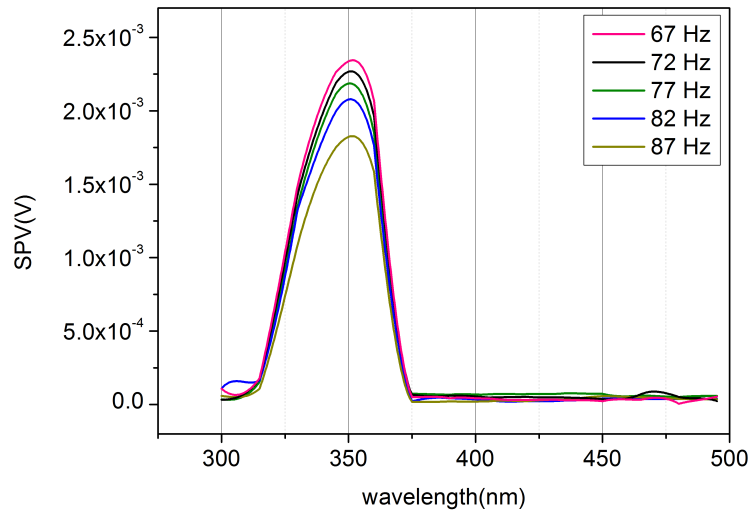
Figure 4.13: Acquisitions of the same SPV signal measured on GaN test sample for different chopper frequencies.
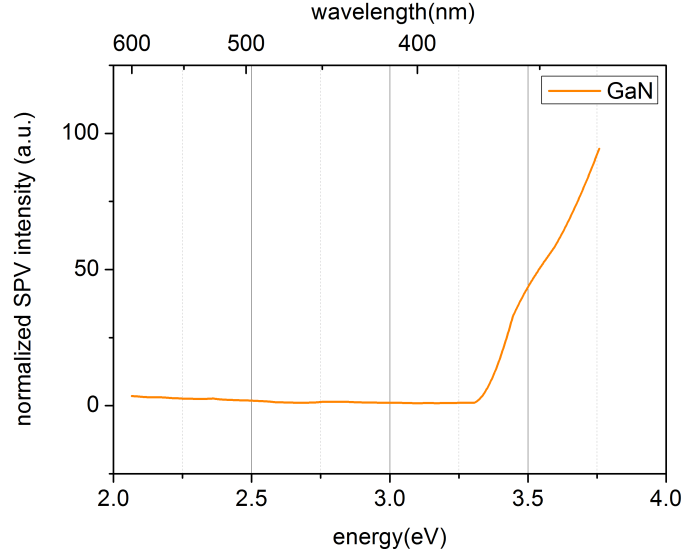
Figure 4.14: SPV normalized signal of GaN sample (at 77 Hz).

In Fig. 4.14, the plot of normalized SPV signal is shown: the edge corresponding to GaN bandgap (3.4 eV at 300 K) is evident, as already observed from the acquired signal as well. The normalization of the SPV signal is slightly different from the one performed for the transmission spectra measurements. In fact, the lamp flux and the SPV signal are collected by two different devices, while for the transmission spectra both signals are collected by the pyroelectric sensor; therefore, it is not sufficient to simply divide the measured SPV signal by the lamp flux for normalization.

The SPV normalized signal is obtained by the following equation:

$$SPV_{norm} = \frac{SPV_{meas}}{\dfrac{\Phi}{h\nu}} \tag{4.3}$$

where Φ is the lamp flux, SPV_{norm} and SPV_{meas} are SPV normalized and acquired signal respectively, and $h\nu$ is the energy of impinging photons.

4.3.2 LaVO₃ SPV measurements

SPV measurements on LaVO₃ samples were finally performed. As explained in Sec. 4.2.2, the investigation is focused on the thickest samples. SPV spectrum of sample LVO7Q on LaVO₃ side produced a signal below the detection limit of the apparatus ($<$ 1 µV). Thus the sample was investigated with the geometry shown in Fig. 4.15.
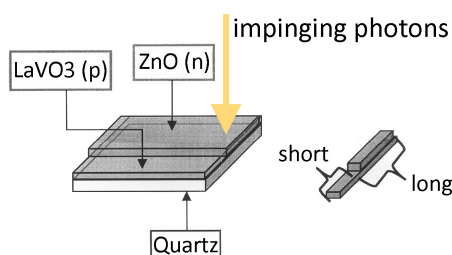
Figure 4.15: SPV measurements geometry.

At the $ZnO/LaVO_3$ interface a junction is created, thus the charge separation and collection is more efficient than at the free LaVO₃ surface, where only the surface band-bending is present. Also, ZnO is transparent in the spectral range of interest for LaVO₃ (the ZnO bandgap value is around 3.7 eV [73], while LaVO₃ detectable bandgap values in the considered spectral ranges are 1.1, 1.80 and 2.99 eV [2]). The SPV signal can be then acquired through the $ZnO/LaVO_3$ interface, where it is higher and more stable. Nevertheless, the signal is quite small and extremely noisy, as shown in Fig. 4.16.
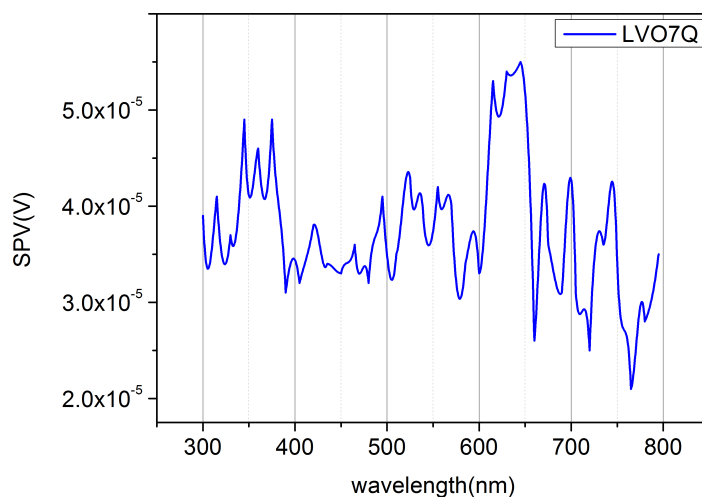
Figure 4.16: LVO7Q SPV signal (ZnO side).

Therefore, a further optimization of the optical system is required in order to get a better signal. A new lens was bought and mounted on the monochromator. This lens has a better performance because it is made of quartz, while the old one was made of glass; the advantages are the absence of absorption and a better optical coupling between the monochromator output and the sample; therefore, the output beam is considerably greater than the previous one. A comparison of QTH and Xe fluxes with and without the new lens is shown in Fig. 4.17.
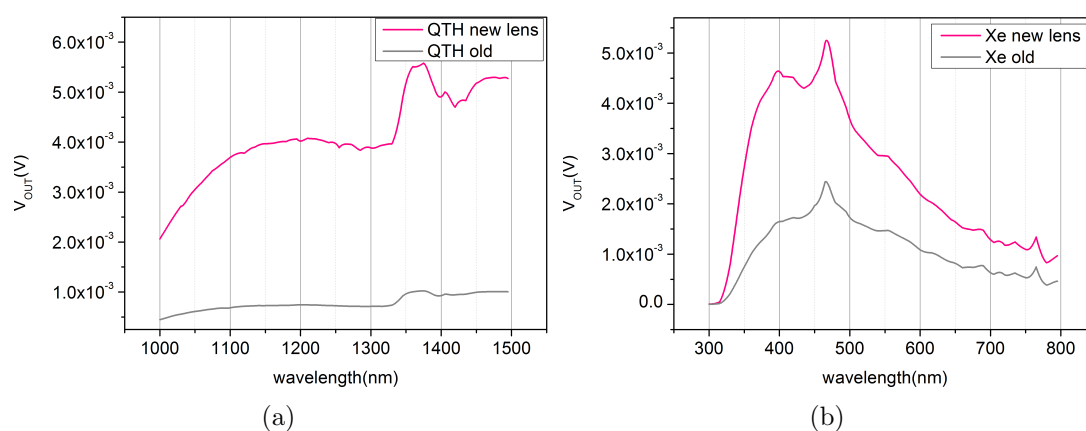
Figure 4.17: (a) QTH and (b) Xe fluxes acquired with the new lens in the optical system (pink) compared to old fluxes without the lens (grey). V_{OUT} is the output voltage signal measured by the pyroelectric sensor.

SPV measurements on LVO14Q, acquired on ZnO side as well, show a higher and much more stable signal with the new lens. ZnO bandgap (3.7 eV [73]) is clearly visible: as a peak in the SPV measured signal (Fig. 4.18 (a)), and as an edge in the SPV normalized intensity (Fig. 4.18 (b)), obtained using Eq. 4.3. However, no signal beside the ZnO one has been detected.

A last attempt was done using the QTH lamp, trying to investigate a different spectral range, in order to verify the presence of a significant signal in this range. Fig. 4.19 (a) depicts the SPV signal compared to the QTH flux and it is evident that SPV on LaVO₃ provided an almost zero signal even in this spectral range. The same SPV signal is reported in Fig. 4.19 (b) too.

(a)   (b)
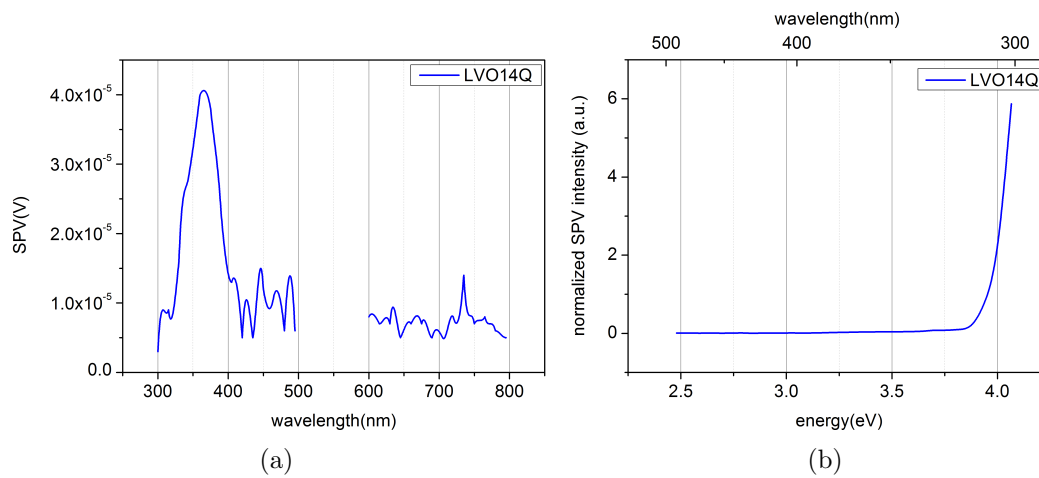
Figure 4.18: LVO14Q SPV measured (a) and normalized (b) signal.

(a)   (b)
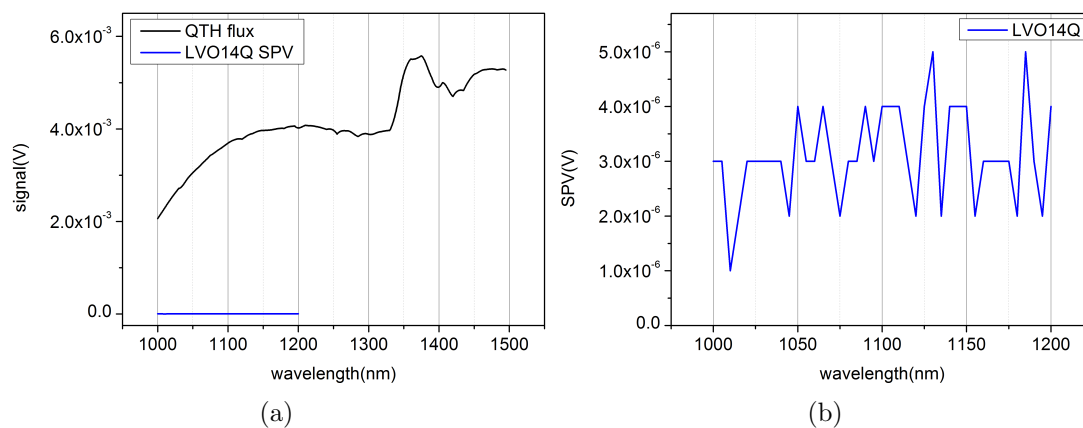
Figure 4.19: (a) LVO14Q SPV signal (blue) compared to the QTH flux. (b) LVO14Q SPV signal on enlarged vertical scale.

4.4 AFM measurements

4.4.1 Morphological analysis

Non-contact AFM maps were acquired to investigate morphological properties of the samples at the nanoscale. For every sample, maps of different size were acquired.

The samples (whose full list has been presented in Tab. 4.1) differ for substrate, deposition technique and thickness. The first sample investigated was LVO22Q, whose features were used as a reference for comparison with the following measurements. In fact, the other samples differ from LVO22Q by only one parameter (i.e. substrate, deposition technique or thickness). In this way it was possible to easily identify how the single parameter influences the surface morphology.

(a)   (b)
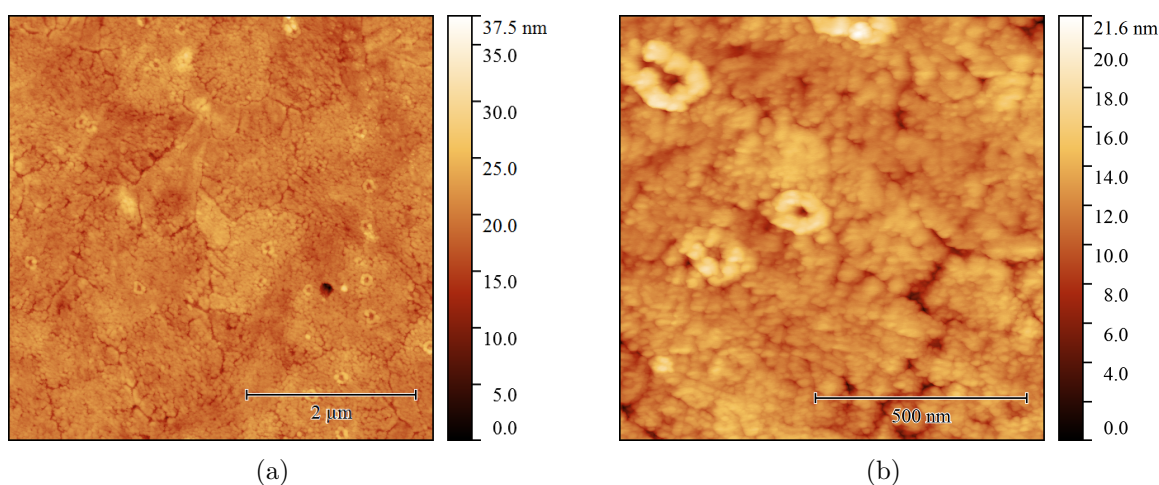
Figure 4.20: Surface morphology of LVO22Q: 55 nm LaVO$_3$ on quartz (sputtering). The scan area is 5x5 μm^2 for map (a) and 1x1 μm^2 for map (b).

LVO22Q maps (Fig. 4.20) present different zones separated by grain boundaries. This separation is probably due to the quartz substrate structure which has a very pleated surface. Ring-like structures are present, of 100-200 nm diameter.

Different substrate: quartz *versus* Si

LVO24S maps (Fig. 4.21) present a roughness decrease of one order of magnitude with respect to the LVO22Q sample, and no grain boundaries. This is due to the different substrate; in fact, Si has a very flat surface which reflects on the layers surface on the top of it. Ring-like structures with a hole of 5-10 nm of depth are still present. Since the deposition technique is the same as LVO22Q, these ring-like defects are probably due to molecular impact during sputtering. It is likely that ring-like structures may be avoided by lowering power deposition.

80
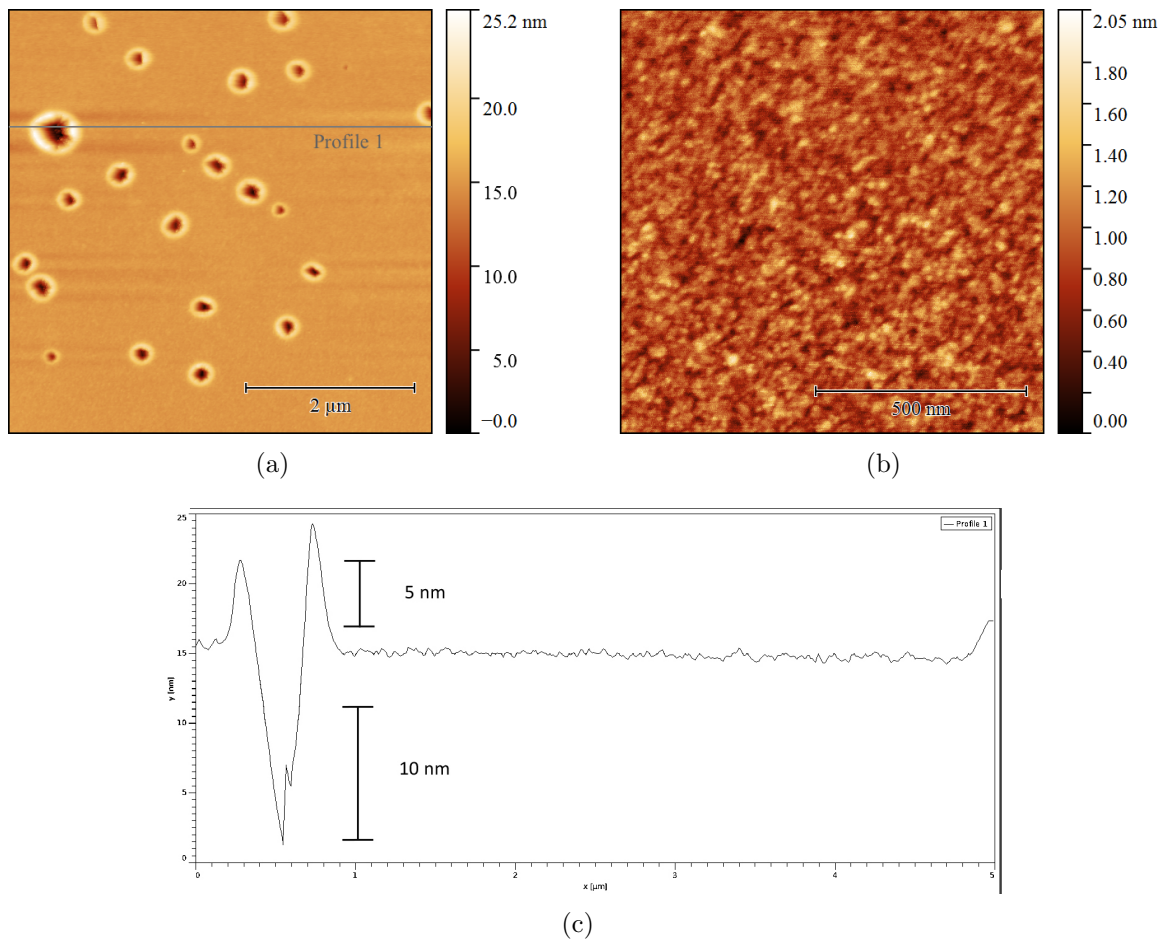
Figure 4.21: (a) Surface morphology of LVO24S: 55 nm LaVO$_3$ on Si (sputtering). The scan area is 5x5 μm^2 for map (a) and 1x1 μm^2 for map (b). Map (b) is almost flat; it is a small part of surface with no ring-like structures. (c) Profile height of the line indicated in map (a), with an esteem of hole dimensions.

Different deposition technique: sputtering *versus* solgel

LVOsg2Q maps (Fig. 4.22) also present a roughness decrease with respect to the LVO22Q sample, but grain boundaries are still present. This double check proves the correlation between the presence of these grain boundaries and the quartz substrate. Ring-like structures disappear, confirming that their existence is due to the sputtering technique.
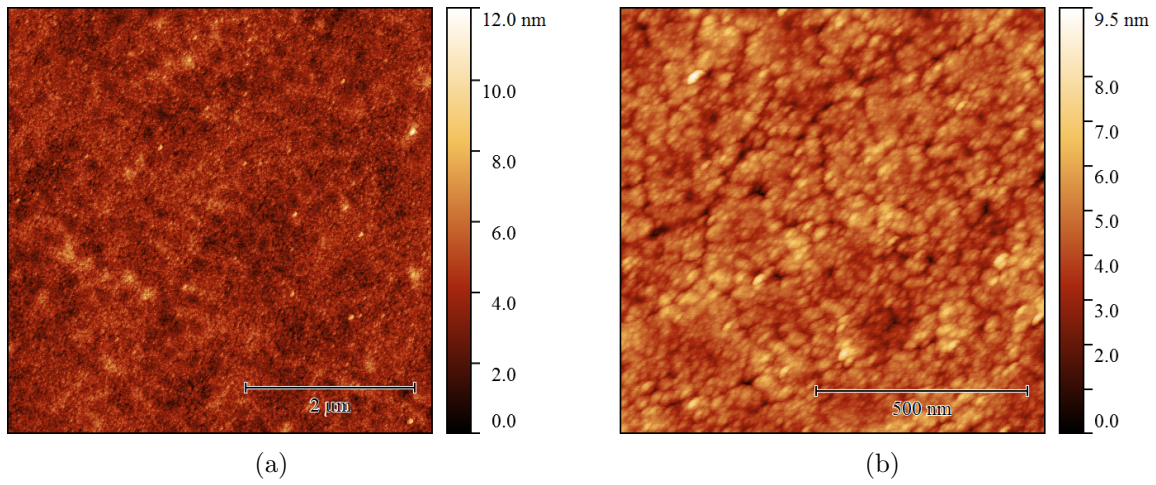
Figure 4.22: Surface morphology of LVOsg2Q: 36 nm LaVO$_3$ on quartz (solgel). The scan area is 5x5 μm^2 for map (a) and 1x1 μm^2 for map (b).

Different thickness: thin (around 50 nm) *versus* thick (around 100 nm)

Since the LVO7Q and LVO14Q samples have very similar features as far as structure, substrate and deposition techniques are concerned, the surface morphology of the two samples is almost equal. Only LVO14Q is presented in the compared analysis because its maps show the most stable signals and better reproducibility.
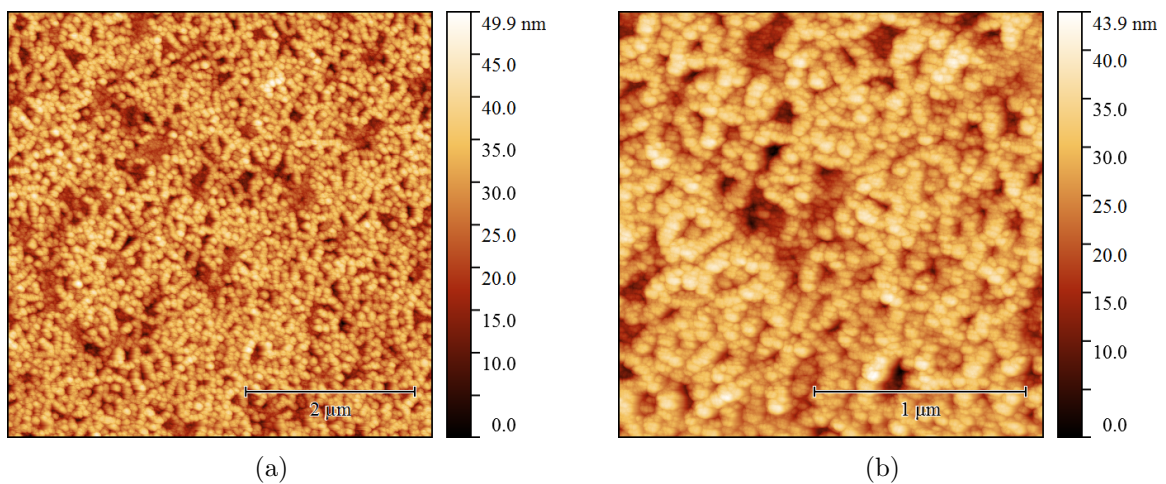
Figure 4.23: Surface morphology of LVO14Q: ZnO (100 nm) // LaVO$_3$ (130 nm) // quartz (sputtering). The scan area is 5x5 μm^2 for map (a) and 2x2 μm^2 for map (b).

LVO14Q maps (Fig. 4.23) present a roughness increases with respect to the LVO22Q sample; grain boundaries disappear with higher thicknesses. Ring-like structures are still present, but with a smaller depth and diffusion.

This structure is exactly the same both on the $LaVO_3$ and on the ZnO side.

The larger deposition time (necessary to achieve a greater thickness) may allow the atoms to migrate and rearrange on the surface.

The extrapolated RMS roughness σ_{RMS} (measured in zones without ring-like structures) of investigated samples are reported in Tab. 4.3.

	substrate	deposition technique	thickness (nm)	σ_{RMS} (nm)
LVO22Q	quartz	sputtering	55	2.7 ± 0.5
LVO24S	Si	sputtering	55	0.20 ± 0.02
LVOsg2Q	quartz	solgel	36	0.9 ± 0.1
LVO14Q	quartz	sputtering	130	5 ± 1

Table 4.3: RMS roughness values of investigated samples, measured in zones without ring-like structures.

The conclusions of the AFM morphological analysis can be summarized as follows.

- The presence of ring-like features is probably due to sputtering deposition, since they occur in samples deposited by sputtering on different substrates and disappear in the sample deposited by solgel.

- Ring-like features change in dimensions and number with increasing thickness of the layer, as the atom migration is more pronounced with higher deposition times.

- Thin layers grown on quartz show the presence of grain boundaries due to the high roughness of the substrate surface. This feature disappears with increasing thickness of the layer.

4.4.2 Electrical characterization

Electrical force microscopy (EFM) and scanning Kelvin probe microscopy (SKPM) maps were acquired to investigate the surface electrical property of the sample LVO14Q at the nanoscale.

As described in Sec. 3.2.3, EFM and SKPM techniques differ in the way the mapped signal is detected. In EFM, the bare tip-sample electrostatic potential is mapped, which could be dependent also on morphological effect. In the SKPM, a feedback signal is used in order to cancel out the measured surface potential, and the bias applied to the feedback loop is then mapped. The SKPM allows for the determination of the contact potential difference V_{CPD} defined as in Eq. 2.2 here reported:

$$eV_{\mathrm{CPD}} = W_{\mathrm{tip}} - W_{\mathrm{sample}} = \Delta W.$$

Fig. 4.24 depicts a 30x30 μm^2 map showing the edge between LaVO$_3$ and ZnO. The topography map in Fig. 4.24 (a) shows a depression at the edge between the two layers, likely due to the feedback based acquisition of constant force mode, while a step should be expected since the ZnO layer deposited on LaVO$_3$ is 100 nm thick (Fig. 4.1). In addition, the morphology has the exact same structure on both sides, as already seen from the topography maps analysed in the previous section. On the contrary, from EFM and SKPM images, the difference between the two materials is clearly visible.

The average values of the measured potentials are reported in Tab. 4.4.

	LaVO$_3$	ZnO
EFM (electrostatic potential) (V)	$(0.10 \pm 0.05) \cdot 10^{-3}$	$(1.88 \pm 0.04) \cdot 10^{-3}$
SKPM (V_{CPD}) (V)	0.175 ± 0.005	0.300 ± 0.005
W calculated value (eV)	4.625 ± 0.005	4.500 ± 0.005

Table 4.4: EFM and SKPM extrapolated potential average values and calculated work functions for LaVO$_3$ and ZnO.

A reliable value unaffected by morphology effect can be extracted by the SKPM average value. The measured value of the V_{CPD} allows for the extraction of the value of the work function W for both the materials. As the tip is made by gold, whose work function is $W_{\mathrm{Au}} = 4.8$ eV [74], the work function values have been evaluated and reported in Tab.
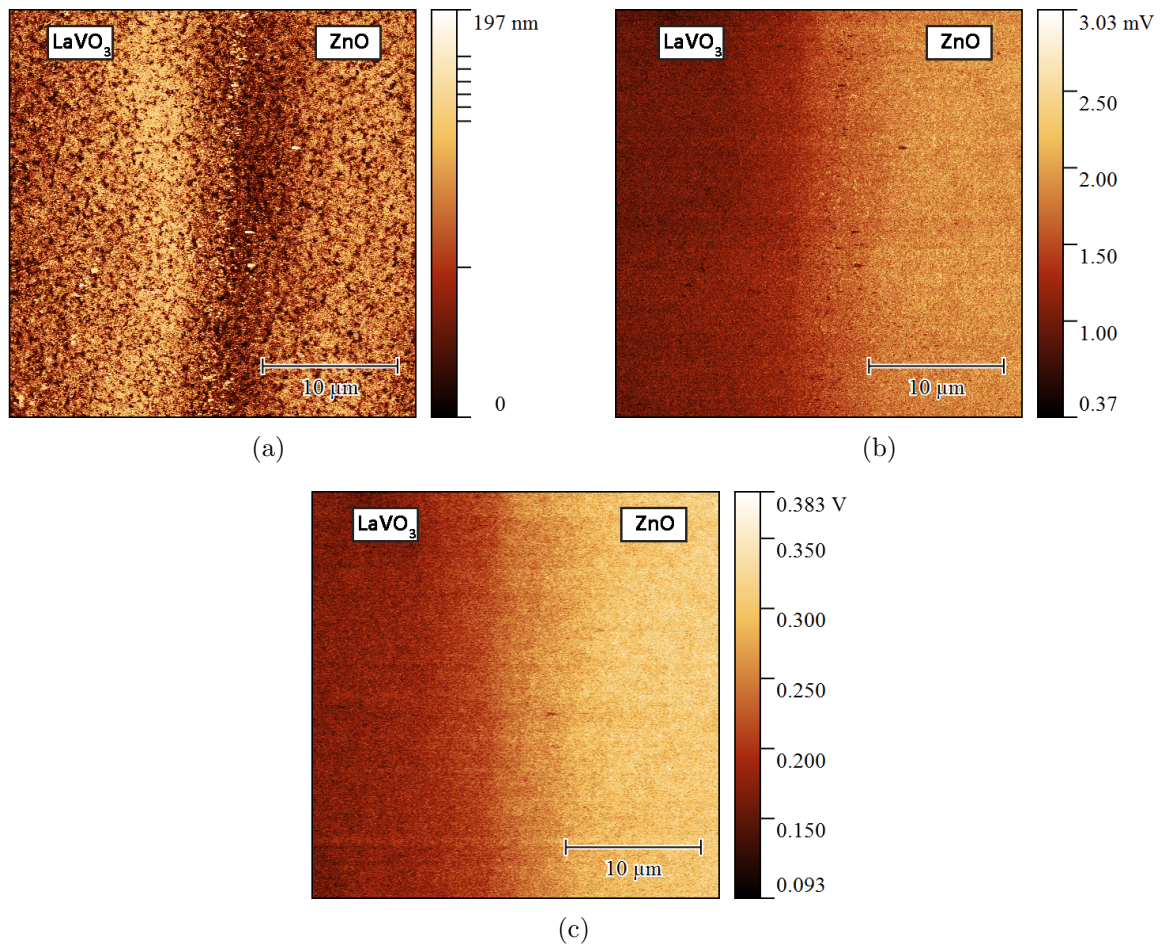
Figure 4.24: LVO14Q at the edge between $LaVO_3$ and ZnO (scan area 30x30 μm^2): (a) topography, (b) EFM, (c) SKPM. $LaVO_3$ is on the left side and ZnO on the right side of the map.

4.4 last row. As the result obtained for ZnO well compares with literature values (which span from 3.7 to 6.0 eV depending on the surface orientation and deposition methods [75]), the result for $LaVO_3$ can be considered reliable as well. In addition, it is worth mentioning that the barrier height value between ZnO and $LaVO_3$ is equal to 0.125 V.

Then, a more enlarged map (2x2 μm^2) was acquired only on $LaVO_3$ (Fig. 4.25), to investigate the surface potential variations at the nanoscale.
It can be noticed that the EFM signal is highly correlated to morphology, as expected. The SKPM map shows tiny variations, that seem to be due only to noise effects: the
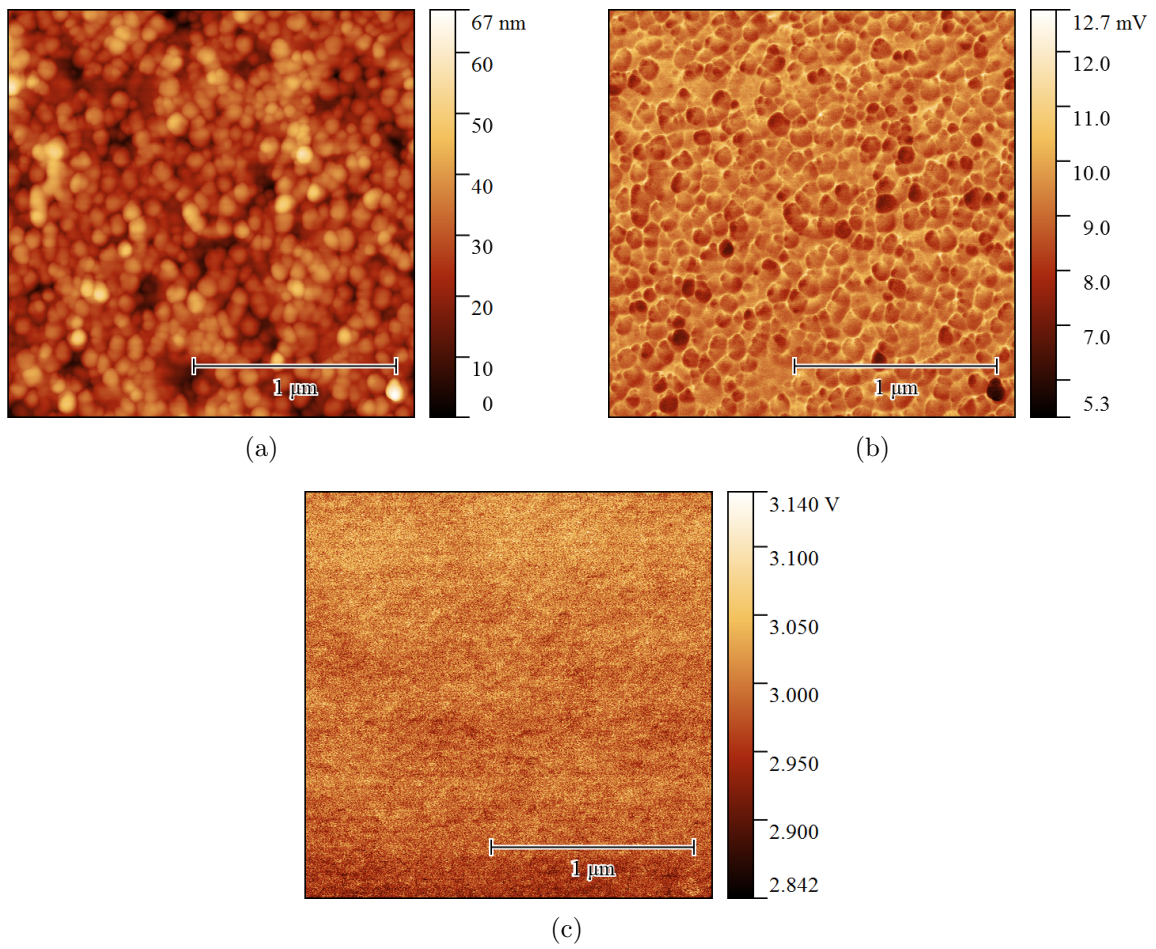
Figure 4.25: LVO14Q on LaVO$_3$ side (scan area 2x2 µm^2): (a) topography, (b) EFM, (c) SKPM.

grains detected in the topography maps do not show appreciable variations in the surface potential, within the sensitivity of the method.

Conclusions

The research on innovative materials for photovoltaic application has recently focused on perovskites for the development of new types of high efficiency and low cost solar cells. Perovskite based solar cells faced indeed an unbelievable increase in the last years, reaching a certified efficiency of 22.1% in early 2016 [1], an impressive value considering that seven years ago these devices did not exist at all. However, perovskite photovoltaics are still far from commercialization because of their high instability. $LaVO_3$ is a transition metal oxide perovskite promising for photovoltaic applications, which could overcome the stability issue.

Within this framework, $LaVO_3$ optical and electrical properties have been investigated in this thesis. The main objectives of the present thesis were the following.

1. The implementation and optimization of a surface photovoltage (SPV) spectroscopy experimental set-up, and the development of the related data acquisition software.

2. The investigation of optoelectronic properties of $LaVO_3$ by surface potential measurements (surface photovoltage spectroscopy, atomic force microscopy, electrical force and scanning Kelvin probe microscopies).

1. The first objective has been fully achieved: the surface photovoltage spectroscopy set-up has been implemented, and a software for data acquisition and system control has been developed. Moreover, the experimental set-up has been optimized in order to enhance the measured signal, as shown by the positive results obtained on the test samples (Si and GaN, measured for different spectral ranges).

2. The second objective (i.e. $LaVO_3$ characterisation) needs a detailed discussion.

2a) Morphological analysis to investigate surface properties at the nanoscale have been performed on the $LaVO_3$ thin layers, comparing different deposition parameters (different substrate, different deposition technique and different thickness). Sputtering deposition technique dramatically increases the surface roughness, while optimal surface properties with low roughness have been obtained for solgel deposition. As a matter of fact, high surface roughness could result in high surface recombination rate, which makes surfaces act as lifetime killers with detrimental effects on the solar device performance.

2b) Electrical characterisation for the measurement of the surface potential, performed by scanning Kelvin probe microscopy, showed that the grains do not present appreciable variations in the surface potential, within the sensitivity of the method. Moreover, the barrier height value at the $LaVO_3$/ZnO interface, equal to 0.125 V has been obtained, and this value is in good agreement with the one extracted by measured current-voltage characteristics shown in Fig. 4.26 [76]. It can be noted that the built-in potential is around 0.1 V, in very good agreement with the barrier height evaluated by SKPM. In addition, besides to the measurement of the $LaVO_3$/ZnO barrier height, SKPM has also allowed to determine the surface potential, and thus work functions of ZnO and $LaVO_3$. It is noteworthy that the measured value of the work function of $LaVO_3$ has never been reported in literature up to now.

2c) Surface photovoltage spectroscopy on $LaVO_3$ gave a signal below the detection limit of the apparatus. In fact, the evaluated low barrier height value indicates that photogenerated electron-hole pairs are inefficiently separated and thus collected. This can explain the behaviour shown in Fig. 4.26, where dark and light current-voltage characteristics almost overlap. SPV signal could not be measured if the free carriers are not efficiently separated and collected.

In conclusion, $LaVO_3$ is known to have optimal optical properties and high stability, which are considerable benefits for possible photovoltaic devices. However, SPV measurements, which are sensitive to transport properties besides the optical ones, have clearly shown that this material is a poor charge-transport medium. Therefore, $LaVO_3$ investigated samples are not suitable for photovoltaic applications. To overcome the
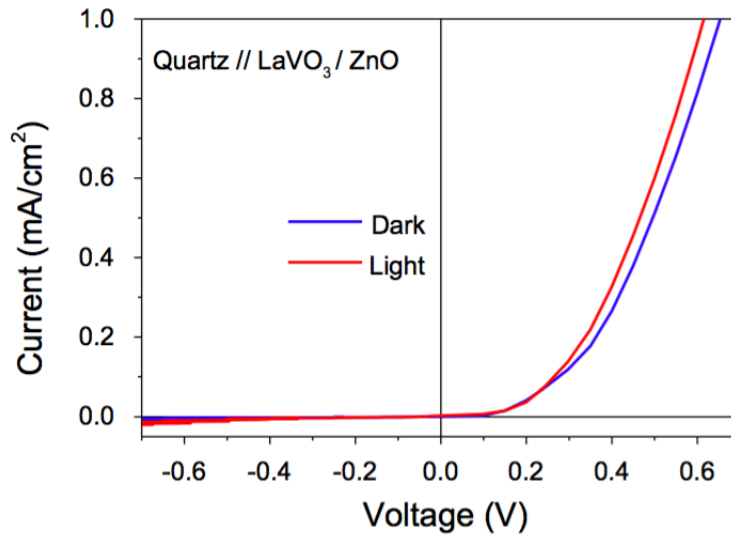
Figure 4.26: Current-voltage characteristics for LaVO$_3$/ZnO grown on quartz [76].

limitation of the poor carrier transport properties of LaVO$_3$, a solution could be the incorporation of an additional electron-transport material and hole-transport material into a structure similar to the design of dye-sensitized solar cells, as proposed by Wang et al. in 2015 [2]. In such a structure, a huge number of internal interfaces between the individual solar absorber and nanostructured charge transport media would enable the separation and collection of photogenerated electron-hole pairs. These considerations could pave the way for future developments on the study and optimization of LaVO$_3$ perovskite as a material for photovoltaic applications.

Acknowledgments

First of all, I would like to thank Prof. Daniela Cavalcoli for her endless patience. She has constantly supported me with her competent guidance, giving me valuable tips on the experiments, and helpful observations when discussing the results together. Also, she has always been available to answer all my questions, and always with great kindness.

Many thanks to Thomas Fix and Abdel Slaoui from the research group at MaCEPV (Materials for electronic and photovoltaic devices), iCube, CNRS, Université de Strasbourg, for samples deposition.

I am very thankful to the PhD student Maria Antonietta Fazio, because, even if I was the first student she had to supervise for a thesis, she helped and supported me in the best way.
I gratefully acknowledge Filippo Maria Giorgi for its essential teaching concerning electronics and software development, and thanks for saving me every time that the computer seemed to be dead and I had no hope.

Finally, thanks to the people that helped me behind the scenes. I really thank my parents Luana and Pier Giacomo for their great help in these years, I know it was not easy and I really appreciate. A huge thanks to all my family: my wonderful grandparents Adriana, Narciso e Giuseppina, my aunts Maria Giulia and Mirna and my uncle Giovanni, who have always sincerely believed in me. I would like to thank my favourite cousin and friend Marta, and Davide.

I would like to thank Andrea the genius for his precious help and support during these years.
I will never thank enough my best friend Rina for everything she did for me, for supporting me all the time and for understanding me without a word, because we are too

much TOO MUCH. My sincere thanks goes to Eugenia, Ludovica, Beatrice, Valeria and Anna: all these ladies are an essential and irreplaceable part of my life.

Thanks also to Chiara, who always understands me and gives me good advices, and Cora for the beautiful time spent together.

At last, I would like to thank my wonderful boyfriend Stefano, who has always supported me even in the worst moments, and who constantly makes me happy and proud.

Bibliography

[1] http://www.nrel.gov/ncpv/.

[2] L. Wang, Y. Li, A. Bera, C. Ma, F. Jin, K. Yuan, W. Yin, A. David, W. Chen, W. Wu, *et al.*, "Device Performance of the Mott Insulator LaVO$_3$ as a Photovoltaic Material," *Physical Review Applied*, vol. 3, no. 6, p. 064015, 2015.

[3] https://thelostelectron.wordpress.com/2015/05/28/beginners-guide-to-hybrid-organic-inorganic-halide-perovskite-mapi-solar-cells/.

[4] "BP Statistical review of world energy 2015." http://www.bp.com.

[5] "UNEP Yearbook—Emerging Issues in Our Global Environment," 2012.

[6] N. Armaroli and V. Balzani, "Solar Electricity and Solar Fuels: Status and Perspectives in the Context of the Energy Transition," *Chemistry–A European Journal*, vol. 22, no. 1, pp. 32–57, 2016.

[7] R. G. Miller and S. R. Sorrell, "The future of oil supply," *Philosophical Transactions of the Royal Society of London A: Mathematical, Physical and Engineering Sciences*, vol. 372, no. 2006, p. 20130179, 2014.

[8] L. Maugeri, "The shale oil boom: a US phenomenon," *Harvard Kennedy School*, 2013.

[9] V. Balzani and N. Armaroli, *Energy for a sustainable world: from the oil age to a sun-powered future.* John Wiley & Sons, 2010.

[10] "Renewable Energy Policy Network for the 21 st Century." http://www.ren21.net/.

[11] J. Mathews, *Greening of Capitalism: How Asia Is Driving the Next Great Transformation.* Stanford University Press, 2014.

[12] http://www.ise.fraunhofer.de/.

[13] J. Nelson, *The Physics of Solar Cells.* Imperial College Press, 2013.

[14] http://www.liverpool.ac.uk/renewable-energy/.

[15] http://www.newport.com/Introduction-to-Solar-Radiation/.

[16] M. Green, *Third generation photovoltaics: advanced solar energy conversion*, vol. 12. Springer Science & Business Media, 2006.

[17] S. Chen, X. Gong, and S.-H. Wei, "Band-structure anomalies of the chalcopyrite semiconductors $CuGaX_2$ versus $AgGaX_2$ (X= S and Se) and their alloys," *Physical Review B*, vol. 75, no. 20, p. 205209, 2007.

[18] F. Dimroth and S. Kurtz, "High-efficiency multijunction solar cells," *MRS bulletin*, vol. 32, no. 03, pp. 230–235, 2007.

[19] Ncouniot - Fraunhofer Institute for Solar Energy Systems.
https://commons.wikimedia.org/w/index.php?curid=8980251.

[20] B. Burnett, "The basic physics and design of III-V multijunction solar cells," *National Renewable Energy Laboratory*, 2002.

[21] N. V. Yastrebova *et al.*, "High-efficiency multi-junction solar cells: Current status and future potential," *Solar Energy*, 2007.

[22] http://webmineral.com/data/Perovskite.shtml/.

[23] http://globalsolartechnology.com/.

[24] A. Kojima, K. Teshima, Y. Shirai, and T. Miyasaka, "Organometal halide perovskites as visible-light sensitizers for photovoltaic cells," *Journal of the American Chemical Society*, vol. 131, no. 17, pp. 6050–6051, 2009.

[25] J.-H. Im, C.-R. Lee, J.-W. Lee, S.-W. Park, and N.-G. Park, "6.5% efficient perovskite quantum-dot-sensitized solar cell," *Nanoscale*, vol. 3, no. 10, pp. 4088–4093, 2011.

[26] M. M. Lee, J. Teuscher, T. Miyasaka, T. N. Murakami, and H. J. Snaith, "Efficient hybrid solar cells based on meso-superstructured organometal halide perovskites," *Science*, vol. 338, no. 6107, pp. 643–647, 2012.

[27] H.-S. Kim, C.-R. Lee, J.-H. Im, K.-B. Lee, T. Moehl, A. Marchioro, S.-J. Moon, R. Humphry-Baker, J.-H. Yum, J. E. Moser, *et al.*, "Lead iodide perovskite sensitized all-solid-state submicron thin film mesoscopic solar cell with efficiency exceeding 9%," *Scientific reports*, vol. 2, 2012.

[28] M. A. Green, A. Ho-Baillie, and H. J. Snaith, "The emergence of perovskite solar cells," *Nature Photonics*, vol. 8, no. 7, pp. 506–514, 2014.

[29] L. Kronik and Y. Shapira, "Surface photovoltage phenomena: theory, experiment, and applications," *Surface Science Reports*, vol. 37, no. 1, pp. 1–206, 1999.

[30] L. Kronik and Y. Shapira, "Surface photovoltage spectroscopy of semiconductor structures: at the crossroads of physics, chemistry and electrical engineering," *Surface and Interface analysis*, vol. 31, no. 10, pp. 954–965, 2001.

[31] W. H. Brattain and J. Bardeen, "Surface properties of germanium," *Bell System Technical Journal*, vol. 32, no. 1, pp. 1–41, 1953.

[32] E. Johnson, "Measurement of minority carrier lifetimes with the surface photovoltage," *Journal of Applied Physics*, vol. 28, no. 11, pp. 1349–1353, 1957.

[33] A. M. Goodman, "A method for the measurement of short minority carrier diffusion lengths in semiconductors," *Journal of Applied Physics*, vol. 32, no. 12, pp. 2550–2552, 1961.

[34] H. C. Gatos and J. Lagowski, "Surface photovoltage spectroscopy — A new approach to the study of high-gap semiconductor surfaces," *Journal of Vacuum Science & Technology*, vol. 10, no. 1, pp. 130–135, 1973.

[35] I. F. Patai and M. A. Pomerantz, "Contact potential differences," *Journal of the Franklin Institute*, vol. 252, no. 3, pp. 239–260, 1951.

[36] Lord Kelvin, "Contact electricity of metals," *The London, Edinburgh, and Dublin Philosophical Magazine and Journal of Science*, vol. 46, no. 278, pp. 82–120, 1898.

[37] K. Besocke and S. Berger, "Piezoelectric driven Kelvin probe for contact potential difference studies," *Review of Scientific Instruments*, vol. 47, no. 7, pp. 840–842, 1976.

[38] S. Morrison, "Changes of surface conductivity of germanium with ambient," *The Journal of Physical Chemistry*, vol. 57, no. 8, pp. 860–863, 1953.

[39] W. Nabhan, B. Equer, A. Broniatowski, and G. De Rosny, "A high-resolution scanning Kelvin probe microscope for contact potential measurements on the 100 nm scale," *Review of scientific instruments*, vol. 68, no. 8, pp. 3108–3111, 1997.

[40] Y. Kuk, R. Becker, P. Silverman, and G. Kochanski, "Optical interactions in the junction of a scanning tunneling microscope," *Physical review letters*, vol. 65, no. 4, p. 456, 1990.

[41] J. Weaver and H. Wickramasinghe, "Semiconductor characterization by scanning force microscope surface photovoltage microscopy," *Journal of Vacuum Science & Technology B*, vol. 9, no. 3, pp. 1562–1565, 1991.

[42] L. Burstein, J. Bregman, and Y. Shapira, "Characterization of interface states at III-V compound semiconductor-metal interfaces," *Journal of applied physics*, vol. 69, no. 4, pp. 2312–2316, 1991.

[43] W. Krystek, F. H. Pollak, Z. Feng, M. Schurman, and R. Stall, "Nondestructive, Room Temperature Determination Of The Nature Of The Band-Bending (Carrier Type) In Group III Nitrides Using Contactless Electroreflectance And Surface Photovoltage Spectroscopy," in *MRS Proceedings*, vol. 482, p. 573, Cambridge Univ Press, 1997.

[44] L. Kronik, B. Mishori, E. Fefer, Y. Shapira, and W. Riedl, "Quality control and characterization of Cu(In,Ga)Se$_2$ based thin-film solar cells by surface photovoltage spectroscopy," *Solar energy materials and solar cells*, vol. 51, no. 1, pp. 21–34, 1998.

[45] R. M. Jacobs, D. Morgan, and J. H. Booske, "Perovskite oxides: New candidate materials for low work function electron emitters," in *Vacuum Electronics Conference, IEEE International*, pp. 133–134, IEEE, 2014.

[46] H. Rotella, O. Copie, G. Steciuk, H. Ouerdane, P. Boullay, P. Roussel, M. Morales, A. David, A. Pautrat, B. Mercey, *et al.*, "Structural analysis of strained $LaVO_3$ thin films," *Journal of Physics: Condensed Matter*, vol. 27, no. 17, p. 175001, 2015.

[47] Y. Yuan, Z. Xiao, B. Yang, and J. Huang, "Arising applications of ferroelectric materials in photovoltaic devices," *Journal of Materials chemistry A*, vol. 2, no. 17, pp. 6027–6041, 2014.

[48] D. Rogers, A. Ferretti, D. Ridgley, R. Arnott, and J. Goodenough, "Single-Crystal Growth and Properties of the Perovskites $LaVO_3$ and YVO_3," *Journal of Applied Physics*, vol. 37, no. 3, pp. 1431–1432, 1966.

[49] O. Madelung, U. Rössler, and M. Schulz, *Landolt-Börnstein, Group III Condensed Matter (Ternary Compounds, Organic Semiconductors)*, vol. 41E. Springer Materials, 2000.

[50] http://www.forter.com.tw/.

[51] http://www.controlledenvironments.org/Light1994Conf/5_9_Kofferlein/ Kofferlein%20text.htm.

[52] http://www.horiba.com/fileadmin/uploads/Scientific/Documents/OSD/ MSeries.pdf.

[53] http://www.fisica.uniud.it/URDF/secif/mec_q/esp/plank_5.htm.

[54] http://www.newport.com/Grating-Physics/383720/1033/content.aspx.

[55] http://www.horiba.com/scientific/products/optics-tutorial/ diffraction-gratings/.

[56] http://www.forter.com.tw/.

[57] G. W. John, "The Measurement, Instrumentation and Sensors Handbook," 1999.

[58] http://www.thinksrs.com/products/SR810830.htm.

[59] http://www.thinksrs.com/downloads/PDFs/Manuals/SR830m.pdf.

[60] D. Stamps, *Learn LabVIEW 2013 / 2014 Fast: A Primer for Automatic Data Acquisition.* SDC Publications, 2015.

[61] R. A. Oliver, "Advances in AFM for the electrical characterization of semiconductors," *Reports on Progress in Physics*, vol. 71, no. 7, p. 076501, 2008.

[62] J. E. Jones, "On the determination of molecular fields. II. From the equation of state of a gas," in *Proceedings of the Royal Society of London A: Mathematical, Physical and Engineering Sciences*, vol. 106, pp. 463–477, The Royal Society, 1924.

[63] T. Y. Edward, "Nanoscale characterization of semiconductor materials and devices using scanning probe techniques," *Materials Science and Engineering: R: Reports*, vol. 17, no. 4, pp. 147–206, 1996.

[64] F. J. Giessibl, "Advances in atomic force microscopy," *Reviews of modern physics*, vol. 75, no. 3, p. 949, 2003.

[65] http://www.parkafm.com/index.php/park-afm-technology/true-non-contact-mode.

[66] R. J. Colton, "Nanoscale measurements and manipulation," *Journal of Vacuum Science & Technology B*, vol. 22, no. 4, pp. 1609–1635, 2004.

[67] http://www.parkafm.com/index.php/parl-spm-modes/dielectric-piezoelectric-properties/228-electric-force-microscopy-efm.

[68] http://www.parkafm.com/index.php/park-spm-modes/93-dielectric-piezoelectric/232-scanning-kelvin-probe-microscopy-skpm.

[69] http://www.nanosensors.com/SuperSharpSilicon-Non-Contact-Tapping-mode-High-Resonance-Frequency-Reflex-Coating-afm-tip-SSS-NCHR.

[70] http://www.nanosensors.com/PointProbe-Plus-Non-Contact-Soft-Tapping-Mode-Au-Coating-afm-tip-PPP-NCSTAu.

98

[71] `http://gwyddion.net/`.

[72] J. I. Pankove, *Optical processes in semiconductors*. Courier Corporation, 2012.

[73] M. Nafees, W. Liaqut, S. Ali, and M. A. Shafique, "Synthesis of ZnO/Al: ZnO nano-material: structural and band gap variation in ZnO nanomaterial by Al doping," *Applied Nanoscience*, vol. 3, no. 1, pp. 49–55, 2013.

[74] M. Grundmann, *The physics of semiconductors: an introduction including devices and nanophysics*. Springer Science & Business Media, 2006.

[75] H. Moormann, D. Kohl, and G. Heiland, "Work function and band bending on clean cleaved zinc oxide surfaces," *Surface Science*, vol. 80, pp. 261–264, 1979.

[76] Thomas Fix et al., MaCEPV laboratory, iCube, CNRS, Université de Strasbourg, private communication.